Elektromagnetischegolfanalyse van golfgeleiders met meerdere geleiders
en een Calderón-preconditioneerder
voor de heterogene Poincaré-Steklov-operator

Full-Wave Multiconductor Waveguide Analysis
and a Calderón Preconditioner
for the Heterogeneous Poincaré-Steklov Operator

Dieter Dobbelaere

Promotoren: prof. dr. ir. H. Rogier, prof. dr. ir. D. De Zutter
Proefschrift ingediend tot het behalen van de graad van
Doctor in de Ingenieurswetenschappen: Elektrotechniek

Vakgroep Informatietechnologie
Voorzitter: prof. dr. ir. D. De Zutter
Faculteit Ingenieurswetenschappen en Architectuur
Academiejaar 2015 - 2016

ISBN 978-90-8578-844-7
NUR 959
Wettelijk depot: D/2015/10.500/88

Full-Wave Multiconductor Waveguide Analysis and a Calderón Preconditioner for the Heterogeneous Poincaré-Steklov Operator

Dieter Dobbelaere

Dissertation submitted to obtain the academic degree of
Doctor of Electrical Engineering

Publicly defended at Ghent University on November 13, 2015

Research funded by a doctoral grant from the Research Foundation Flanders (FWO)

Supervisors:

prof. dr. ir. H. Rogier
prof. dr. ir. D. De Zutter
Electromagnetics Group
Department of Information Technology
Faculty of Engineering and Architecture
Ghent University
Sint-Pietersnieuwstraat 41
9000 Ghent, Belgium
`http://emweb.intec.ugent.be`

Members of the examination board:

prof. dr. ir. R. Van de Walle (chairman)	Ghent University, Belgium
prof. dr. ir. D. Vande Ginste (secretary)	Ghent University, Belgium
prof. dr. ir. H. Rogier (supervisor)	Ghent University, Belgium
prof. dr. ir. D. De Zutter (supervisor)	Ghent University, Belgium
prof. dr. ir. F. P. Andriulli	Télécom Bretagne, France
prof. dr. ir. K. Cools	University of Nottingham, United Kingdom
dr. ir. J. Sercu	Keysight Technologies, Belgium
prof. dr. M. Slodička	Ghent University, Belgium

Opgedragen aan mijn grootouders

Dankwoord

Vier jaar doctoraatsonderzoek omhelsde onder andere veel papers en boeken lezen, bestaande ideeën en theorieën ontdekken, discussiëren met collega's, eigen vondsten en bijdragen publiceren en presenteren op conferenties, oefeningenlessen geven, maar vooral de vrijheid hebben om nieuwe onderzoeksdomeinen te verkennen. Het was een boeiend en plezant leerproces, waarvan dit proefschrift het belangrijkste resultaat is.

Hendrik en Daniël, bedankt om mij gedurende het onderzoek deskundig te begeleiden. Jullie enthousiasme werkte meer dan eens aanstekelijk. Ik beschouw het als een voorrecht en eer om jullie als promotoren te hebben gehad.

Yves en Ignace, bedankt voor de vele fijne momenten op ons bureau, en voor de interessante uitwisselingen over randintegraalvergelijkingen en snelle-multipoolmethoden.

Steven, bedankt voor de samenwerking op vlak van hybride methoden (en voor het dichten van een fout in het bewijs van stelling 6.2.2). Verder ook bedankt aan alle andere (oud-)collega's.

Bedankt ook aan alle leden van de examencommissie.

Vader, moeder, broer en zus, bedankt voor alles en nog zoveel meer.

Gent, oktober 2015
Dieter Dobbelaere

"Les vraies conquêtes,
les seules qui ne donnent aucun regret,
sont celles que l'on fait sur l'ignorance."

Napoléon Bonaparte

Contents

Samenvatting

Overzicht

De belangrijkste resultaten van het verrichtte wetenschappelijk onderzoek worden voorgesteld in dit proefschrift. In het algemeen handelen ze over het numeriek oplossen van elektromagnetische problemen. Elektromagnetische velden worden opgewekt door bronnen, bijvoorbeeld elektrische ladingen en stromen, en planten zich voort doorheen de ruimte volgens de vergelijkingen van Maxwell (zie hoofdstuk 1). Typisch zijn bij een elektromagnetisch probleem de geometrie, d.w.z. de verdeling en elektromagnetische eigenschappen van materie in de ruimte, en bronnen gekend en is men op zoek naar de opgewekte velden. Slechts voor een beperkt aantal elektromagnetische problemen (bv. verstrooiing aan een perfect geleidende bol in een homogene ruimte*) kan de oplossing geschreven worden als een wiskundige formule met gekende functies. Voor de meeste problemen, waaronder vele praktische antenneproblemen en ingewikkelde geometrieën, is men op zoek naar een benaderde oplossing van de Maxwellvergelijkingen met behulp van een numerieke oplossingsmethode (zoals een eindige-elementen- of randelementenmethode). De benaderde oplossing ligt in een ruimte met eindige dimensie n (grofweg gesproken kan ze enkel veranderen in n mogelijke richtingen), en de hoofdgedachte is dat ze convergeert naar de exacte oplossing als we n laten toenemen (ten koste van hogere berekeningstijden), een eigenschap die bewezen is voor de meeste bestaande numerieke oplossingsmethoden.

Het proefschrift is opgebouwd als volgt. Hoofdstuk 1 voert de heersende vergelijkingen en notaties in die gebruikt worden doorheen het manuscript. De volgende hoofdstukken zijn onderverdeeld in twee delen, die de twee verschillende soorten van onderzochte elektromagnetische problemen weerspiegelen. In het eerste deel wordt een elektromagnetischegolfanalyse van golfgeleiders met meerdere geleiders beschreven. Het tweede deel bespreekt een preconditioneerder voor de Poincaré-Steklov-operator van een heterogeen gebied die het oplossen van verstrooiingsproblemen versnelt.

*Voor de geïnteresseerde lezer: dit komt doordat de Helmholtz-differentiaalvergelijking scheidbaar is in bolcoördinaten (waarin de punten op het boloppervlak een constante radiale coördinaat hebben), wat een mogelijke manier is om de Maxwellvergelijkingen analytisch op te lossen. Er kan aangetoond worden dat er slechts 11 coördinaatsystemen bestaan waarin deze *truc* met scheiding van veranderlijken kan worden toegepast.

Deel I

Talrijke toepassingen, waaronder golfgeleiders verbonden met een antenne of microgolfovencaviteit, elektrische verbindingen op een printplaat, trans-Atlantische optischevezelkabels, coaxkabelnetwerken en hoogspanningsleidingen, steunen op de voortplanting van elektromagnetische golven voor de overbrenging van informatie of energie door een structuur die als onveranderlijk kan worden beschouwd in een bepaalde ruimtelijke richting, bijgenaamd de lengterichting*. Het nauwkeurig voorspellen van alle optredende elektromagnetische verschijnselen, waaronder demping ten gevolge van verliezen, voortplantingssnelheid van golfpakketten, overspraak, (mode)dispersie, verdeling van elektromagnetische energie en gevoeligheid voor elektromagnetische storing, komt in wezen neer op dezelfde vraag: wat is (zijn†) de oplossing(en) van de Maxwellvergelijkingen voor een gegeven tweedimensionale geometrie en een gegeven excitatie. Het eerste deel beoogt het voorstellen van een efficiënt numeriek raamwerk, gebaseerd op een randelementenmethode (REM) voor de elektromagnetischegolfanalyse (d.w.z. vertrekkend vanuit de Maxwellvergelijkingen) van de belangrijke en praktisch relevante klasse van golfgeleiders die bestaan uit stuksgewijs homogene, isotrope en mogelijks goedgeleidende materiaalgebieden.

Het inleidende hoofdstuk 2 heeft tot doel de lezer vertrouwd te maken met de eigenmodeanalyse van golfgeleiders (met meerdere geleiders) in het frequentiedomein. Een opsplitsing van de eigenmodes, op basis van de ligging van hun overeenkomstige voortplantingsconstantes in het complexe vlak, wordt besproken en twee benaderende theorieën voor de bepaling van de fundamentele modes van een golfgeleider met meerdere geleiders, de quasi-TEM- en quasi-TM-analyse, worden in herinnering gebracht.

Technologische vorderingen in halfgeleidergebaseerde informatieverwerkingssystemen gedurende de laatste tientallen jaren, hebben het mogelijk gemaakt voor gebruikers om complexe inhoud (bv. hogeresolutiebeelden, afbeeldingen, spraak) te delen over digitale communicatiekanalen met een hoge bandbreedte‡. Vaak worden de informatiestromen van meerdere gebruikers tegelijk verzonden over dezelfde fysische golfgeleider (bv. optischevezelkabel, coaxkabel, gekoppelde microstripbaantjes), waardoor elektromagnetische golven op nog hogere frequenties vereist zijn om verstoring te vermijden. Aangezien de quasi-TEM-

*sommige klassen van golfgeleiders die niet aan deze voorwaarde voldoen, zoals de wijdverspreide getwistpaarkabel, zijn alsnog gelijkwaardig met een inhomogene anisotrope golfgeleider die onveranderlijk is in de lengterichting langsheen de kabel, na een geschikte coördinatentransformatie

†het bestaan van meerdere oplossingen van de bronloze Maxwellvergelijkingen in het frequentiedomein, genaamd eigenmodes (zie hoofdstuk 2), treedt op nadat de randvoorwaarde op oneindig in de lengterichting wordt verzacht (t.t.z. de oplossingen worden toegelaten om zich te gedragen als een golf *invallend vanuit oneindig*)

‡voor een gegeven signaalvermogen aan de zender en ruisvermogen op het kanaal stijgt de minimaal vereiste bandbreedte in Hz voor het verzenden van een bitstroom met een willekeurig lage kans op fouten als de zendsnelheid in bits/s toeneemt, ten gevolge van de wet van Shannon-Hartley

en quasi-TM-analyse enkel geldig zijn voor voldoende lage frequenties, is er een duidelijke nood aan een elektromagnetischegolfanalyse voor de huidige en toekomstige generatie van geavanceerde hogesnelheidsverbindingen.

Om nauwkeurig alle golfverschijnselen te voorspellen die optreden in geleiders (zoals de gelijkmatige stroomverdeling bij lage frequenties en de ophoping van stroom nabij de randen ten gevolge van het skin- en nabijheidseffect bij hogere frequenties), stelt hoofdstuk 3 een nieuwe methode voor voor de efficiënte berekening van interactie-integralen in een 2.5-D REM, voor willekeurige geleidbaarheden en frequenties.

Een nauwkeurige voorspelling van de voorplantingssnelheid van golfpakketten (die latentie beïnvloedt) en modedispersie (die een lineaire tijdsinvariante vervorming van een golfpakket veroorzaakt naargelang het zich voortplant doorheen de golfgeleider) vereist kennis van de dispersiekrommen van de eigenmodes, m.a.w. van het gedrag van de overeenkomstige voortplantingsconstantes in functie van de frequentie. In hoofdstuk 4 leiden we een aantal analytische eigenschappen af van de numeriek verkregen dispersiekrommen. Deze eigenschappen worden gebruikt in een numeriek raamwerk dat in staat is om de dispersiekrommen en eigenmodeveldverdelingen van golfgeleiders met meerdere geleiders nauwkeurig te bepalen, in functie van de frequentie, zoals geïllustreerd door numerieke voorbeelden. Bovendien wordt de invloed van een verlieshebbende afschermingsgeleider op de complexe modes van een afgeschermde diëlektrische 'beeld'-geleider voor het eerst onderzocht.

Deel II

Men kan gerust stellen dat de twee belangrijkste eigenschappen van een numerieke oplossingsmethode bestaan uit de convergentie naar de exacte oplossing bij een toenemend aantal basisfuncties n, zoals eerder uitgelegd, en de conditie-eigenschappen als functie van n. In essentie is de numerieke oplossing van een grote klasse van lineaire problemen, waaronder de elektromagnetische verstrooiingsproblemen die beschouwd worden in dit deel, de oplossing van een lineair systeem met n vergelijkingen en n onbekenden, voorgesteld door een complexe vierkante matrix M en een complexe rechterlidvector b. In een digitaal opslag- en informatieverwerkingstoestel worden de elementen van M en b afgerond naar een voorstelbaar getal dat behoort tot een eindige verzameling getallen, hetgeen impliceert dat de opgeslagen versies $\tilde{\mathsf{M}}$ en $\tilde{\mathsf{b}}$ over het algemeen verschillen van M en b*. Het conditiegetal van M, d.w.z. de verhouding van de grootste tot de kleinste singuliere waarde, is een belangrijke grootheid voor het schatten van de mogelijke fout van de benaderde oplossing $\tilde{\mathsf{x}} = \tilde{\mathsf{M}}^{-1}\tilde{\mathsf{b}}$ t.o.v. de foutvrije oplossing $\mathsf{x} = \mathsf{M}^{-1}\mathsf{b}$. Als het conditiegetal groot is, *kan* de relatieve fout van $\tilde{\mathsf{x}}$ veel groter zijn dan de relatieve fout van $\tilde{\mathsf{M}}$ en $\tilde{\mathsf{b}}$. Bovendien heeft een hoog conditiegetal de

*een andere bron van fouten vloeit voort uit de benaderde berekening van de elementen

neiging om het aantal iteraties van een iteratief oplossingsalgoritme te verhogen, voor een gegeven nauwkeurigheid*.

Uit de voorgaande beschouwingen volgt dat het wenselijk is dat het conditiegetal van M zo dicht mogelijk bij 1 ligt. Helaas is dit voor veel operatoren, waaronder de gediscretiseerde elektrische-veldintegraaloperator (EVIO) T, gedefinieerd in hoofdstuk 5, en de gediscretiseerde Poincaré-Steklov-operator (PS) P van een heterogeen gebied, gedefinieerd in hoofdstuk 6, niet het geval en blijft het conditiegetal zelfs stijgen voor toenemende n, zonder een maximumwaarde aan te nemen. Een mogelijke oplossing is het voorvermenigvuldigen van het lineaire systeem met een preconditioneerder.

Hoofdstuk 5 bespreekt de belangrijkste wiskundige resultaten die geleid hebben tot een vermenigvuldigende Calderón-preconditioneerder (VCP) A van de EVIO, gebaseerd op een familie van Buffa-Christiansenfuncties die duaal zijn met de Rao-Wilton-Glissonfuncties. Er wordt aangetoond dat het spectrale conditiegetal van AT uniform begrensd is in n.

In hoofdstuk 6 stellen we voor het eerst een VCP voor de PS-operator van een heterogeen gebied voor. Er wordt bewezen dat de continue EVIO de continue PS-operator regulariseert, t.t.z. dat hun product kan geschreven worden als een compacte perturbatie van een goedgeconditioneerde operator, in de geschikte Sobolevruimte. Er wordt numeriek bevestigd dat het conditiegetal van AP begrensd is, onafhankelijk van n. We tonen aan dat de VCP het iteratief oplossen versnelt van een nieuwe herleidde hybride eindige/randelementenmethode, d.i. een numerieke oplossingsmethode voor verstrooiingsproblemen aan een heterogeen gebied ingebed in een homogene ruimte.

*dit is bewezen voor positief-definiete systemen die opgelost worden met de 'conjugate-gradient'-methode; er bestaat tot op heden geen iteratieve methode die *bewijsbaar* goed presteert voor algemene systemen, maar men kan wel stellen dat voor de meeste methodes niet alleen het conditiegetal, maar ook de verdeling van de eigenwaarden in het complexe vlak van belang is (het geval van eigenwaarden die in het rechterhalfvlak liggen is beter dan eigenwaarden die de oorsprong omcirkelen, voor een gegeven conditiegetal)

Summary

Outline

The main results of the conducted scientific research are presented in this dissertation. In general, they concern the numerical solution of electromagnetic problems. Electromagnetic fields are excited by sources, for example electric charges and currents, and propagate through space according to Maxwell's equations (see chapter 1). Typically, in an electromagnetic problem, the geometry, i.e., the distribution and electromagnetic properties of matter in space, and sources are given, and the generated electromagnetic fields are sought for. Only for a few electromagnetic problems (e.g., scattering at a perfectly conducting spherical ball embedded in a homogeneous space*), the solution can be written as a mathematical formula in terms of known functions. For most problems, including many practical antenna problems and complex geometries, an approximate solution to Maxwell's equations is sought for, by using a numerical solution technique (such as a finite element or boundary element method). The approximate solution lies in a space with finite dimension n (loosely speaking, it can only vary in n possible directions), and the principal idea is that it converges to the exact solution if we increase n (at the cost of higher computational times), a property that has been proven for most existing numerical solution techniques.

The dissertation is structured as follows. Chapter 1 introduces the governing equations and notations that are used throughout the manuscript. The subsequent chapters are divided over two parts, which reflect the two distinct types of investigated electromagnetic problems. In the first part, a full-wave analysis of multiconductor waveguides is described. The second part discusses a preconditioner for the Poincaré-Steklov operator of a heterogeneous domain that accelerates the solution of scattering problems.

Part I

Numerous applications, including waveguides connected to an antenna or a microwave oven cavity, signal traces on a printed circuit board, transatlantic

*For the interested reader: this is because the Helmholtz differential equation is separable in spherical coordinates (in which the points on the spherical boundary surface have a constant radial coordinate), which is one way to solve Maxwell's equations analytically. It can be shown that there are only 11 coordinate systems where we can apply this separation of variables *trick*.

optical fiber cables, coaxial cable networks, and overhead power lines, rely on the propagation of electromagnetic waves for the transportation of information or energy through a structure that can be considered invariant in a certain spatial direction, called the longitudinal direction*. Accurate prediction of all occurring electromagnetic phenomena, including attenuation due to losses, propagation speed of wave packets, crosstalk, (modal) dispersion, distribution of electromagnetic energy, and susceptibility to electromagnetic interference, essentially boils down to the same question: what is (are†) the solution(s) to Maxwell's equations for a given two-dimensional geometry and a given excitation. The goal of the first part is to present an efficient numerical framework, based on a boundary element method (BEM), for the full-wave (i.e., starting from Maxwell's equations) modal analysis of the important and practically relevant class of waveguides consisting of piecewise homogeneous isotropic, and possibly highly conductive, material regions.

The introductory chapter 2 aims to acquaint the reader with the frequency-domain modal analysis of (multiconductor) waveguides. A classification of the eigenmodes, based on the location of their corresponding propagation constants in the complex plane, is discussed and two approximative theories for the determination of the fundamental modes of a multiconductor waveguide, the quasi-TEM and quasi-TM analyses, are recalled.

Technological advances of semiconductor-based information processing systems in the past decades, have enabled users to share complex content (e.g. high-definition video, images, voice) using high-bandwidth‡ digital communication channels. Often, the information streams of multiple users are multiplexed over the same physical waveguide (e.g. optical fiber cable, coaxial cable, coupled microstrip lines), which requires the use of electromagnetic waves at even higher frequencies, to avoid interference. As the quasi-TEM/TM analyses are only valid for sufficiently low frequencies, the need for a full-wave analysis of current and future state-of-the-art high-speed interconnects is apparent.

To accurately predict all wave phenomena occurring inside conductors (such as the uniform distribution of the current at low frequencies, and the concentration of current near the edges due to the skin and proximity effect at higher frequencies), chapter 3 presents a novel method for the efficient evaluation of interaction integrals in a 2.5-D BEM, for arbitrary conductivities and frequencies.

---

*some types of waveguides that do not satisfy this condition, such as the ubiquitous twisted pair cable, are still equivalent to an inhomogeneous anisotropic waveguide that is invariant in the longitudinal direction along the cable after a suitable coordinate transformation

†the existence of multiple solutions to the sourceless frequency-domain Maxwell equations, called eigenmodes (see chapter 2), follows after relaxing the boundary condition at infinity in the longitudinal direction (i.e., the solutions are allowed to behave as an *incoming wave from infinity*)

‡for a given power level of the transmitter and noise power level of the channel, the minimal required bandwidth in Hz to transmit a bitstream with arbitrarily low bit error rate, increases with increasing transmission rate in bits/s, by the Shannon-Hartley theorem

Accurate prediction of the propagation speed of wave packets (which influences latency) and modal dispersion (which causes a linear time-invariant deformation of a wave packet as it travels through the waveguide), necessitates knowledge of the dispersion curves of the eigenmodes, i.e., the behavior of the corresponding propagation constants as a function of frequency. In chapter 4, we derive some analytic properties of the numerically obtained dispersion curves. These properties are leveraged in a numerical framework, capable of accurately determining the propagation constants and eigenmode field distributions of multiconductor waveguides as a function of frequency, as illustrated by numerical examples. Moreover, the influence of a lossy shielding conductor on the complex modes of a shielded dielectric image guide is investigated for the first time.

Part II

Arguably, the two most important properties of a numerical solution technique are convergence to the exact solution for an increasing number n of basis functions, as explained earlier, and conditioning properties as a function of n. In essence, for a large class of linear problems, including the electromagnetic scattering problems considered in this part, the numerical solution is the solution of a linear system of n equations with n unknowns, represented by a complex square matrix M, and a complex right hand side vector b. In a digital storage and information processing device, the elements of M and b are rounded to a representable number belonging to a finite set of numbers, implying that the stored versions $\tilde{\mathsf{M}}$ and $\tilde{\mathsf{b}}$ are different from M and b, in general*. The condition number of M, i.e., the ratio of its largest to smallest singular value, is an important parameter for estimating the possible error on the approximate solution $\tilde{\mathsf{x}} = \tilde{\mathsf{M}}^{-1}\tilde{\mathsf{b}}$ w.r.t. the error-free solution $\mathsf{x} = \mathsf{M}^{-1}\mathsf{b}$. If the condition number is large, the relative error of $\tilde{\mathsf{x}}$ *can* be much higher than the relative error of $\tilde{\mathsf{M}}$ and $\tilde{\mathsf{b}}$. Moreover, a high condition number tends to increase the number of iterations of an iterative solution algorithm, for a given precision†.

From the previous considerations, it is desirable that the condition number of M is as close to 1 as possible. Unfortunately, for a lot of operators, including the discretized electric field integral operator (EFIO) T, defined in chapter 5, and the discretized Poincaré-Steklov (PS) operator P of a heterogeneous domain, defined in chapter 6, this is not the case and the condition number even continues to increase without bound for increasing n. A possible remedy is to premultiply the linear system with a preconditioner.

*another source of error originates from the approximate calculation of the elements

†this has been proven for positive definite systems solved by the conjugate gradient method; to date, no iterative method exists that *provably* performs well for general systems, but it can be stated that, for most methods, not only the condition number, but also the distribution of the eigenvalues in the complex plane is important (the case of eigenvalues lying in the right half-plane is better than eigenvalues surrounding the origin, for a given condition number)

Chapter 5 recalls the main mathematical results that have led to a Calderón multiplicative preconditioner (CMP) A of the EFIO, based on a family of Buffa-Christiansen functions that are dual to the Rao-Wilton-Glisson functions. It is shown that the spectral condition number of AT is bounded uniformly in n.

In chapter 6, we present a CMP for the PS operator of a heterogeneous domain, for the first time. It is proven that the continuous EFIO regularizes the continuous PS operator, i.e., that their product can be written as a compact perturbation of a well-conditioned operator, in the appropriate Sobolev space. It is confirmed numerically that the condition number of AP is bounded, independent of n. We show that the CMP accelerates the convergence of the iterative solution of a novel reduced hybrid finite/boundary element method (FEM-BEM), a numerical solution technique for scattering problems at a heterogeneous domain embedded in a homogeneous space.

List of Acronyms

BC	Buffa-Christiansen (functions)
BEM	Boundary Element Method
CFIE	Combined Field Integral Equation
CMP	Calderón Multiplicative Preconditioner
EFIE	Electric Field Integral Equation
EFIO	Electric Field Integral Operator
FEM	Finite Element Method
MCW	Multiconductor Waveguide
MFIE	Magnetic Field Integral Equation
MoM	Method of Moments
MLFMA	Multilevel Fast Multipole Algorithm
PEC	Perfect Electric Conductor
PMC	Perfect Magnetic Conductor
PMCHWT	Poggio-Miller-Chang-Harrington-Wu-Tsai (equation)
PS	Poincaré-Steklov (operator)
RCS	Radar Cross Section
RWG	Rao-Wilton-Glisson (functions)
TE	Transverse Electric
TEM	Transverse Electromagnetic
TM	Transverse Magnetic

List of Symbols

$\mathbb{R}$	set of real numbers	
$\mathbb{C}$	set of complex numbers	
j	imaginary unit	
$\Re\alpha$	real part of α	
$\Im\alpha$	imaginary part of α	
$\overline{\alpha}$	complex conjugate of α	
$\overline{A}$	closure of set A (of elements in a topological space)	
$\mathbf{v}$	vector (field)	
$\lvert\mathbf{v}\rvert$	norm of $\mathbf{v}$	
$\hat{\mathbf{w}}$	unit vector (with $\lvert\hat{\mathbf{w}}\rvert = 1$)	
M	matrix	
$\bar{\bar{T}}$	dyadic (i.e., linear transformation from $\mathbb{C}^3$ to $\mathbb{C}^3$)	
$\triangleq$	by definition equal to	
x, y, z	Cartesian coordinates in three dimensions	
$\hat{\mathbf{x}}, \hat{\mathbf{y}}, \hat{\mathbf{z}}$	Cartesian coordinate vectors	
∂_x, $\frac{\partial}{\partial x}$	partial derivative with respect to x	
$\boldsymbol{\rho}$	$x\hat{\mathbf{x}} + y\hat{\mathbf{y}}$	
$\mathbf{r}$	$x\hat{\mathbf{x}} + y\hat{\mathbf{y}} + z\hat{\mathbf{z}}$	
∇_t	$\partial_x\hat{\mathbf{x}} + \partial_y\hat{\mathbf{y}}$	
∇	$\partial_x\hat{\mathbf{x}} + \partial_y\hat{\mathbf{y}} + \partial_z\hat{\mathbf{z}}$	
δ	Dirac distribution (acting on functions from $\mathbb{R}^n$ to $\mathbb{C}$)	
$H_\alpha^{(2)}$	Hankel function of the second kind of order $\alpha \in \mathbb{C}$	
$L^2(\Omega)$	Hilbert space of square integrable* functions on $\Omega \subset \mathbb{R}^n$	
$\mathbf{L}^2(\Omega)$	$\left(L^2(\Omega)\right)^3$	
t	time	s
$\boldsymbol{E}$	electric field	V/m
$\boldsymbol{H}$	magnetic field	A/m
$\boldsymbol{D}$	dielectric displacement	$\mathrm{C/m^2}$
$\boldsymbol{B}$	magnetic induction	$\mathrm{Wb/m^2}$
$\boldsymbol{J}$	electric current density	$\mathrm{A/m^2}$
$\boldsymbol{M}$	magnetic current density	$\mathrm{V/m^2}$
P	electric charge density	$\mathrm{C/m^3}$
P_m	magnetic charge density	$\mathrm{Wb/m^3}$

*Lebesgue integrability is meant, to ensure the completeness of the space

f	frequency	1/s
ω	angular frequency ($= 2\pi f$)	1/s
$\mathbf{e}$	phasor of time-harmonic* electric field	V/m
$\mathbf{h}$	phasor of time-harmonic magnetic field	A/m
$\mathbf{d}$	phasor of time-harmonic dielectric displacement	C/m^2
$\mathbf{b}$	phasor of time-harmonic magnetic induction	Wb/m^2
$\mathbf{j}$	phasor of time-harmonic electric current density	A/m^2
$\mathbf{m}$	phasor of time-harmonic magnetic current density	V/m^2
ρ	phasor of time-harmonic electric charge density	C/m^3
ρ_m	phasor of time-harmonic magnetic charge density	Wb/m^3
β	propagation constant	1/m
$\mathbf{E}$	phasor of time- and space-harmonic† electric field	V/m
$\mathbf{H}$	phasor of time- and space-harmonic magnetic field	A/m
$\mathbf{D}$	phasor of time- and space-harmonic dielectric displacement	C/m^2
$\mathbf{B}$	phasor of time- and space-harmonic magnetic induction	Wb/m^2
$\mathbf{J}$	phasor of time- and space-harmonic electric current density	A/m^2
$\mathbf{M}$	phasor of time- and space-harmonic magnetic current density	V/m^2
P	phasor of time- and space-harmonic electric charge density	C/m^3
P_m	phasor of time- and space-harmonic magnetic charge density	Wb/m^3
ϵ, $\bar{\bar{\epsilon}}$	permittivity (dyadic)	F/m
μ, $\bar{\bar{\mu}}$	permeability (dyadic)	H/m
k	wavenumber ($= \omega\sqrt{\epsilon\mu}$)	1/m
γ	transversal wavenumber ($= \sqrt{k^2 - \beta^2}$)	1/m
$G(\boldsymbol{\rho})$	two-dimensional Green's function‡ ($= -\frac{j}{4}H_0^{(2)}(\gamma\lvert\boldsymbol{\rho}\rvert)$)	
$g(\mathbf{r})$	three-dimensional Green's function§ ($= \frac{e^{-jk\lvert\mathbf{r}\rvert}}{4\pi\lvert\mathbf{r}\rvert}$)	

*time factor $e^{j\omega t}$, with $\omega \in \mathbb{C}$

†space factor $e^{-j\beta z}$, with $\beta \in \mathbb{C}$

‡note the upper case, by analogy with the two-dimensional phasor fields

§note the lower case, by analogy with the three-dimensional phasor fields

List of Publications

Articles in International Journals

- D. Dobbelaere, H. Rogier, and D. De Zutter, "Properties and numerical solutions of dispersion curves in general isotropic waveguides", *IEEE Transactions on Microwave Theory and Techniques*, vol. 61, no. 9, pp. 3161–3168, 2013.
- D. Dobbelaere, H. Rogier, and D. De Zutter, "Accurate 2.5-D boundary element method for conductive media", *Radio Science*, vol. 49, no. 6, pp. 389–399, 2014.
- D. Dobbelaere, D. D. Zutter, J. V. Hese, J. Sercu, T. Boonen, and H. Rogier, "A Calderón multiplicative preconditioner for the electromagnetic Poincaré-Steklov operator of a heterogeneous domain with scattering applications", *Journal of Computational Physics*, `http://dx.doi.org/10.1016/j.jcp.2015.09.052`, 2015.

Articles in Conference Proceedings

- D. Dobbelaere, H. Rogier, and D. De Zutter, "Accurate 2D MoM technique for arbitrary dielectric, magnetic and conducting media applied to shielding problems", in *URSI International Symposium on Electromagnetic Theory*, Hiroshima, Japan: IEEE, 2013, pp. 738–741.
- D. Dobbelaere, H. Rogier, and D. De Zutter, "Analytic properties of dispersion curves for efficient eigenmode analysis of isotropic waveguides using a boundary element method", in *Proceedings of the IEEE International Conference on Numerical Electromagnetic Modeling and Optimization for RF, Microwave, and Terahertz Applications*, Pavia, Italy: IEEE, 2014, pp. 1–4.
- F. Boeykens, H. Rogier, D. Dobbelaere, J. Van Hese, J. Sercu, and T. Boonen, "Identification of the Poincaré-Steklov operator in hybrid FE-BIE formulations for the analysis of internal resonances", in *Book of Abstracts of the 6th International Conference on Advanced Computational Methods in Engineering*, R. De Staelen and M. Slodička, Eds., Ghent, Belgium: Ghent University, Faculty of Engineering and Architecture, Department of Mathematical Analysis, 2014, pp. 163–164.

Scientific Award

Second Prize at the Student Paper Contest of the IEEE International Conference on Numerical Electromagnetic Modeling and Optimization for RF, Microwave, and Terahertz Applications, Pavia, Italy, May 2014

IEEE Microwave Theory and Techniques Society, 2014

Full-Wave Multiconductor Waveguide Analysis and a Calderón Preconditioner for the Heterogeneous Poincaré-Steklov Operator

1 Introduction

★ ★ ★

"Changing electric fields produce magnetic fields, and changing magnetic fields produce electric fields. Thus these fields can animate one another in turn, giving birth to self-reproducing disturbances that travel at the speed of light. Ever since Maxwell, we understand that these disturbances are what light is."

Frank Wilczek, *The Lightness of Being*

1.1 Maxwell's equations

1.1.1 Time domain equations

The interactions between the electric field $\boldsymbol{E}$ in V/m, the magnetic field $\boldsymbol{H}$ in A/m, the dielectric displacement $\boldsymbol{D}$ in $\mathrm{C/m^2}$, the magnetic induction $\boldsymbol{B}$ in $\mathrm{Wb/m^2}$, the electric current density $\boldsymbol{J}$ in $\mathrm{A/m^2}$, the electric charge density P in $\mathrm{C/m^3}$, the magnetic current density* $\boldsymbol{M}$ in $\mathrm{V/m^2}$ and the magnetic charge density P_m in $\mathrm{Wb/m^3}$ (the last two quantities have not yet been experimentally observed, but are added to make the equations more symmetric) as a function of space and time, are governed by Maxwell's equations [2], written (under some mild and mostly valid assumptions, such as flat spacetime and negligible quantum effects) as a system of coupled linear partial differential equations in (1.1)–(1.4). These equations were first postulated, albeit in a different but

*note that we adopt the sign convention of [1], which allows us to write the Calderón projectors in Section 1.3 as mappings from $\begin{pmatrix}\mathbf{m}\\ \mathbf{j}\end{pmatrix}$ to $\begin{pmatrix}\hat{\mathbf{n}}\times\mathbf{e}\\ \hat{\mathbf{n}}\times\mathbf{h}\end{pmatrix}$

equivalent formulation, by the Scottish physicist James Clerk Maxwell in the nineteenth century [3].

$$\nabla \times \boldsymbol{E}(\mathbf{r},t) = -\partial_t \boldsymbol{B}(\mathbf{r},t) + \boldsymbol{M}(\mathbf{r},t) \tag{1.1}$$
$$\nabla \times \boldsymbol{H}(\mathbf{r},t) = \partial_t \boldsymbol{D}(\mathbf{r},t) + \boldsymbol{J}(\mathbf{r},t) \tag{1.2}$$
$$\nabla \cdot \boldsymbol{D}(\mathbf{r},t) = P(\mathbf{r},t) \tag{1.3}$$
$$\nabla \cdot \boldsymbol{B}(\mathbf{r},t) = P_m(\mathbf{r},t) \tag{1.4}$$

1.1.2 Time-harmonic equations

In this thesis, all quantities are assumed to behave sinusoidally in time, with the same* angular frequency $\omega = 2\pi f$. In that case Maxwell's equations reduce to (1.5)–(1.8), after introducing complex phasors (written in lowercase, e.g. $\boldsymbol{E}(\mathbf{r},t) = \Re[\mathbf{e}(\mathbf{r})e^{j\omega t}]$). This frequency domain formulation is commonly used for the description of narrow-band systems (e.g. the calculation of antenna properties).

$$\nabla \times \mathbf{e}(\mathbf{r}) = -j\omega\mathbf{b}(\mathbf{r}) + \mathbf{m}(\mathbf{r}) \tag{1.5}$$
$$\nabla \times \mathbf{h}(\mathbf{r}) = j\omega\mathbf{d}(\mathbf{r}) + \mathbf{j}(\mathbf{r}) \tag{1.6}$$
$$\nabla \cdot \mathbf{d}(\mathbf{r}) = \rho(\mathbf{r}) \tag{1.7}$$
$$\nabla \cdot \mathbf{b}(\mathbf{r}) = \rho_m(\mathbf{r}) \tag{1.8}$$

The properties of the material (e.g. dielectrics, conductors or (ferro)-magnetic materials) in which the fields exist, define the relations between the fields and the inductions†. In this thesis, the occurring media are considered *locally reacting*, *linear* and *time-invariant* (we further refrain from so-called bi-materials, i.e. $\mathbf{e}$ and $\mathbf{h}$ only depend on $\mathbf{d}$ and $\mathbf{b}$, respectively), leading to the constitutive equations (1.9)–(1.10), with $\bar{\bar{\epsilon}}$ and $\bar{\bar{\mu}}$ the permittivity and permeability dyadics, respectively.

$$\mathbf{d}(\mathbf{r}) = \bar{\bar{\epsilon}}(\mathbf{r}) \cdot \mathbf{e}(\mathbf{r}) \tag{1.9}$$
$$\mathbf{b}(\mathbf{r}) = \bar{\bar{\mu}}(\mathbf{r}) \cdot \mathbf{h}(\mathbf{r}) \tag{1.10}$$

Sometimes we additionally assume that the materials are *isotropic*, leading to the constitutive equations (1.11)–(1.12), with $\epsilon \in \mathbb{C}$ and $\mu \in \mathbb{C}$ the permittivity and permeability, respectively.

$$\mathbf{d}(\mathbf{r}) = \epsilon(\mathbf{r})\mathbf{e}(\mathbf{r}) \tag{1.11}$$
$$\mathbf{b}(\mathbf{r}) = \mu(\mathbf{r})\mathbf{h}(\mathbf{r}) \tag{1.12}$$

*note that this additionally assumes time invariance of the constitutive equations and boundary conditions, preventing e.g. the movement of scatterers w.r.t. the introduced Cartesian coordinate system

†let us call $\mathbf{e}$ and $\mathbf{h}$ the fields, $\mathbf{d}$ and $\mathbf{b}$ the inductions, $\mathbf{j}$ and $\mathbf{m}$ the currents and ρ and ρ_m the charges

1.1.3 Time- and space-harmonic equations

In Part I, we investigate solutions of Maxwell's equations (1.5)–(1.8) for translation invariant structures*, i.e., structures for which $\partial_z \bar{\bar{\epsilon}}(\boldsymbol{\rho}) = \partial_z \bar{\bar{\mu}}(\boldsymbol{\rho}) = \bar{\bar{0}}$, that have an $e^{-j\beta z}$ dependence ($\beta \in \mathbb{C}$). It is easy to show that the phasor fields (written in non-italic upper case, i.e. $\mathbf{e}(\mathbf{r}) = \mathbf{E}(\boldsymbol{\rho})e^{-j\beta z}$, implying that $\boldsymbol{E}(\mathbf{r},t) = \Re[\mathbf{e}(\mathbf{r})e^{j\omega t}] = \Re[\mathbf{E}(\boldsymbol{\rho})e^{j(\omega t-\beta z)}]$) satisfy (1.13)–(1.16), with $\nabla_t = \partial_x\hat{\mathbf{x}} + \partial_y\hat{\mathbf{y}}$.

$$(\nabla_t - j\beta\hat{\mathbf{z}}) \times \mathbf{E}(\boldsymbol{\rho}) = -j\omega\mathbf{B}(\boldsymbol{\rho}) + \mathbf{M}(\boldsymbol{\rho}) \tag{1.13}$$

$$(\nabla_t - j\beta\hat{\mathbf{z}}) \times \mathbf{H}(\boldsymbol{\rho}) = j\omega\mathbf{D}(\boldsymbol{\rho}) + \mathbf{J}(\boldsymbol{\rho}) \tag{1.14}$$

$$(\nabla_t - j\beta\hat{\mathbf{z}}) \cdot \mathbf{D}(\boldsymbol{\rho}) = \mathrm{P}(\boldsymbol{\rho}) \tag{1.15}$$

$$(\nabla_t - j\beta\hat{\mathbf{z}}) \cdot \mathbf{B}(\boldsymbol{\rho}) = \mathrm{P}_m(\boldsymbol{\rho}) \tag{1.16}$$

Denoting† $\mathbf{E}(\boldsymbol{\rho}) = \mathbf{E}_t(\boldsymbol{\rho}) + E_z(\boldsymbol{\rho})\hat{\mathbf{z}}$ (and likewise for the other fields), the curl equations (1.13)–(1.14) further reduce to (1.17)–(1.20).

$$\nabla_t \times \mathbf{E}_t(\boldsymbol{\rho}) = -j\omega B_z(\boldsymbol{\rho})\hat{\mathbf{z}} + M_z(\boldsymbol{\rho})\hat{\mathbf{z}} \tag{1.17}$$

$$-j\beta\hat{\mathbf{z}} \times \mathbf{E}_t(\boldsymbol{\rho}) + \nabla_t \times E_z(\boldsymbol{\rho})\hat{\mathbf{z}} = -j\omega\mathbf{B}_t(\boldsymbol{\rho}) + \mathbf{M}_t(\boldsymbol{\rho}) \tag{1.18}$$

$$\nabla_t \times \mathbf{H}_t(\boldsymbol{\rho}) = j\omega D_z(\boldsymbol{\rho})\hat{\mathbf{z}} + J_z(\boldsymbol{\rho})\hat{\mathbf{z}} \tag{1.19}$$

$$-j\beta\hat{\mathbf{z}} \times \mathbf{H}_t(\boldsymbol{\rho}) + \nabla_t \times H_z(\boldsymbol{\rho})\hat{\mathbf{z}} = j\omega\mathbf{D}_t(\boldsymbol{\rho}) + \mathbf{J}_t(\boldsymbol{\rho}) \tag{1.20}$$

1.2 Function spaces

It is natural to ask to which set of functions the fields and inductions belong (we restrict ourselves to the three-dimensional time-harmonic phasor fields). Let us consider a bounded domain $\Omega \subset \mathbb{R}^3$ with boundary Γ and outward unit normal $\hat{\mathbf{n}}$ (Fig. 1.1). For square integrable volume sources $\mathbf{m}(\mathbf{r})$, $\mathbf{j}(\mathbf{r})$, $\rho(\mathbf{r})$ and $\rho_m(\mathbf{r})$, the total electric and magnetic energy inside Ω is finite, implying that the electric and magnetic fields belong to the Sobolev space (see e.g. [4] or the introductory chapters of [5] for an introduction to functional analysis) $\mathbf{H}(\mathsf{curl}, \Omega)$ with elements $\mathbf{u} : \Omega \to \mathbb{C}^3$, defined in (1.21), with $\mathbf{L}^2(\Omega) = (L^2(\Omega))^3$ the Hilbert space of square integrable vector functions (distributions, in fact) on Ω and all derivatives considered in distributional sense (see [6] for the specific Sobolev spaces introduced in this section).

$$\mathbf{e}, \mathbf{h} \in \mathbf{H}(\mathsf{curl}, \Omega) = \left\{\mathbf{u} \in \mathbf{L}^2(\Omega) \mid \nabla \times \mathbf{u} \in \mathbf{L}^2(\Omega)\right\} \tag{1.21}$$

For square integrable sources, the inductions, as well as the currents, belong to $\mathbf{H}(\mathsf{div}, \Omega)$.

$$\mathbf{d}, \mathbf{b}, \mathbf{j}, \mathbf{m} \in \mathbf{H}(\mathsf{div}, \Omega) = \left\{\mathbf{u} \in \mathbf{L}^2(\Omega) \mid \nabla \cdot \mathbf{u} \in L^2(\Omega)\right\} \tag{1.22}$$

*if assumed, translation invariance is along the z dimension

†$\mathbf{E}_t$ is called the *transversal* component, i.e., $\mathbf{E}_t \cdot \hat{\mathbf{z}} = 0$, and E_z the *longitudinal* component

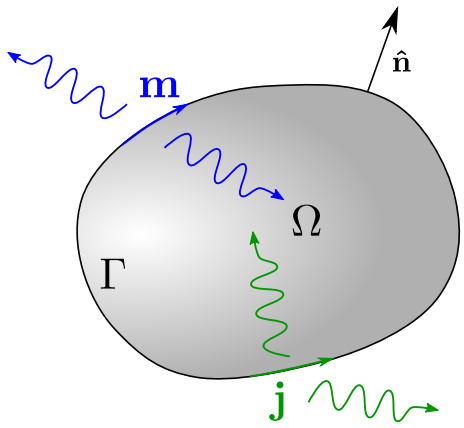

Figure 1.1: Domain $\Omega \subset \mathbb{R}^3$ with currents $\mathbf{j}, \mathbf{m}$ flowing on its boundary Γ and generating fields in $\mathbb{R}^3$.

In the following section, we define some operators that operate on *boundary* functions, i.e., restrictions of the fields to the boundary Γ. We are thus interested in the *trace* space of $\mathbf{H}(\mathsf{curl}, \Omega)$. Under the rather technical assumption of Lipschitz continuity (see e.g. [5] for a definition) of Γ, there exists a continuous and surjective trace operator γ_t that maps $\mathbf{H}(\mathsf{curl}, \Omega)$ onto the *tangential* trace space* $\mathbf{H}^{-\frac{1}{2}}(\mathsf{div}_\Gamma, \Gamma)$ (see [7] for the subtler details and precise definition for Lipschitz domains).

$$\mathbf{H}^{-\frac{1}{2}}(\mathsf{div}_\Gamma, \Gamma) = \{\boldsymbol{\psi} \in \mathbf{H}^{-\frac{1}{2}}(\Gamma) \mid \boldsymbol{\psi} \cdot \hat{\mathbf{n}} = 0 \text{ and } \nabla_\Gamma \cdot \boldsymbol{\psi} \in H^{-\frac{1}{2}}(\Gamma)\} \quad (1.23)$$

Indeed, we cannot simply evaluate a given electric field $\mathbf{e} \in \mathbf{H}(\mathsf{curl}, \Omega)$ at the boundary by evaluating $\hat{\mathbf{n}} \times \mathbf{e}$ on Γ, as this makes no sense in the distributional context (i.e., we can change the field on a set with zero measure, for example on the surface Γ, without altering the distribution it represents). However, mostly because the considered distributions in practice have a continuous representative in the neighborhood of Γ, we will not ensue these technicalities in this thesis and colloquially refer to $\gamma_t \mathbf{e}$ as $\hat{\mathbf{n}} \times \mathbf{e}|_\Gamma$.

The fields and inductions in $\mathbb{R}^3 \setminus \overline{\Omega}$ belong to spaces with *locally* square integrable densities (and curl or divergence, respectively). We refer to [6] for more details.

It should be noted that in most cases we consider current densities $\mathbf{j}, \mathbf{m}$ flowing on the boundary, but this will be clear from the context. Thus, with slight abuse of notation we write $\mathbf{j}, \mathbf{m} \in \mathbf{H}^{-\frac{1}{2}}(\mathsf{div}_\Gamma, \Gamma)$ for *surface* current densities in A/m and V/m, respectively.

*note that, for notational convenience, we refrain from the subscript t used by some authors

1.3 Calderón projectors

In this section, some boundary integral operators that map tangential current densities to their excited tangential boundary fields in a homogeneous isotropic domain (i.e., with constant ϵ and μ) will be defined. We introduce the so-called Calderón projectors in three dimensions, which will be used in Part II, and the Fourier transformed equivalent operators for translation-invariant structures, which will be used for the waveguide analysis in Part I.

1.3.1 Time-harmonic fields

Consider a homogeneous isotropic space $\mathbb{R}^3$ (i.e., constant ϵ and μ), with tangential current densities $\mathbf{j}, \mathbf{m} \in \mathbf{H}^{-\frac{1}{2}}(\mathsf{div}_\Gamma, \Gamma)$ flowing on the boundary Γ of a bounded Lipschitzian domain Ω (Fig. 1.1). The currents generate fields in $\Omega^- \triangleq \Omega$ and $\Omega^+ \triangleq \mathbb{R}^3 \setminus \overline{\Omega}$, called the interior and exterior domain, respectively. The exterior and interior traces of the (rotated) tangential electric and magnetic field are given by

$$\lim_{\Omega^\pm \ni \mathbf{r} \to \Gamma} \begin{pmatrix} \hat{\mathbf{n}} \times \mathbf{e} \\ \hat{\mathbf{n}} \times \mathbf{h} \end{pmatrix} = \mathbb{P}^\pm \begin{pmatrix} \mathbf{m} \\ \mathbf{j} \end{pmatrix}, \ \mathbb{P}^\pm = \begin{pmatrix} \mathcal{K}_k \pm \frac{1}{2} & -\eta \mathcal{T}_k \\ \mathcal{T}_k/\eta & \mathcal{K}_k \pm \frac{1}{2} \end{pmatrix}, \tag{1.24}$$

with $\eta = \sqrt{\mu/\epsilon}$ the impedance of the homogeneous medium, $\mathbb{P}^+$ and $\mathbb{P}^-$ the exterior and interior Calderón projectors, respectively [1], [6], and the operators $\mathcal{T}_k : \mathbf{H}^{-\frac{1}{2}}(\mathsf{div}_\Gamma, \Gamma) \to \mathbf{H}^{-\frac{1}{2}}(\mathsf{div}_\Gamma, \Gamma)$ and $\mathcal{K}_k : \mathbf{H}^{-\frac{1}{2}}(\mathsf{div}_\Gamma, \Gamma) \to \mathbf{H}^{-\frac{1}{2}}(\mathsf{div}_\Gamma, \Gamma)$ given by*

$$\begin{aligned} \mathcal{T}_k : \mathbf{m} \mapsto \hat{\mathbf{n}} \times jk \int_\Gamma g(\mathbf{r} - \mathbf{r}') \mathbf{m}(\mathbf{r}') \mathrm{d}S' \\ - \hat{\mathbf{n}} \times \frac{1}{jk} \int_\Gamma \nabla g(\mathbf{r} - \mathbf{r}') \nabla' \cdot \mathbf{m}(\mathbf{r}') \mathrm{d}S', \end{aligned} \tag{1.25}$$

$$\mathcal{K}_k : \mathbf{m} \mapsto \hat{\mathbf{n}} \times \left[\nabla \times \int_\Gamma g(\mathbf{r} - \mathbf{r}') \mathbf{m}(\mathbf{r}') \mathrm{d}S' \right], \tag{1.26}$$

with $k = \omega\sqrt{\epsilon\mu}$ the wavenumber and $g(\mathbf{r} - \mathbf{r}') = e^{-jk|\mathbf{r}-\mathbf{r}'|}/(4\pi|\mathbf{r} - \mathbf{r}'|)$ the Green's function of the three-dimensional scalar Helmholtz operator that satisfies the Sommerfeld radiation condition and the distributional equation

$$\nabla^2 g(\mathbf{r}) + k^2 g(\mathbf{r}) = -\delta(\mathbf{r}). \tag{1.27}$$

The projector property $(\mathbb{P}^\pm)^2 = \mathbb{P}^\pm$ immediately implies the so-called Calderón identities

$$\mathcal{T}_k \mathcal{K}_k + \mathcal{K}_k \mathcal{T}_k = 0, \tag{1.28}$$

$$\mathcal{K}_k^2 - \mathcal{T}_k^2 = \frac{1}{4}. \tag{1.29}$$

*all integrals are considered in Cauchy principal value sense, i.e., as the limit for $\delta \to 0$ of the integrals over the surface $\Gamma \setminus \Gamma_\delta$, with Γ_δ the intersection of Γ with a ball with radius δ, centered around the singularity $\mathbf{r} \in \Gamma$ of the integrands [2]

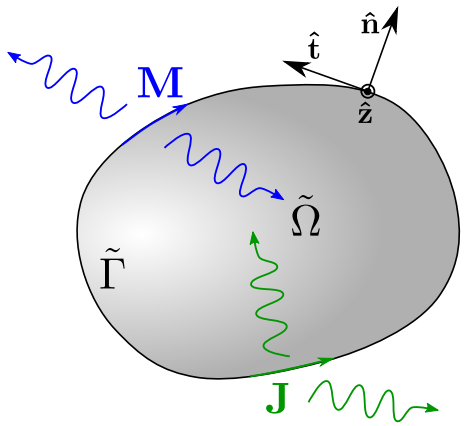

Figure 1.2: Cross-section $\tilde{\Omega} \subset \mathbb{R}^2$ of a translation-invariant structure with currents $\mathbf{J}, \mathbf{M}$ flowing on its boundary $\tilde{\Gamma}$ and generating fields in $\mathbb{R}^3$.

1.3.2 Time- and space-harmonic fields

If the structure of Fig. 1.1 is translation-invariant (denote $\tilde{\Omega} \subset \mathbb{R}^2$ and $\tilde{\Gamma}$ as the restrictions of Ω and Γ to the cross sectional (x, y) plane, $\tilde{\Omega}^- \triangleq \tilde{\Omega}$ and $\tilde{\Omega}^+ \triangleq \mathbb{R}^2 \setminus \overline{\tilde{\Omega}}$, as shown in Fig. 1.2) and the sources and fields have an $e^{-j\beta z}$ dependence, Maxwell's equations (1.13)–(1.16) hold. Equation (1.24) reduces to

$$\lim_{\tilde{\Omega}^\pm \ni \boldsymbol{\rho} \to \tilde{\Gamma}} \begin{pmatrix} \hat{\mathbf{n}} \times \mathbf{E} \\ \hat{\mathbf{n}} \times \mathbf{H} \end{pmatrix} = \tilde{\mathbb{P}}^\pm \begin{pmatrix} \mathbf{M} \\ \mathbf{J} \end{pmatrix}, \quad \tilde{\mathbb{P}}^\pm = \begin{pmatrix} \tilde{\mathcal{K}}_k \pm \frac{1}{2} & -\eta \tilde{\mathcal{T}}_k \\ \tilde{\mathcal{T}}_k / \eta & \tilde{\mathcal{K}}_k \pm \frac{1}{2} \end{pmatrix}, \tag{1.30}$$

with $\tilde{\mathbb{P}}^\pm$ the 2.5-D* Calderón projectors and†

$$\begin{aligned} \tilde{\mathcal{T}}_k : \mathbf{M} \mapsto \hat{\mathbf{n}} \times jk \int_{\tilde{\Gamma}} G(\boldsymbol{\rho} - \boldsymbol{\rho}') \mathbf{M}(\boldsymbol{\rho}') \mathrm{d}c' \\ - \hat{\mathbf{n}} \times \frac{1}{jk} \int_{\tilde{\Gamma}} (\nabla_t - j\beta\hat{\mathbf{z}}) G(\boldsymbol{\rho} - \boldsymbol{\rho}') (\nabla_t' - j\beta\hat{\mathbf{z}}) \cdot \mathbf{M}(\boldsymbol{\rho}') \mathrm{d}c', \end{aligned} \tag{1.31}$$

$$\tilde{\mathcal{K}}_k : \mathbf{M} \mapsto \hat{\mathbf{n}} \times \left[(\nabla_t - j\beta\hat{\mathbf{z}}) \times \int_{\tilde{\Gamma}} G(\boldsymbol{\rho} - \boldsymbol{\rho}') \mathbf{M}(\boldsymbol{\rho}') \mathrm{d}c' \right], \tag{1.32}$$

with $\gamma = \sqrt{k^2 - \beta^2}$ the transversal wavenumber‡ and $G(\boldsymbol{\rho} - \boldsymbol{\rho}') = -\frac{j}{4} H_0^{(2)}(\gamma |\boldsymbol{\rho} - \boldsymbol{\rho}'|)$ the Green's function of the two-dimensional scalar Helmholtz operator that

*although the geometry is translation-invariant, the fields have a longitudinal dependence $e^{-j\beta z}$, implying that Maxwell's equations do not split into purely 2-D TE and TM equations

†all integrals are considered in Cauchy principal value sense, i.e., as the limit for $\delta \to 0$ of the integrals over the surface $\tilde{\Gamma} \setminus \tilde{\Gamma}_\delta$, with $\tilde{\Gamma}_\delta$ the intersection of $\tilde{\Gamma}$ with a disc with radius δ, centered around the singularity $\boldsymbol{\rho} \in \tilde{\Gamma}$ of the integrands

‡the branch cuts are chosen on the hyperbola in the β plane such that $\Im\gamma \leq 0$ and the Sommerfeld radiation condition of the Green's function is satisfied

satisfies the Sommerfeld radiation condition and the distributional equation

$$\nabla_t^2 G(\boldsymbol{\rho}) + \gamma^2 G(\boldsymbol{\rho}) = -\delta(\boldsymbol{\rho}). \tag{1.33}$$

Proof. Introducing $\mathbf{m}(\mathbf{r}') = \mathbf{M}(\boldsymbol{\rho}')e^{-j\beta z'}$ into (1.26) leads, with $r = |\boldsymbol{\rho} - \boldsymbol{\rho}'|$ and $|\mathbf{r} - \mathbf{r}'| = \sqrt{r^2 + (z - z')^2}$, to

$$\begin{aligned}
\mathcal{K}_k(\mathbf{m})(\mathbf{r}) &= \hat{\mathbf{n}} \times \left[\nabla \times \int_\Gamma g(\mathbf{r} - \mathbf{r}') \mathbf{M}(\boldsymbol{\rho}') e^{-j\beta z'} \mathrm{d}S' \right] \\
&= \hat{\mathbf{n}} \times \left[\nabla \times \int_{\tilde{\Gamma}} \mathbf{M}(\boldsymbol{\rho}') \mathrm{d}c' \int_{-\infty}^{\infty} \frac{e^{-jk\sqrt{r^2+(z-z')^2}}}{4\pi\sqrt{r^2+(z-z')^2}} e^{-j\beta z'} dz' \right] \\
&= \hat{\mathbf{n}} \times \left[\nabla \times \int_{\tilde{\Gamma}} \mathbf{M}(\boldsymbol{\rho}') e^{-j\beta z} \mathrm{d}c' \int_{-\infty}^{\infty} \frac{e^{-jkr\sqrt{1+u^2}}}{4\pi\sqrt{1+u^2}} e^{-j\beta r u} du \right] \\
&= \hat{\mathbf{n}} \times \left[\nabla \times \int_{\tilde{\Gamma}} \mathbf{M}(\boldsymbol{\rho}') e^{-j\beta z} \mathrm{d}c' \int_{-\infty}^{\infty} \frac{1}{4\pi} e^{-jr(k\cosh v + \beta \sinh v)} dv \right] \\
&= \hat{\mathbf{n}} \times \left[\nabla \times \int_{\tilde{\Gamma}} \frac{-j}{4} H_0^{(2)}(r\sqrt{k^2-\beta^2}) \mathbf{M}(\boldsymbol{\rho}') e^{-j\beta z} \mathrm{d}c' \right] \\
&= \tilde{\mathcal{K}}_k(\mathbf{M})(\boldsymbol{\rho}) e^{-j\beta z},
\end{aligned}$$

where we made the substitutions $(z - z')/r = u = \sinh v$ and the penultimate step follows from [8, equation 10.9.16]. Completely similar, one shows that $\mathcal{T}_k(\mathbf{m})(\mathbf{r}) = \tilde{\mathcal{T}}_k(\mathbf{M})(\boldsymbol{\rho}) e^{-j\beta z}$, for $\mathbf{m}(\mathbf{r}') = \mathbf{M}(\boldsymbol{\rho}') e^{-j\beta z'}$. □

1.4 Representation formulas

The following representation formulas* (1.34)–(1.37), which will be used in Part I, express relations between the transverse tangential (subscript t) and longitudinal (subscript z) components of the phasors of the time- and space-harmonic total electric and magnetic field $\mathbf{E} = E_t\hat{\mathbf{t}} + E_n\hat{\mathbf{n}} + E_z\hat{\mathbf{z}}$ and $\mathbf{H} = H_t\hat{\mathbf{t}} + H_n\hat{\mathbf{n}} + H_z\hat{\mathbf{z}}$, respectively, and the incoming electric and magnetic field $\mathbf{E}^{(i)} = E_t^{(i)}\hat{\mathbf{t}} + E_n^{(i)}\hat{\mathbf{n}} + E_z^{(i)}\hat{\mathbf{z}}$ and $\mathbf{H}^{(i)} = H_t^{(i)}\hat{\mathbf{t}} + H_n^{(i)}\hat{\mathbf{n}} + H_z^{(i)}\hat{\mathbf{z}}$ due to sources in $\tilde{\Omega}^-$, respectively, expanded in the local orthogonal coordinate system on the

*the integrals of the terms in $\frac{\partial^2 G(\boldsymbol{\rho}-\boldsymbol{\rho}')}{\partial n \partial n'}$ are interpreted in Hadamard finite part sense (or, equivalently, as the limit of the integrals for $\boldsymbol{\rho} \to \tilde{\Gamma}$), all other integrals are considered in Cauchy principal value sense, i.e., as the limit for $\delta \to 0$ of the integrals over the surface $\tilde{\Gamma} \setminus \tilde{\Gamma}_\delta$, with $\tilde{\Gamma}_\delta$ the intersection of $\tilde{\Gamma}$ with a disc with radius δ, centered around the singularity $\boldsymbol{\rho} \in \tilde{\Gamma}$ of the integrands

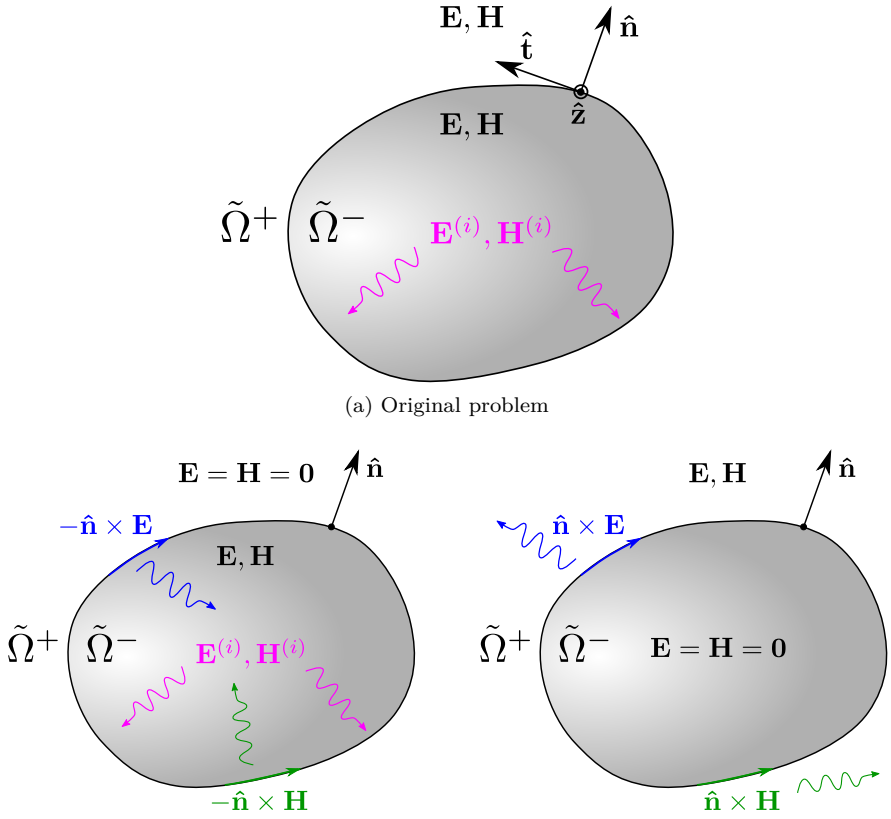

(a) Original problem

(b) Equivalent interior problem

(c) Equivalent exterior problem

Figure 1.3: Homogeneous domain $\tilde{\Omega}^-$, embedded in a (possibly inhomogeneous) domain $\tilde{\Omega}^+$, with incoming fields $\mathbf{E}^{(i)}$ and $\mathbf{H}^{(i)}$ and total fields $\mathbf{E}$ and $\mathbf{H}$

boundary $\tilde{\Gamma}$ with $\hat{\mathbf{n}} = \hat{\mathbf{t}} \times \hat{\mathbf{z}}$ the outward unit normal vector (see Fig. 1.3(a)).

$$\begin{aligned}\frac{1}{2}E_z(\boldsymbol{\rho}) = E_z^{(i)}(\boldsymbol{\rho}) - \oint_{\tilde{\Gamma}} \Bigg[& E_z(\boldsymbol{\rho}') \frac{\partial G(\boldsymbol{\rho}-\boldsymbol{\rho}')}{\partial n'} \\ & + \left(\frac{j\gamma^2}{\omega\epsilon} H_t(\boldsymbol{\rho}') - \frac{\beta}{\omega\epsilon} \frac{\partial H_z(\boldsymbol{\rho}')}{\partial t'} \right) G(\boldsymbol{\rho}-\boldsymbol{\rho}') \Bigg] \, \mathrm{d}c' \end{aligned} \tag{1.34}$$

$$\begin{aligned}\frac{1}{2}E_t(\boldsymbol{\rho}) = E_t^{(i)}(\boldsymbol{\rho}) + \oint_{\tilde{\Gamma}} \Bigg[& \frac{j\beta}{\gamma^2} E_z(\boldsymbol{\rho}') \frac{\partial^2 G(\boldsymbol{\rho}-\boldsymbol{\rho}')}{\partial t \partial n'} - \frac{j\omega\mu}{\gamma^2} H_z(\boldsymbol{\rho}') \frac{\partial^2 G(\boldsymbol{\rho}-\boldsymbol{\rho}')}{\partial n \partial n'} \\ & + \frac{j\omega\mu}{\gamma^2} \left(\frac{j\gamma^2}{\omega\mu} E_t(\boldsymbol{\rho}') - \frac{\beta}{\omega\mu} \frac{\partial E_z(\boldsymbol{\rho}')}{\partial t'} \right) \frac{\partial G(\boldsymbol{\rho}-\boldsymbol{\rho}')}{\partial n} \\ & + \frac{j\beta}{\gamma^2} \left(\frac{j\gamma^2}{\omega\epsilon} H_t(\boldsymbol{\rho}') - \frac{\beta}{\omega\epsilon} \frac{\partial H_z(\boldsymbol{\rho}')}{\partial t'} \right) \frac{\partial G(\boldsymbol{\rho}-\boldsymbol{\rho}')}{\partial t} \Bigg] \, \mathrm{d}c' \end{aligned} \tag{1.35}$$

$$\frac{1}{2}H_z(\boldsymbol{\rho}) = H_z^{(i)}(\boldsymbol{\rho}) - \oint_{\tilde{\Gamma}} \left[H_z(\boldsymbol{\rho}') \frac{\partial G(\boldsymbol{\rho}-\boldsymbol{\rho}')}{\partial n'} - \left(\frac{j\gamma^2}{\omega\mu} E_t(\boldsymbol{\rho}') - \frac{\beta}{\omega\mu} \frac{\partial E_z(\boldsymbol{\rho}')}{\partial t'} \right) G(\boldsymbol{\rho}-\boldsymbol{\rho}') \right] \mathrm{d}c' \tag{1.36}$$

$$\begin{aligned} \frac{1}{2}H_t(\boldsymbol{\rho}) = H_t^{(i)}(\boldsymbol{\rho}) + \oint_{\tilde{\Gamma}} \Bigg[& \frac{j\beta}{\gamma^2} H_z(\boldsymbol{\rho}') \frac{\partial^2 G(\boldsymbol{\rho}-\boldsymbol{\rho}')}{\partial t \partial n'} + \frac{j\omega\epsilon}{\gamma^2} E_z(\boldsymbol{\rho}') \frac{\partial^2 G(\boldsymbol{\rho}-\boldsymbol{\rho}')}{\partial n \partial n'} \\ & + \frac{j\omega\epsilon}{\gamma^2} \left(\frac{j\gamma^2}{\omega\epsilon} H_t(\boldsymbol{\rho}') - \frac{\beta}{\omega\epsilon} \frac{\partial H_z(\boldsymbol{\rho}')}{\partial t'} \right) \frac{\partial G(\boldsymbol{\rho}-\boldsymbol{\rho}')}{\partial n} \\ & - \frac{j\beta}{\gamma^2} \left(\frac{j\gamma^2}{\omega\mu} E_t(\boldsymbol{\rho}') - \frac{\beta}{\omega\mu} \frac{\partial E_z(\boldsymbol{\rho}')}{\partial t'} \right) \frac{\partial G(\boldsymbol{\rho}-\boldsymbol{\rho}')}{\partial t} \Bigg] \mathrm{d}c' \end{aligned} \tag{1.37}$$

Formula (1.34) can be easily derived from (1.30)–(1.32), as shown below.

Proof of (1.34). The total interior fields $\mathbf{E}$ and $\mathbf{H}$ and incoming fields $\mathbf{E}^{(i)}$ and $\mathbf{H}^{(i)}$ of the original problem of Fig. 1.3(a) and the equivalent interior problem of Fig. 1.3(b) are equal. Therefore, we introduce equivalent sources $\mathbf{M} = -\hat{\mathbf{n}} \times \mathbf{E}$ and $\mathbf{J} = -\hat{\mathbf{n}} \times \mathbf{H}$ on the boundary $\tilde{\Gamma}$ and denote the fields excited by these sources as $(\mathbf{E}^{(s)}, \mathbf{H}^{(s)})$ (called *scattered*), implying that $(\mathbf{E}, \mathbf{H}) = (\mathbf{E}^{(s)}, \mathbf{H}^{(s)}) + (\mathbf{E}^{(i)}, \mathbf{H}^{(i)})$. By (1.30) the scattered electric field in $\tilde{\Omega}$ is given by (note that $\hat{\mathbf{z}}' = \hat{\mathbf{z}}$, whereas $\hat{\mathbf{t}}'$ and $\hat{\mathbf{n}}'$ depend on $\boldsymbol{\rho}'$)

$$\hat{\mathbf{n}} \times \mathbf{E}^{(s)} = E_t^{(s)} \hat{\mathbf{z}} - E_z^{(s)} \hat{\mathbf{t}} \tag{1.38}$$

$$= \left(\tilde{\mathcal{K}}_k - \frac{1}{2} \right) (E_z \hat{\mathbf{t}}' - E_t \hat{\mathbf{z}}) - \eta \tilde{\mathcal{T}}_k (H_z \hat{\mathbf{t}}' - H_t \hat{\mathbf{z}}), \tag{1.39}$$

implying that

$$E_z^{(s)} = \hat{\mathbf{t}} \cdot \left[\left(\tilde{\mathcal{K}}_k - \frac{1}{2} \right) (E_t \hat{\mathbf{z}} - E_z \hat{\mathbf{t}}') - \eta \tilde{\mathcal{T}}_k (H_t \hat{\mathbf{z}} - H_z \hat{\mathbf{t}}') \right]. \tag{1.40}$$

The term $\hat{\mathbf{t}} \cdot \left(\tilde{\mathcal{K}}_k - \frac{1}{2} \right) E_t \hat{\mathbf{z}}$ vanishes, as $\hat{\mathbf{t}} \cdot \hat{\mathbf{z}} = 0$ and

$$\hat{\mathbf{t}} \cdot \tilde{\mathcal{K}}_k (E_t \hat{\mathbf{z}}) = \hat{\mathbf{t}} \cdot \left(\hat{\mathbf{n}} \times \left[(\nabla_t - j\beta \hat{\mathbf{z}}) \times \int_{\tilde{\Gamma}} G(\boldsymbol{\rho}-\boldsymbol{\rho}') E_t(\boldsymbol{\rho}') \hat{\mathbf{z}} \, \mathrm{d}c' \right] \right) \tag{1.41}$$

$$= \hat{\mathbf{t}} \cdot \left(\hat{\mathbf{n}} \times (\kappa(\boldsymbol{\rho}) \hat{\mathbf{t}} + \lambda(\boldsymbol{\rho}) \hat{\mathbf{n}}) \right) \tag{1.42}$$

$$= 0. \tag{1.43}$$

The term $-\hat{\mathbf{t}} \cdot \tilde{\mathcal{K}}_k(E_z\hat{\mathbf{t}}')$ is equal to

$$-\hat{\mathbf{t}} \cdot \tilde{\mathcal{K}}_k(E_z\hat{\mathbf{t}}') = -\hat{\mathbf{t}} \cdot \left(\hat{\mathbf{n}} \times \left[(\nabla_t - j\beta\hat{\mathbf{z}}) \times \int_{\tilde{\Gamma}} G(\boldsymbol{\rho}-\boldsymbol{\rho}')E_z(\boldsymbol{\rho}')\hat{\mathbf{t}}' \, \mathrm{d}c'\right]\right) \tag{1.44}$$

$$= -\hat{\mathbf{t}} \cdot \left(\hat{\mathbf{n}} \times \left[\int_{\tilde{\Gamma}} \nabla_t G(\boldsymbol{\rho}-\boldsymbol{\rho}') \times (E_z(\boldsymbol{\rho}')\hat{\mathbf{t}}') \, \mathrm{d}c'\right]\right) \tag{1.45}$$

$$= -\hat{\mathbf{t}} \cdot \left(\hat{\mathbf{n}} \times \left[\int_{\tilde{\Gamma}} (E_z(\boldsymbol{\rho}')\hat{\mathbf{t}}') \times \nabla_t' G(\boldsymbol{\rho}-\boldsymbol{\rho}') \, \mathrm{d}c'\right]\right) \tag{1.46}$$

$$= -\hat{\mathbf{t}} \cdot \left(\hat{\mathbf{n}} \times \left[\int_{\tilde{\Gamma}} (E_z(\boldsymbol{\rho}')\hat{\mathbf{t}}') \times (\partial_{t'} G\hat{\mathbf{t}}' + \partial_{n'} G\hat{\mathbf{n}}') \, \mathrm{d}c'\right]\right) \tag{1.47}$$

$$= -\int_{\tilde{\Gamma}} \frac{\partial G(\boldsymbol{\rho}-\boldsymbol{\rho}')}{\partial n'} E_z(\boldsymbol{\rho}')\mathrm{d}c'. \tag{1.48}$$

The term $-\eta\hat{\mathbf{t}} \cdot \tilde{\mathcal{T}}_k(H_z\hat{\mathbf{t}}')$ is equal to

$$-\eta\hat{\mathbf{t}} \cdot \tilde{\mathcal{T}}_k(H_z\hat{\mathbf{t}}') = \eta\hat{\mathbf{t}} \cdot \left(\hat{\mathbf{n}} \times \frac{1}{jk}\int_{\tilde{\Gamma}} (\nabla_t - j\beta\hat{\mathbf{z}}) G(\boldsymbol{\rho}-\boldsymbol{\rho}')\partial_{t'} H_z(\boldsymbol{\rho}')\mathrm{d}c'\right) \tag{1.49}$$

$$= \frac{\beta}{\omega\epsilon}\int_{\tilde{\Gamma}} G(\boldsymbol{\rho}-\boldsymbol{\rho}')\frac{\partial H_z(\boldsymbol{\rho}')}{\partial t'}\mathrm{d}c'. \tag{1.50}$$

The term $\eta\hat{\mathbf{t}} \cdot \tilde{\mathcal{T}}_k(H_t\hat{\mathbf{z}})$ is equal to

$$\eta\hat{\mathbf{t}} \cdot \tilde{\mathcal{T}}_k(H_t\hat{\mathbf{z}}) = j\eta\left(k - \frac{\beta^2}{k}\right)\hat{\mathbf{t}} \cdot \left(\hat{\mathbf{n}} \times \int_{\tilde{\Gamma}} G(\boldsymbol{\rho}-\boldsymbol{\rho}')H_t(\boldsymbol{\rho}')\hat{\mathbf{z}} \, \mathrm{d}c'\right) \tag{1.51}$$

$$= -\frac{j\gamma^2}{\omega\epsilon}\int_{\tilde{\Gamma}} G(\boldsymbol{\rho}-\boldsymbol{\rho}')H_t(\boldsymbol{\rho}')\mathrm{d}c'. \tag{1.52}$$

Substituting (1.48), (1.50) and (1.52) into (1.40) leads to

$$E_z^{(s)} = \frac{1}{2}E_z - \int_{\tilde{\Gamma}} \left[E_z(\boldsymbol{\rho}')\frac{\partial G(\boldsymbol{\rho}-\boldsymbol{\rho}')}{\partial n'} + \left(\frac{j\gamma^2}{\omega\epsilon}H_t(\boldsymbol{\rho}') - \frac{\beta}{\omega\epsilon}\frac{\partial H_z(\boldsymbol{\rho}')}{\partial t'}\right)G(\boldsymbol{\rho}-\boldsymbol{\rho}')\right]\mathrm{d}c'. \tag{1.53}$$

Together with $E_z = E_z^{(i)} + E_z^{(s)}$, (1.34) follows. □

Formulas (1.36)–(1.37) follow from the duality substitutions $\mathbf{E} \to \mathbf{H}$, $\mathbf{H} \to -\mathbf{E}$, $\mathbf{E}^{(i)} \to \mathbf{H}^{(i)}$, $\mathbf{H}^{(i)} \to -\mathbf{E}^{(i)}$ and $\epsilon \leftrightarrow \mu$ in (1.34)–(1.35).

The identities (1.54)–(1.57) follow from $\lim_{\tilde{\Omega}^- \ni \boldsymbol{\rho} \to \tilde{\Gamma}} [(\nabla_t - j\beta\hat{\mathbf{z}}) \times \mathbf{E} + j\omega\mu\mathbf{H}] = 0$ and $\lim_{\tilde{\Omega}^- \ni \boldsymbol{\rho} \to \tilde{\Gamma}} [(\nabla_t - j\beta\hat{\mathbf{z}}) \times \mathbf{H} - j\omega\epsilon\mathbf{E}] = 0$ (and mutatis mutandis for the incoming

fields*).

$$E_t = \frac{j\omega\mu}{\gamma^2}\frac{\partial H_z}{\partial n} - \frac{j\beta}{\gamma^2}\frac{\partial E_z}{\partial t} \tag{1.54}$$

$$H_t = -\frac{j\omega\epsilon}{\gamma^2}\frac{\partial E_z}{\partial n} - \frac{j\beta}{\gamma^2}\frac{\partial H_z}{\partial t} \tag{1.55}$$

$$E_t^{(i)} = \frac{j\omega\mu}{\gamma^2}\frac{\partial H_z^{(i)}}{\partial n} - \frac{j\beta}{\gamma^2}\frac{\partial E_z^{(i)}}{\partial t} \tag{1.56}$$

$$H_t^{(i)} = -\frac{j\omega\epsilon}{\gamma^2}\frac{\partial E_z^{(i)}}{\partial n} - \frac{j\beta}{\gamma^2}\frac{\partial H_z^{(i)}}{\partial t} \tag{1.57}$$

Substituting (1.34) and (1.36) into (1.54) leads, together with (1.56), to formula (1.35).

*note that this additionally assumes that incident fields are excited by sources that vanish in a neighborhood of $\tilde{\Gamma}$

References

[1] J. Nédélec, *Acoustic and Electromagnetic Equations: Integral Representations for Harmonic Problems*. Springer, 2001.

[2] J. Van Bladel, *Electromagnetic Fields*. John Wiley & Sons, 2007, IEEE Press Series on Electromagnetic Wave Theory.

[3] J. Clerk Maxwell, "A dynamical theory of the electromagnetic field", *Philosophical Transactions of the Royal Society of London*, vol. 155, pp. 459–512, 1865.

[4] R. A. Adams and J. J. Fournier, *Sobolev Spaces*. Elsevier, 2003, Pure and Applied Mathematics.

[5] S. Sauter and C. Schwab, *Boundary Element Methods*. Springer, 2010, Springer Series in Computational Mathematics.

[6] A. Buffa and R. Hiptmair, "Galerkin boundary element methods for electromagnetic scattering", in *Topics in Computational Wave Propagation*, M. Ainsworth, P. Davies, D. Duncan, B. Rynne, and P. Martin, Eds., vol. 31, Lecture Notes in Computational Science and Engineering, Springer Berlin Heidelberg, 2003, pp. 83–124.

[7] A. Buffa, M. Costabel, and D. Sheen, "On traces for H(curl,Ω) in Lipschitz domains", *Journal of Mathematical Analysis and Applications*, vol. 276, no. 2, pp. 845 –867, 2002.

[8] F. W. Olver, D. W. Lozier, R. F. Boisvert, and C. W. Clark, *NIST Handbook of Mathematical Functions*. New York, NY, USA: Cambridge University Press, 2010.

Part I

Full-wave Multiconductor Waveguide Analysis

2

Multiconductor Waveguides

★ ★ ★

This chapter aims to acquaint the reader with the eigenmode analysis of waveguides consisting of a finite number of conductors embedded in piecewise homogeneous isotropic dielectrics. Approximative theories, such as the quasi-TEM and quasi-TM analyses, are presented and the need for a full-wave analysis, which will be elaborated in subsequent chapters, is emphasized.

2.1 Introduction

Consider a uniform waveguide, i.e., a structure in $\mathbb{R}^3$ whose material parameters are invariant in the so-called *longitudinal* direction (assume that it coincides with the $\hat{\mathbf{z}}$ axis of a Cartesian coordinate system, Fig. 2.1). Assume further that all occurring media are isotropic (for an extension of the results in this chapter to (bi)-anisotropic media, we refer to [1]), implying that the waveguide is completely characterized by the functions $\epsilon(\boldsymbol{\rho})$ and $\mu(\boldsymbol{\rho})$, representing the permittivity and permeability in the cross section, respectively (with $\boldsymbol{\rho} = x\hat{\mathbf{x}} + y\hat{\mathbf{y}} \in \mathbb{R}^2$). In most practical cases, these functions are piecewise constant, which has the benefit that their corresponding waveguides can be numerically solved via a boundary element method (BEM), as explained in subsequent chapters.

With $\{\Omega_i \mid 0 \leq i \leq N\}$ a finite partition of $\mathbb{R}^2$ with $N+1$ *connected* components (i.e. Ω_i is open and connected, $\cup_i \overline{\Omega_i} = \mathbb{R}^2$ and $\Omega_i \cap \Omega_j = \emptyset$ unless $i = j$) and $\Omega_{i>0}$ bounded (i.e. the only unbounded domain is Ω_0), we restrict ourselves in

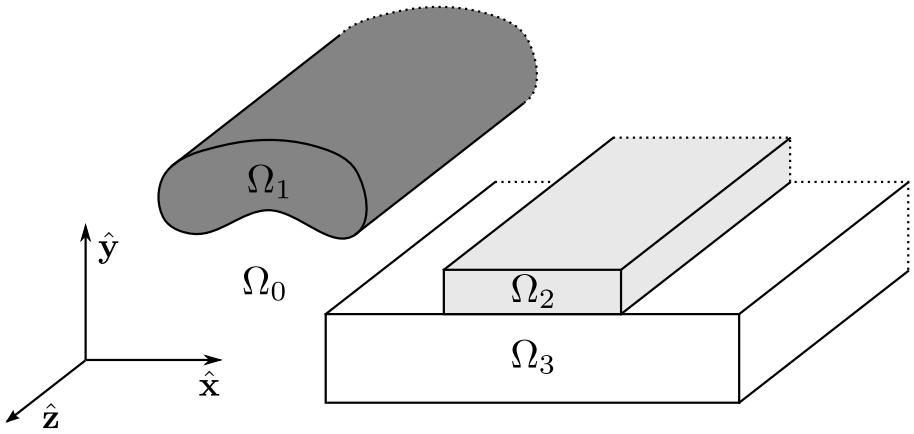

Figure 2.1: Geometry of a uniform waveguide with piecewise constant material parameters

this thesis to the following subset of uniform waveguides*:

$$\begin{cases} \epsilon(\boldsymbol{\rho} \in \Omega_i) & = \epsilon_i \in \mathbb{C}_0 \cup \infty, \\ \mu(\boldsymbol{\rho} \in \Omega_i) & = \mu_i \in \mathbb{C}_0 \cup \infty. \end{cases} \tag{2.1}$$

From here on, we use the term *waveguide* for a uniform waveguide that satisfies assumption (2.1). Note that the isotropic property of the media implies that all considered waveguides are *reciprocal*.

A waveguide is called *lossless* if $\forall i : \epsilon_i, \mu_i \in \mathbb{R} \cup \infty$, and *lossy* if $\forall i : \Im\epsilon_i, \Im\mu_i \geq 0$ and $\exists j : \Im\epsilon_j > 0$ or $\Im\mu_j > 0$.

A waveguide is called *closed* if $\epsilon_0 = \infty$ or $\mu_0 = \infty$ (or if Ω_0 is a good electric or magnetic conductor, implying that $|\epsilon_0| \approx \infty$ or $|\mu_0| \approx \infty$), otherwise it is called *open*.

An electric *multiconductor waveguide* (MCW) is a waveguide with N_c electric conductors $\Omega_{c(i)}$ $(1 \leq i \leq N_c)$. A *perfect electric* multiconductor waveguide is an MCW with perfect electric conductors, i.e., with $\epsilon_{c(i)} = \infty$. A perfect electric MCW can be lossless or lossy (depending on whether there are dielectric losses), an imperfect electric MCW is necessarily lossy† (Fig. 2.2).

The coaxial cable in Fig. 2.3 is an example of a closed MCW with $N_c = 2$ conductors (dashed regions). The coupled microstrip lines in Fig. 2.4 are an example of an open MCW with $N_c = 3$ conductors.

*the cases $\epsilon = \infty$ and $\mu = \infty$ correspond to perfect electric and magnetic conductors, respectively

†for simplicity and because they are rarely used in practice, we do not consider materials with gain (with either $\Im\epsilon_i < 0$ or $\Im\mu_i < 0$)

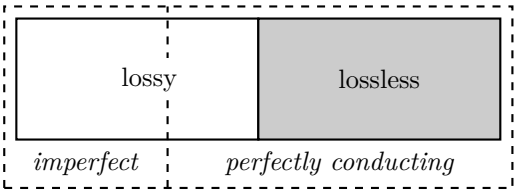

Figure 2.2: Classification of electric multiconductor waveguides

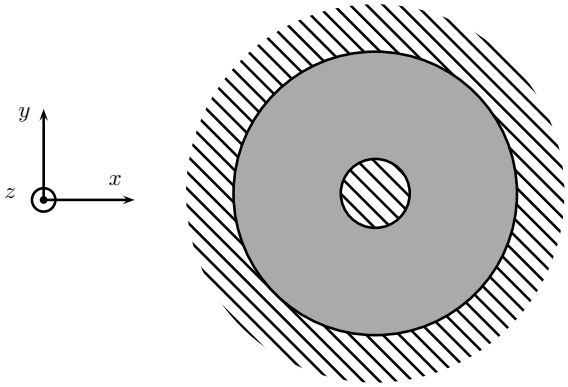

Figure 2.3: Coaxial cable with unbounded outer conductor

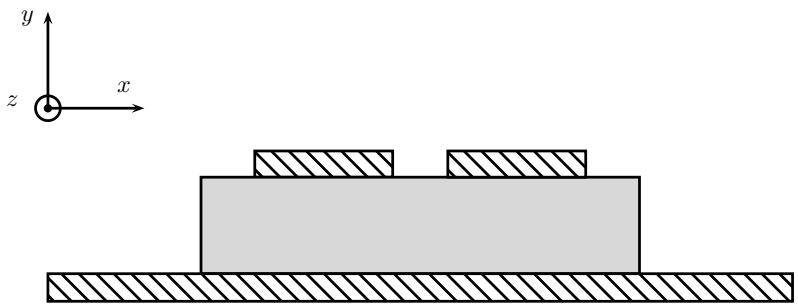

Figure 2.4: Coupled microstrip lines on a bounded substrate

2.2 Eigenmodes

2.2.1 Definitions and properties

For certain $\beta \in \mathbb{C}$, there exist non-zero solutions of the sourceless (i.e., with $\mathbf{M} = \mathbf{J} = 0$ and $\mathrm{P} = \mathrm{P}_m = 0$) time- and space-harmonic Maxwell equations (1.13)–(1.16). Such a solution $(\mathbf{E}, \mathbf{H})$ is called an *eigenmode* of the waveguide

with *propagation constant* β, i.e., if (2.2)–(2.5) hold.

$$\nabla_t \times \mathbf{E}_t(\boldsymbol{\rho}) = -j\omega\mu(\boldsymbol{\rho})H_z(\boldsymbol{\rho})\hat{\mathbf{z}} \tag{2.2}$$

$$-j\beta\hat{\mathbf{z}} \times \mathbf{E}_t(\boldsymbol{\rho}) + \nabla_t \times E_z(\boldsymbol{\rho})\hat{\mathbf{z}} = -j\omega\mu(\boldsymbol{\rho})\mathbf{H}_t(\boldsymbol{\rho}) \tag{2.3}$$

$$\nabla_t \times \mathbf{H}_t(\boldsymbol{\rho}) = j\omega\epsilon(\boldsymbol{\rho})E_z(\boldsymbol{\rho})\hat{\mathbf{z}} \tag{2.4}$$

$$-j\beta\hat{\mathbf{z}} \times \mathbf{H}_t(\boldsymbol{\rho}) + \nabla_t \times H_z(\boldsymbol{\rho})\hat{\mathbf{z}} = j\omega\epsilon(\boldsymbol{\rho})\mathbf{E}_t(\boldsymbol{\rho}) \tag{2.5}$$

It is easy to show that if $(\mathbf{E}_t + E_z\hat{\mathbf{z}}, \mathbf{H}_t + H_z\hat{\mathbf{z}})$ is an eigenmode with propagation constant β, then $(\mathbf{E}_t - E_z\hat{\mathbf{z}}, -\mathbf{H}_t + H_z\hat{\mathbf{z}})$ is another eigenmode with propagation constant $-\beta$. This property of the considered waveguides is called *bidirectionality*.

The number of linearly independent eigenmodes with the same propagation constant β is called the *multiplicity* of the propagation constant, denoted $\nu(\beta)$.

An eigenmode $(\mathbf{E}, \mathbf{H})$ is called a *guided* eigenmode if $(\mathbf{E}, \mathbf{H}) \in \mathbf{L}^2(\mathbb{R}^2)^2$, i.e., if its cross-sectional field distributions are square integrable.

Denote the wavenumber and transversal wavenumber in region Ω_i as $k_i = \omega\sqrt{\epsilon_i\mu_i}$ and $\gamma_i = \sqrt{k_i^2 - \beta^2}$, respectively. The branch cuts of γ_0 as a function of β are chosen on the hyperbola through the branch points $\pm k_0$ with the real and imaginary axes as asymptotes, implying that $\Im\gamma_0 \leq 0$ and that the Green's function $G_0(\boldsymbol{\rho}) = -\frac{j}{4}H_0^{(2)}(\gamma_0|\boldsymbol{\rho} - \boldsymbol{\rho}'|)$ remains bounded for arbitrarily large $|\boldsymbol{\rho} - \boldsymbol{\rho}'|$ [1].

2.2.2 Distribution of propagation constants

Fig. 2.5 shows the distribution of possible propagation constants in the complex plane for different types of waveguides, at a fixed frequency ω.

The propagation constants of a lossless closed waveguide form an infinite set of discrete points (Fig. 2.5(a)). A finite number of guided modes have a real propagation constant and are called *propagating*. They transport, or propagate, electromagnetic energy in the longitudinal direction without attenuation, as their fields have an $e^{-j\beta z}$ dependence (with $\beta \in \mathbb{R}$). An infinite number of discrete propagation constants is located on the imaginary axis. They represent *evanescent* eigenmodes, whose fields decay exponentially in the longitudinal direction. As the frequency increases, the imaginary propagation constants move along the imaginary axis towards the origin. When they reach the origin, at the so-called *cut-off frequency*, they move to the real axis: the evanescent mode transforms into a propagating mode. In certain closed lossless inhomogeneous waveguides, discrete modes appear with complex propagation constants (non-zero real and imaginary parts) at certain frequencies [2]. They constitute an intriguing class of *complex* modes and are further explored numerically in chapter 4.

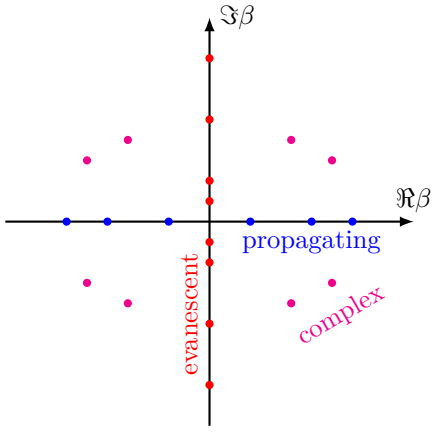

(a) lossless closed waveguide

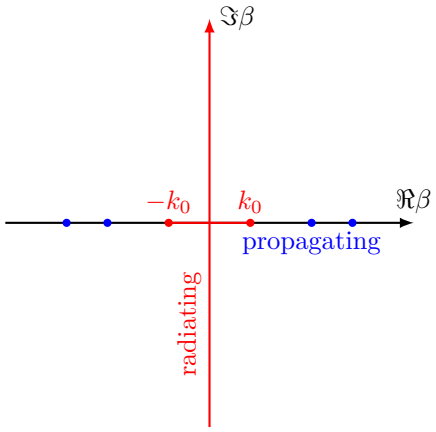

(b) lossless open waveguide

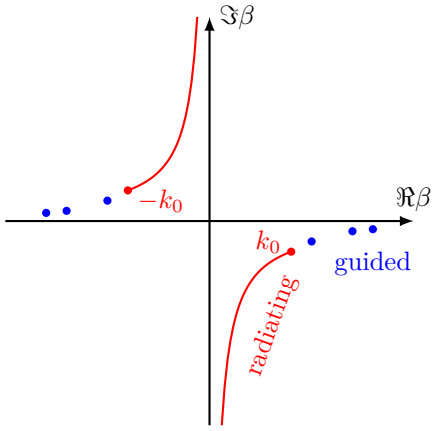

(c) lossy open waveguide

Figure 2.5: Distribution of possible propagation constants for different types of waveguides (at a fixed frequency ω)

The propagation constants of a lossless open waveguide split into two classes. Similarly to the lossless closed waveguide, a finite* number of guided modes have a real propagation constant [3] and are called *propagating*. It can be shown that these propagation constants are restricted to the interval $]k_0, \max_i k_i[$ [3]. Their fields decay exponentially as a function of the distance to the waveguide core $\mathbb{R}^2 \setminus \Omega_0$, with Ω_0 the unbounded background medium (see section 2.1). Fundamental differences with the closed waveguide are the lack of complex modes and discrete evanescent modes in exchange for a continuous set of *radiation modes*. Their propagation constants are located on the branch cut of γ_0 such that $\Im\gamma_0 \leq 0$, i.e., the union of the interval $[-k_0, k_0]$ and the imaginary axis (Fig. 2.5(b)).

The propagation constants of a *lossy* open waveguide can be viewed as a perturbation of those from its lossless counterpart. A finite number of discrete *guided*† modes now have a complex propagation constant, whose imaginary part represents the attenuation of the modes due to losses (Fig. 2.5(c)). For a lossy background medium Ω_0, the continuous set of propagation constants of the radiation modes lies on the hyperbola with the real and imaginary axes as asymptotes [1].

For a discussion of the distribution of propagation constants in other types of waveguides, e.g. those with layered structures (whose layers introduce additional branch cuts which represent *surface waves*), we refer to [1].

2.2.3 Fundamental modes

In an MCW with N_c conductors, there are $N_c - 1$ modes that are called *fundamental modes*‡ [1]. They belong to the class of propagating or guided eigenmodes (see section 2.2.2), depending on whether the MCW is lossless or lossy. They exist for all frequencies $\omega \geq 0$ and reduce to the static $N_c - 1$ dimensional space of the N_c current carrying wires at $\omega = 0$ (under the constraint of equal total forward and backward currents to avoid charge accumulation at infinity).

2.3 Quasi-TEM analysis

In this section, we investigate the fundamental modes $(\mathbf{E}^n, \mathbf{H}^n)$ (with $1 \leq n \leq N_c - 1$) of a perfect electric MCW. At low frequencies, we show that $E_z^n \approx 0$ and $H_z^n \approx 0$ (if the MCW consists, besides perfect electric conductors, of dielectrics with material parameters of the form (2.11)–(2.12)) and call the fundamental modes *quasi-TEM* (quasi transverse electromagnetic).

*each of the finite number of real propagation constants has a finite multiplicity [3]

†note that we reserve the qualifier *propagating* for real propagation constants

‡this is under the assumption that the conductors are not touching; the touching of two or more conductors reduces the number of fundamental modes

We note that $E_z^n = H_z^n = 0\ \forall\omega \geq 0$ only if for every two touching dielectric regions Ω_i and Ω_j it holds that $\epsilon_i\mu_i = \epsilon_j\mu_j$ (MCWs with a single homogeneous dielectric region are a special case), in which case the modes are called *TEM* (see [1] for a proof).

Consider an eigenmode $(\mathbf{E}, \mathbf{H})$ with propagation constant β. As we are interested in the low-frequency behavior, we expand the fields, propagation constant and material parameters as a Taylor series around $\omega = 0$*. Since $\boldsymbol{E}(\mathbf{r}, t) = \Re[\mathbf{e}(\mathbf{r}, \omega)e^{j\omega t}] = \Re[\mathbf{e}(\mathbf{r}, -\omega)e^{-j\omega t}]$, it follows that $\mathbf{e}(\mathbf{r}, \omega) = \overline{\mathbf{e}(\mathbf{r}, -\omega)}$, with $\overline{\alpha}$ the complex conjugate of $\alpha \in \mathbb{C}$. By $\mathbf{e}(\mathbf{r}, \omega) = \mathbf{E}(\boldsymbol{\rho}, \omega)e^{-j\beta(\omega)z}$, it follows that $\mathbf{E}(\boldsymbol{\rho}, \omega) = \overline{\mathbf{E}(\boldsymbol{\rho}, -\omega)}$ and $\beta(\omega) = -\overline{\beta(-\omega)}$. Completely similar, one shows that $\mathbf{H}(\boldsymbol{\rho}, \omega) = \overline{\mathbf{H}(\boldsymbol{\rho}, -\omega)}$. This implies that $\mathbf{E}^R \triangleq \Re\mathbf{E}$, $\mathbf{H}^R \triangleq \Re\mathbf{H}$ and $\beta^I \triangleq \Im\beta$ are even functions of ω, whereas $\mathbf{E}^I \triangleq \Im\mathbf{E}$, $\mathbf{E}^I \triangleq \Im\mathbf{H}$ and $\beta^R \triangleq \Re\beta$ are odd functions of ω. This leads to the Taylor expansions (2.6)–(2.10) (note that we omit the dependence on $\boldsymbol{\rho}$ of the fields and material parameters for notational convenience).

$$\mathbf{E}_t(\omega) = \sum_{i=0}^{+\infty} \omega^{2i} \left[\mathbf{E}_{t,i}^R + j\omega\mathbf{E}_{t,i}^I\right] \tag{2.6}$$

$$E_z(\omega) = \sum_{i=0}^{+\infty} \omega^{2i} \left[E_{z,i}^R + j\omega E_{z,i}^I\right] \tag{2.7}$$

$$\mathbf{H}_t(\omega) = \sum_{i=0}^{+\infty} \omega^{2i} \left[\mathbf{H}_{t,i}^R + j\omega\mathbf{H}_{t,i}^I\right] \tag{2.8}$$

$$H_z(\omega) = \sum_{i=0}^{+\infty} \omega^{2i} \left[H_{z,i}^R + j\omega H_{z,i}^I\right] \tag{2.9}$$

$$\beta(\omega) = \sum_{i=0}^{+\infty} \omega^{2i} \left[\beta_i^I + j\omega\beta_i^R\right] \tag{2.10}$$

Since $\epsilon(\omega)$ and $\mu(\omega)$ are the Fourier transforms of real impulse responses, it holds that $\epsilon(\omega) = \overline{\epsilon(-\omega)}$ and $\mu(\omega) = \overline{\mu(-\omega)}$. Assume that the material parameters are given by (2.11)–(2.12), with $\epsilon^R \triangleq \Re\epsilon$, $\epsilon^I \triangleq \Im\epsilon$, $\mu^R \triangleq \Re\mu$ and $\mu^I \triangleq \Im\mu$ independent of ω. In case there are (semi)-conducting material regions with finite conductivity σ, the permittivity is given by $\epsilon(\omega) = \epsilon^R - j\sigma/\omega$, and the quasi-TM analysis of section 2.4 is appropriate.

$$\epsilon(\omega) = \epsilon^R + j\omega\epsilon^I \tag{2.11}$$

$$\mu(\omega) = \mu^R + j\omega\mu^I \tag{2.12}$$

From a static analysis, it follows that $E_{z,0}^R = H_{z,0}^R$ vanish and, since there is no propagation at $\omega = 0$, that β_0^I also vanishes [1]. Note that this implies that, for

*the subsequent analysis and derivation are inspired by [1]

sufficiently low frequencies, $(\mathbf{E}_t, \mathbf{H}_t) \sim 1$ and $(E_z, H_z) \sim \omega$, justifying the term *quasi-TEM*.

$$E_{z,0}^R = H_{z,0}^R = \beta_0^I = 0 \tag{2.13}$$

Substituting (2.6)–(2.12) into (2.2)–(2.5), equating terms of the same order in ω and using (2.13) leads to (2.14)–(2.21).

$$\nabla_t \times \mathbf{E}_{t,0}^R = 0 \tag{2.14}$$

$$\nabla_t \times \mathbf{E}_{t,0}^I = 0 \tag{2.15}$$

$$-j\beta_0^R \hat{\mathbf{z}} \times \mathbf{E}_{t,0}^R + \nabla_t \times E_{z,0}^I \hat{\mathbf{z}} = -\mu^R \mathbf{H}_{t,0}^R \tag{2.16}$$

$$\beta_0^R \hat{\mathbf{z}} \times \mathbf{E}_{t,0}^I - j\beta_1^I \hat{\mathbf{z}} \times \mathbf{E}_{t,0}^R + \nabla_t \times E_{z,1}^R \hat{\mathbf{z}} = \mu^R \mathbf{H}_{t,0}^I + \mu^I \mathbf{H}_{t,0}^R \tag{2.17}$$

$$\nabla_t \times \mathbf{H}_{t,0}^R = 0 \tag{2.18}$$

$$\nabla_t \times \mathbf{H}_{t,0}^I = 0 \tag{2.19}$$

$$-j\beta_0^R \hat{\mathbf{z}} \times \mathbf{H}_{t,0}^R + \nabla_t \times H_{z,0}^I \hat{\mathbf{z}} = \mu^R \mathbf{E}_{t,0}^R \tag{2.20}$$

$$\beta_0^R \hat{\mathbf{z}} \times \mathbf{H}_{t,0}^I - j\beta_1^I \hat{\mathbf{z}} \times \mathbf{H}_{t,0}^R + \nabla_t \times H_{z,1}^R \hat{\mathbf{z}} = -\epsilon^R \mathbf{E}_{t,0}^I - \epsilon^I \mathbf{E}_{t,0}^R \tag{2.21}$$

For sufficiently low frequencies, it is permissible to add higher order terms in ω to (2.14)–(2.21). Under this assumption, (2.22)–(2.25) are approximately valid for a quasi-TEM mode $(\mathbf{E}^{\mathsf{QTEM}}, \mathbf{H}^{\mathsf{QTEM}}) = (\mathbf{E}_t^{\mathsf{QTEM}} + E_z^{\mathsf{QTEM}} \hat{\mathbf{z}}, \mathbf{H}_t^{\mathsf{QTEM}} + H_z^{\mathsf{QTEM}} \hat{\mathbf{z}})$ with propagation constant β^{QTEM} at low frequencies. Comparison with the exact equations (2.2)–(2.5) shows that the right hand side terms of (2.2) and (2.4) are missing in (2.22) and (2.24), respectively, implying that $(\mathbf{E}^{\mathsf{QTEM}}, \mathbf{H}^{\mathsf{QTEM}})$ is, in general*, only an exact solution to Maxwell's equations for $\omega = 0$.

$$\nabla_t \times \mathbf{E}_t^{\mathsf{QTEM}} = 0 \tag{2.22}$$

$$-j\beta^{\mathsf{QTEM}} \hat{\mathbf{z}} \times \mathbf{E}_t^{\mathsf{QTEM}} + \nabla_t \times E_z^{\mathsf{QTEM}} \hat{\mathbf{z}} = -j\omega\mu \mathbf{H}_t^{\mathsf{QTEM}} \tag{2.23}$$

$$\nabla_t \times \mathbf{H}_t^{\mathsf{QTEM}} = 0 \tag{2.24}$$

$$-j\beta^{\mathsf{QTEM}} \hat{\mathbf{z}} \times \mathbf{H}_t^{\mathsf{QTEM}} + \nabla_t \times H_z^{\mathsf{QTEM}} \hat{\mathbf{z}} = j\omega\epsilon \mathbf{E}_t^{\mathsf{QTEM}} \tag{2.25}$$

On a more positive note, equations (2.22)–(2.25) are easier to solve than (2.2)–(2.5), for *perfect* electric multiconductor waveguides. From (2.22) it follows that $\mathbf{E}_t^{\mathsf{QTEM}} = -\nabla_t \Phi$. Taking the divergence of (2.23) and using (2.22) shows that $\nabla_t \cdot (\mu \mathbf{H}_t^{\mathsf{QTEM}}) = 0$ and thus $\mu \mathbf{H}_t^{\mathsf{QTEM}} = \nabla_t \times \Psi \hat{\mathbf{z}}$. The divergence of (2.25) shows that the potential Φ is a solution of the modified Laplace equation (2.26), whereas (2.24) implies that the flux function Ψ is a solution of the modified Laplace equation (2.27).

$$\nabla_t \cdot (\epsilon \nabla_t \Phi) = 0 \tag{2.26}$$

$$\nabla_t \cdot \left(\frac{1}{\mu} \nabla_t \Psi \right) = 0 \tag{2.27}$$

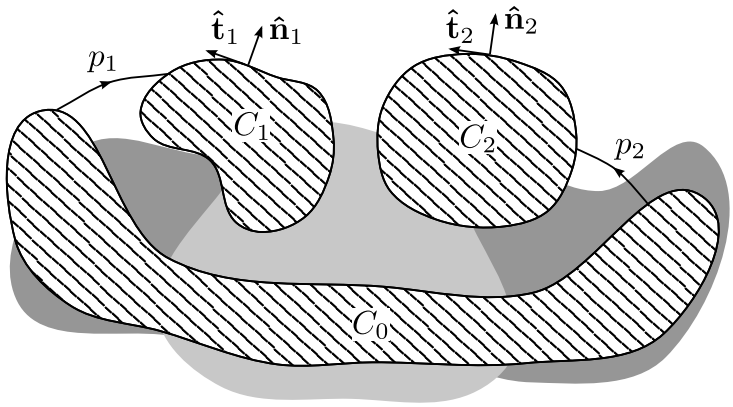

Figure 2.6: Multiconductor waveguide with one reference conductor C_0 and two signal conductors C_1 and C_2

Let us consider a perfect electric MCW, with N_c non-touching PECs $C_i \triangleq \Omega_{c(i)}$ (for $0 \leq i \leq N_c - 1$) with boundaries ∂C_i, exterior unit normal $\hat{\mathbf{n}}_i$ and tangential unit vector $\hat{\mathbf{t}}_i = \hat{\mathbf{z}} \times \hat{\mathbf{n}}_i$ (Fig. 2.6 shows an example with $N_c = 3$). Since the tangential component of the electric field and the normal component of the magnetic field vanish on ∂C_i, it follows that Φ and Ψ are constant on ∂C_i. Therefore, a* general solution of (2.26) and (2.27) is a linear combination of the $N \triangleq N_c - 1$ basis functions ϕ_i and ψ_i (for $1 \leq i \leq N$), as shown in (2.28)–(2.29), that satisfy (2.26) and (2.27), respectively, and are equal to 1 on ∂C_i and vanish on all ∂C_j with $i \neq j$.

$$\Phi = \sum_{i=1}^{N} V_i \phi_i \tag{2.28}$$

$$\Psi = \sum_{i=1}^{N} F_i \psi_i \tag{2.29}$$

The coefficient vectors $\bar{V} = \begin{pmatrix} V_1 & V_2 & \dots & V_N \end{pmatrix}^T$ and $\bar{F} = \begin{pmatrix} F_1 & F_2 & \dots & F_N \end{pmatrix}^T$, which represent the voltages on each *signal* conductor C_i (w.r.t. the *reference* conductor C_0) and fluxes of the magnetic induction through the paths p_i connecting the reference and signal conductors, respectively, are not independent. First, there is the relation (2.30) between the longitudinal current

*as mentioned earlier, there exist waveguides whose fundamental modes are TEM for all frequencies, which is also a sufficient condition for (2.22)–(2.25) to hold exactly

*note that we can choose $\Phi|_{\partial C_0} = \Psi|_{\partial C_0} = 0$, as the addition of a constant term to Φ or Ψ does not influence the fields; in essence, we are assigning the role of *reference* conductor to C_0

$I_i = \oint_{\partial C_i} \mathbf{H}_t^{\mathsf{QTEM}} \cdot \hat{\mathbf{t}}_i \, \mathrm{d}c$ through the signal conductor C_i and the fluxes.

$$I_i = j\omega \sum_{j=1}^{N} (\mathsf{Z}^{-1})_{ij} F_j \tag{2.30}$$

$$(\mathsf{Z}^{-1})_{ij} = -\frac{1}{j\omega} \oint_{\partial C_i} \frac{1}{\mu} \frac{\partial \psi_j}{\partial n_i} \mathrm{d}c \tag{2.31}$$

Integrating $\hat{\mathbf{z}}\times$(2.25) along the boundary ∂C_i leads to (2.32).

$$j\beta^{\mathsf{QTEM}} I_i = \sum_{j=1}^{N} (\mathsf{Y})_{ij} V_j \tag{2.32}$$

$$(\mathsf{Y})_{ij} = -j\omega \oint_{\partial C_i} \epsilon \frac{\partial \phi_j}{\partial n_i} \mathrm{d}c \tag{2.33}$$

Integrating $\hat{\mathbf{z}}\times$(2.23) along the path p_i leads, together with the fact that $E_z = 0$ on the PEC boundaries, to (2.34).

$$j\beta^{\mathsf{QTEM}} V_i = j\omega F_i \tag{2.34}$$

Combining (2.30)–(2.34) leads to (2.35)–(2.36), with $\bar{I} = \begin{pmatrix} I_1 & I_2 & \dots & I_N \end{pmatrix}^T$.

$$j\beta^{\mathsf{QTEM}} \bar{I} = \mathsf{Y}\bar{V} \tag{2.35}$$

$$j\beta^{\mathsf{QTEM}} \bar{V} = \mathsf{Z}\bar{I} \tag{2.36}$$

Combining (2.35)–(2.36) leads (2.37)–(2.38).

$$-\left(\beta^{\mathsf{QTEM}}\right)^2 \bar{I} = \mathsf{YZ}\bar{I} \tag{2.37}$$

$$-\left(\beta^{\mathsf{QTEM}}\right)^2 \bar{V} = \mathsf{ZY}\bar{V} \tag{2.38}$$

To each eigenvector $\bar{I}$ of YZ with eigenvalue $-\left(\beta^{\mathsf{QTEM}}\right)^2$ corresponds an eigenvector $\bar{V} = \frac{1}{j\beta^{\mathsf{QTEM}}} \mathsf{Z}\bar{I}$ of ZY with the same eigenvalue and a quasi-TEM eigenmode $(-\sum_{i=1}^{N} V_i \nabla_t \phi_i + E_z^{\mathsf{QTEM}} \hat{\mathbf{z}}, \mu^{-1} \sum_{i=1}^{N} F_i \nabla_t \psi_i \times \hat{\mathbf{z}} + H_z^{\mathsf{QTEM}} \hat{\mathbf{z}})$ with propagation constant β^{QTEM} that satisfies (2.22)–(2.25)*.

In conclusion, the $N = N_c - 1$ fundamental modes of a perfect electric MCW with N_c conductors at low frequencies are approximately equal to the quasi-TEM modes obtained via the solution of the modified Laplace equations (2.26)–(2.27) and an eigendecomposition of the N-dimensional matrix YZ.

*equations (2.23) and (2.25) are used as definitions for E_z^{QTEM} and H_z^{QTEM} [1]

2.4 Quasi-TM analysis

The quasi-TM analysis of the fundamental modes of an *imperfect* MCW in [4] is similar to the previous section, but now the term in the longitudinal electric field component E_z^{QTM} inside the imperfect conductors C_i ($0 \leq i \leq N_c - 1$), with conductivity σ_i and permittivity $\epsilon_i \approx -j\sigma_i/\omega$, cannot be neglected w.r.t. $\nabla_t \times \mathbf{H}_t^{\mathsf{QTM}}$ in (2.4). This leads, with the same approximations as for the quasi-TEM analysis, to system (2.39)–(2.43).

$$\nabla_t \times \mathbf{E}_t^{\mathsf{QTM}} = 0 \tag{2.39}$$

$$-j\beta^{\mathsf{QTM}}\hat{\mathbf{z}} \times \mathbf{E}_t^{\mathsf{QTM}} + \nabla_t \times E_z^{\mathsf{QTM}}\hat{\mathbf{z}} = -j\omega\mu\mathbf{H}_t^{\mathsf{QTM}} \tag{2.40}$$

$$\nabla_t \times \mathbf{H}_t^{\mathsf{QTM}} = 0 \qquad (\text{in } \mathbb{R}^2 \setminus \cup_i C_i) \tag{2.41}$$

$$\nabla_t \times \mathbf{H}_t^{\mathsf{QTM}} = \sigma_i E_z^{\mathsf{QTM}}\hat{\mathbf{z}} \qquad (\text{in } C_i) \tag{2.42}$$

$$-j\beta^{\mathsf{QTM}}\hat{\mathbf{z}} \times \mathbf{H}_t^{\mathsf{QTM}} + \nabla_t \times H_z^{\mathsf{QTM}}\hat{\mathbf{z}} = j\omega\epsilon\mathbf{E}_t^{\mathsf{QTM}} \tag{2.43}$$

Similar to the quasi-TEM analysis, (2.39) implies that $\mathbf{E}_t^{\mathsf{QTM}} = -\nabla_t\Phi$, whereas the divergence of (2.40) implies that $\mu\mathbf{H}_t^{\mathsf{QTM}} = \nabla_t \times \tilde{\Psi}\hat{\mathbf{z}}$. Taking the divergence of (2.43) and using (2.41) leads to (2.44), whereas (2.41)–(2.42) lead to (2.45)–(2.46).

$$\nabla_t \cdot (\epsilon\nabla_t\Phi) = 0 \qquad (\text{in } \mathbb{R}^2 \setminus \cup_i C_i) \tag{2.44}$$

$$\nabla_t \cdot \left(\frac{1}{\mu}\nabla_t\tilde{\Psi}\right) = 0 \qquad (\text{in } \mathbb{R}^2 \setminus \cup_i C_i) \tag{2.45}$$

$$\nabla_t \cdot \left(\frac{1}{\mu}\nabla_t\tilde{\Psi}\right) = -\sigma_i E_z^{\mathsf{QTM}} \qquad (\text{in } C_i) \tag{2.46}$$

In [4], it is argued that $\mathbf{E}_t \cdot \hat{\mathbf{t}}_i = 0$ on the conductor boundaries ∂C_i. This implies that Φ is constant on ∂C_i, and a* general solution of (2.44) is given by (2.47), with $N = N_c - 1$. Note that this also implies that the basis functions ϕ_i are the same as for the quasi-TEM analysis, i.e., for the case where the conductors in the MCW are assumed perfect.

$$\Phi = \sum_{i=1}^{N} V_i\phi_i \tag{2.47}$$

An important difference between the quasi-TEM and quasi-TM analyses is the fact that $\tilde{\Psi}$ is *not* constant on the conductor boundaries (as opposed to Ψ of section 2.3). For more details on the definition and numerical determination of Y and Z, called the *capacitance* and *inductance* problem, we refer to [4], [5].

*as in section 2.3, it is assumed that $\Phi|_{\partial C_0} = 0$, with C_0 the so-called reference conductor

2.5 Full-wave analysis

The need for a full-wave analysis of multiconductor waveguides, starting from Maxwell's equations (2.2)–(2.5), which will be elaborated in subsequent chapters, is apparent from the following considerations:

- The quasi-TEM and quasi-TM analyses are *only approximately valid at sufficiently low frequencies*, i.e., if no wave phenomena occur in the waveguide cross section or, otherwise stated, if the wavelength in the unbounded domain Ω_0 is sufficiently larger than the diameter $|\mathbb{R}^2 \setminus \Omega_0|$ of the core of the waveguide (see [1] for a proof for quasi-TEM).
- Only (approximations of) the *fundamental modes* of an MCW are provided by the quasi-TEM and quasi-TM analyses. Higher-order modes (i.e., modes that have a cut-off frequency higher than zero) or complex modes in closed waveguides are not predicted.

References

[1] F. Olyslager, *Electromagnetic Waveguides and Transmission Lines*. Oxford University Press, 1999, vol. 51, Oxford Engineering Science Series.

[2] J. Van Bladel, *Electromagnetic Fields*. John Wiley & Sons, 2007, IEEE Press Series on Electromagnetic Wave Theory.

[3] A. Bamberger and A. S. Bonnet, "Mathematical analysis of the guided modes of an optical fiber", *SIAM J. Math. Anal.*, vol. 21, no. 6, pp. 1487–1510, Sep. 1990.

[4] T. Demeester and D. De Zutter, "Quasi-TM transmission line parameters of coupled lossy lines based on the Dirichlet to Neumann boundary operator", *IEEE Transactions on Microwave Theory and Techniques*, vol. 56, no. 7, pp. 1649–1660, 2008.

[5] T. Demeester, "Transmission line modeling of lossy interconnects with the Dirichlet to Neumann boundary operator", PhD thesis, Ghent University, 2009.

3

Efficient Evaluation of 2.5-D BEM Interaction Integrals in Conductors

based on the contributions [1] and [2]

★ ★ ★

The solution of the time-harmonic Maxwell equations with a boundary element method, for 2-D geometries illuminated by arbitrary 3-D excitations, gives rise to numerical difficulties if highly conductive media are present. In particular, the interaction integrals arising in the method of moments involve kernels that strongly oscillate in space and, at the same time, decay exponentially. We present an accurate method to tackle these issues over a very broad conductivity range (from lossy dielectric to conductor skin-effect regime), for both magnetic and non-magnetic conductors. Important applications are the modal analysis of waveguides with non-perfect conductors, scattering problems and shielding problems with enclosures with arbitrary permeability and conductivity and 3-D noise sources.

3.1 Introduction

Boundary element methods (BEMs) provide a powerful framework to solve the time- and space-harmonic Maxwell equations (1.13)–(1.16) numerically. If the problem domain consists of homogeneous material regions, a BEM generally requires fewer unknowns than a volumetric discretization technique. This

chapter considers two-dimensional geometries with conductive material regions, which can be magnetic, illuminated by arbitrary three-dimensional sources, leading to a so-called 2.5-D boundary element method. Important applications of this class of problems are the eigenmode analysis of non-perfect multiconductor transmission lines (see chapters 2 and 4) [3]–[6], scattering problems [7] and shielding problems [1].

Interaction integrals appearing in the method of moments (MoM), with the scalar Green's function $G(\boldsymbol{\rho})$ and its normal derivatives as kernels, are numerically challenging due to two specific and interplaying aspects. First, the kernels in good conductors are strongly oscillating and exponentially decaying in space, due to the large magnitude and imaginary part of the conductor's wavenumber w.r.t. the free space wavenumber. Second, the kernels are singular, or nearly singular, in those regions of the integration domain where the test and basis functions' supports overlap or lie close to each other, respectively. This behavior requires special care for an accurate numerical evaluation. Moreover, the combination of the two aspects, i.e. interaction integrals with both (nearly) singular and oscillating as well as exponentially damped integrands, poses further difficulties. In this chapter we present an accurate method to handle both problems.

A large amount of literature is available concerning the numerical evaluation of MoM interaction integrals in low-loss dielectric media. Integrals with singular or nearly singular integrands are usually evaluated with a singularity extraction [8]–[10] or cancellation technique [11]–[13]. In 3-D, [14] uses singularity cancellation with RWG basis functions [15] to evaluate the interaction integrals in conductive media more accurately. A good overview of the additional problems that arise in conductive media can be found in [16], where, similarly as in this chapter, a so-called cutoff distance is introduced to limit the numerical integration domain of the interaction integrals in the three-dimensional case.

This chapter proposes a new method specifically tailored to the properties of the 2.5-D Green's function $G(\boldsymbol{\rho})$ in conductive media. It is shown, both theoretically and through corroborating examples, that the method accurately evaluates interaction integrals for a wide range of electrical conductivities (low-loss dielectric to highly conductive) and frequencies, and allows media with arbitrary permeability. In addition to the earlier mentioned fields of application, the new method is highly relevant to the accurate full-wave analysis of state-of-the-art multiconductor waveguides and enclosures.

The structure of this chapter is as follows: in sections 3.2 and 3.3 we briefly outline the employed integral equations and the interaction integrals appearing in the MoM. The problems encountered in evaluating the integrals in conductive media are elaborated in section 3.4, followed by our new method in section 3.5. Finally, the numerical examples in section 3.6 testify to the accuracy and applicability of the method, and clearly demonstrate the advantages over existing methods. Conclusions are formulated in section 3.7.

3.2 Geometry and Boundary Integral Equations

Consider a 2-D geometry consisting of isotropic homogeneous material regions Ω_i, with permittivity $\epsilon_i \in \mathbb{C}_0$, permeability $\mu_i \in \mathbb{C}_0$, and a single unbounded domain Ω_0* (Fig. 2.1). Assume that all sources and fields have a common time and longitudinal dependence $e^{j(\omega t - \beta z)}$ ($\beta \in \mathbb{C}$), i.e., the time- and space harmonic Maxwell equations (1.13)–(1.16) hold for the phasor fields. A general three-dimensional excitation can be expanded into sources of this kind via Fourier transformation in the z direction. The unknowns of the problem are the phasors of the time- and space harmonic tangential electric and magnetic boundary fields, given by $\hat{\mathbf{n}}\times\mathbf{E}\times\hat{\mathbf{n}} = E_t\hat{\mathbf{t}}+E_z\hat{\mathbf{z}}$ and $\hat{\mathbf{n}}\times\mathbf{H}\times\hat{\mathbf{n}} = H_t\hat{\mathbf{t}}+H_z\hat{\mathbf{z}}$, with E_t and H_t the transverse tangential components, E_z and H_z the longitudinal components, $\hat{\mathbf{n}}$ the outward unit normal to Ω_i and $\hat{\mathbf{t}} = \hat{\mathbf{z}}\times\hat{\mathbf{n}}$. The representation formulas (1.34)–(1.37) hold, with $E_t^{(i)}\hat{\mathbf{t}} + E_z^{(i)}\hat{\mathbf{z}}$ the incoming tangential electric field generated by sources in Ω_i, $\tilde{\Gamma}$ the boundary of Ω_i, $\boldsymbol{\rho} = x\hat{\mathbf{x}} + y\hat{\mathbf{y}}$, $\epsilon = \epsilon_i$, $\mu = \mu_i$ and $\gamma = \sqrt{\omega^2\epsilon_i\mu_i - \beta^2}$.

A system of coupled integral equations is obtained after imposing continuity of the tangential fields at the boundaries, yielding a 2.5-D version of the PMCHWT (Poggio-Miller-Chang-Harrington-Wu-Tsai) operator [17]–[19]. A finite-dimensional linear system is obtained with the MoM, as explained in the next section.

3.3 MoM Interaction Integrals

Before presenting our new theory from section 3.4 onwards, we briefly recall which types of interaction integrals occur in the MoM of the 2.5-D PMCHWT boundary integral equation [20], [21]. The boundaries are meshed into a union of segments S_j with length l_j, separated by nodes $\boldsymbol{\rho}_k$ (Fig. 3.1). The transverse tangential components E_t and H_t are expanded in terms of pulse functions $p_j(\boldsymbol{\rho})$, with support over segment S_j, whereas the longitudinal components E_z and H_z are expanded into triangular functions $t_k(\boldsymbol{\rho})$, with support over segments that share a node $\boldsymbol{\rho}_k$ [20], [21]:

$$\begin{array}{ll} p_j(\boldsymbol{\rho}) = 1 & \boldsymbol{\rho} \in S_j, \\ t_k(\boldsymbol{\rho}) = 1 - |\boldsymbol{\rho} - \boldsymbol{\rho}_k|\ l_j^{-1} & \boldsymbol{\rho}, \boldsymbol{\rho}_k \in S_j. \end{array} \tag{3.1}$$

The continuity equations for E_z and H_z are tested with pulse functions, whereas the equations for E_t and H_t are tested with triangular functions. To calculate the elements in the MoM system matrix, the interaction integrals (3.2)–(3.4) below need to be evaluated numerically for basis and test functions with support over segments that have Ω_i as a neighboring medium. This can be easily seen by inspecting (1.34) and (1.35). The tangential derivatives of the Green's function

*note that this geometry corresponds to the definition in section 2.1 of a *waveguide* without perfect electric and magnetic conductors

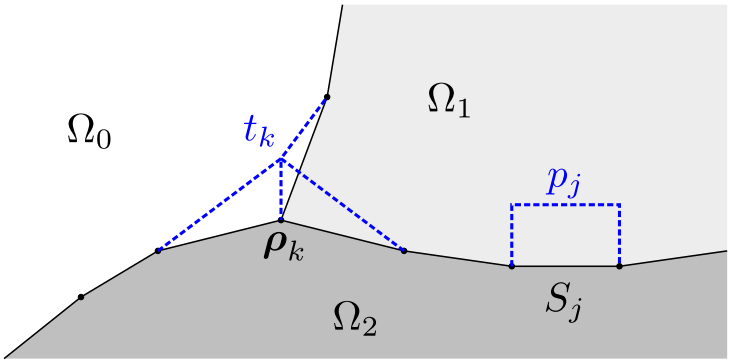

Figure 3.1: The boundaries are approximated with straight segments along which triangular and pulse functions are defined.

can be transferred to the test function using integration by parts such that only three types of interaction integrals remain:

$$\mathsf{I}_{jk}^{(1)} = \int_{\tilde{\Gamma}} p_j(\boldsymbol{\rho})\mathrm{d}c \int_{\tilde{\Gamma}} G(\boldsymbol{\rho}-\boldsymbol{\rho}')\; p_k(\boldsymbol{\rho}')\mathrm{d}c', \tag{3.2}$$

$$\mathsf{I}_{jk}^{(2)} = \int_{\tilde{\Gamma}} p_j(\boldsymbol{\rho})\mathrm{d}c \int_{\tilde{\Gamma}} \frac{\partial G(\boldsymbol{\rho}-\boldsymbol{\rho}')}{\partial n'} t_k(\boldsymbol{\rho}')\mathrm{d}c', \tag{3.3}$$

$$\mathsf{I}_{jk}^{(3)} = \int_{\tilde{\Gamma}} t_j(\boldsymbol{\rho})\mathrm{d}c \int_{\tilde{\Gamma}} \frac{\partial^2 G(\boldsymbol{\rho}-\boldsymbol{\rho}')}{\partial n \partial n'} t_k(\boldsymbol{\rho}')\mathrm{d}c'. \tag{3.4}$$

3.4 Difficulties in Conductive Media

Consider a conductive region Ω, with conductivity σ, complex permittivity $\epsilon = \epsilon_0 - j\frac{\sigma}{\omega}$ and permeability μ. The transversal wavenumber γ can be written as a function of the skin depth $\delta = \sqrt{2/(\omega\mu\sigma)}$ for moderate to high conductivity values, as follows:

$$\gamma = \sqrt{\omega^2\mu(\epsilon_0 - j\sigma/\omega) - \beta^2} \tag{3.5}$$

$$\underset{\sigma \gg \omega\epsilon_0}{\approx} \frac{1-j}{\delta}. \tag{3.6}$$

The particular form of this wavenumber is responsible for the difficulties that arise in evaluating the interaction integrals (3.2)–(3.4) in a highly conductive medium. The Green's function in the conductor reduces to $-\frac{j}{4}H_0^{(2)}\left((1-j)r/\delta\right)$, with $r = |\boldsymbol{\rho}-\boldsymbol{\rho}'|$, while its normal derivatives are expressible in terms of the zeroth, first and second order Hankel functions of the second kind (see appendix 3.8). For large $|\gamma r|$, the Hankel function of the second kind and order ν behaves

as [22]

$$H_\nu^{(2)}(\gamma r) \sim \left(\frac{2}{\pi\gamma r}\right)^{\frac{1}{2}} e^{-j\gamma r + j\frac{\pi}{4}(2\nu+1)} \qquad (|\arg \gamma r| < \pi). \tag{3.7}$$

In a highly conductive medium, the large imaginary part of the wavenumber causes a strong exponential decay of the Green's function and its derivatives. Moreover, the wavelength $\lambda = 2\pi\delta$ is small w.r.t. the free space wavelength, which leads to a spatially strong oscillation of the Green's function and its derivatives. If S_j is a segment on the interface between the conductive region Ω and a dielectric region Ω_d, it is sufficient to choose the segment length to be a fraction of the wavelength λ_d in the dielectric, say $l_j = \frac{\lambda_d}{10} = \frac{2\pi}{10\omega\sqrt{\epsilon_d\mu_d}}$, in order to capture the varying field behavior at the interface. This is because the tangential fields at the interface can only vary at a pace on the order of λ_d in the dielectric and remain continuous at the interface (there are no surface currents). Typically $\delta \ll l_j$ and accordingly a lot of oscillations occur along one segment and standard quadrature techniques fail to correctly evaluate the interaction integrals in the conductive region. Choosing $l_j = \frac{\lambda}{10}$ (with λ corresponding to the wavelength in the conductor) to try to tackle this problem is unnecessary to capture the field behavior and would lead to a very large increase of the number of unknowns.

3.5 Efficient Evaluation of Interaction Integrals

This section proposes a new method to accurately evaluate the MoM interaction integrals in conductive media, with a relatively low quadrature order. The method reduces to the traditional approach in [21] for $\sigma \ll \omega\epsilon_0$ (low-loss dielectric case), and is therefore applicable to arbitrary conductivities $\sigma \in [0, \infty[$, as shown in this section and corroborated by the numerical examples in section 3.6.

3.5.1 Cutoff Distance

The key to accurately integrate the strongly oscillating and exponentially decaying integrands in conductive media, for a fixed number of quadrature points, is to distribute those points over the integration domain where the Green's function has a non-negligible value. Because the magnitude of the Green's function decays exponentially in a good conductor, it can be approximated as $-\frac{j}{4}H_0^{(2)}(\gamma r)\mathbb{H}(r_{\mathsf{cut}} - r)$, neglecting its tail, with $\mathbb{H}$ the Heaviside step function and r_{cut} the cutoff distance.

The cutoff distance is the distance above which the asymptotic Green's function (using (3.7)) becomes smaller in magnitude than a threshold Δ_{cut}. It can be written in terms of the principal branch of the Lambert W function [23], denoted $\mathcal{W}(z)$.

Definition 1 (Cutoff distance r_{cut})**.**

$$r_{\mathsf{cut}} = -\frac{1}{2\Im\gamma}\mathcal{W}\left(\frac{-4\Im\gamma}{\pi\Delta_{\mathsf{cut}}^2|\gamma|}\right) \underset{\sigma\gg\omega\epsilon_0}{\approx} \frac{\delta}{2}\mathcal{W}\left(\frac{2\sqrt{2}}{\pi\Delta_{\mathsf{cut}}^2}\right) \tag{3.8}$$

An upper bound on the Green's function itself is given in Theorem 3.5.1. For sufficiently small Δ_{cut}, the asymptotic expansion (3.7) is a good approximation and $C \approx 1$.

Theorem 3.5.1. *For $|\boldsymbol{\rho}| \geq r_{\mathsf{cut}}$ it holds that $|G(\boldsymbol{\rho})| \leq C\Delta_{\mathsf{cut}} e^{(|\boldsymbol{\rho}|-r_{\mathsf{cut}})\Im\gamma}$ with $C = 1 + \frac{1}{8|\gamma|r_{\mathsf{cut}}}$.*

Proof. Note that $H_0^{(2)}(z) = \sqrt{\frac{2}{\pi z}}e^{-j\left(z-\frac{\pi}{4}\right)}\left(1-\frac{\theta_2(z)}{8jz}\right)$, with $|\theta_2(z)| < 1$ if $\Im z < 0$ [24]. For $r \geq r_{\mathsf{cut}}$, this leads to

$$\left|\frac{j}{4}H_0^{(2)}(\gamma|\boldsymbol{\rho}|)\right| \leq \frac{1}{4}\sqrt{\frac{2}{\pi|\gamma|r_{\mathsf{cut}}}}e^{r_{\mathsf{cut}}\Im\gamma}e^{(|\boldsymbol{\rho}|-r_{\mathsf{cut}})\Im\gamma}\left(1+\frac{1}{8|\gamma|r_{\mathsf{cut}}}\right) \tag{3.9}$$

$$= C\Delta_{\mathsf{cut}}e^{(|\boldsymbol{\rho}|-r_{\mathsf{cut}})\Im\gamma}, \tag{3.10}$$

where the last step follows from Definition 1. □

To illustrate the use of the cutoff distance in the calculation of the interaction integrals, consider $\mathsf{I}_{jk}^{(1)}$ in a conductive medium:

$$\mathsf{I}_{jk}^{(1)} \approx \int_{S_j} p_j(\boldsymbol{\rho})\mathrm{d}c \int_{S_k} G(\boldsymbol{\rho}-\boldsymbol{\rho}')\mathbb{H}(r_{\mathsf{cut}}-|\boldsymbol{\rho}-\boldsymbol{\rho}'|)p_k(\boldsymbol{\rho}')\mathrm{d}c'. \tag{3.11}$$

The boundaries of the test integral over test segment S_j follow from the intersection of S_j with the set of points that are closer than the cutoff distance from the source segment S_k (region Υ_k in Fig. 3.2). Because Υ_k is convex, either $S_j \cap \Upsilon_k = \varnothing$ (no interaction) or $S_j \cap \Upsilon_k$ is a subsegment (AB in Fig. 3.2). For each test point $\boldsymbol{\rho} \in (S_j \cap \Upsilon_k)$, the basis integration interval is a subsegment of S_k (CD in Fig. 3.3).

In this way, interactions between points that are separated further than r_{cut} are neglected and the quadrature points are distributed over the region where the integrand is non-negligible, which alleviates the problem of the exponential damping of the integrand. At the same time, the number of oscillations of the integrands in the interaction integrals is small, *independent of the conductivity*, allowing a relatively low quadrature order. To show this, consider an interface between free space (wavelength λ_0) and a conductive region (conductivity σ, wavenumber $\gamma = \sqrt{\omega^2\mu_0(\epsilon_0 - j\sigma/\omega) - \beta^2}$), with boundary segment length equal to $l = \lambda_0/10$. The integrands of the interaction integrals (3.2)–(3.4) can be expressed in terms of Hankel functions of the second kind, as shown in (3.13).

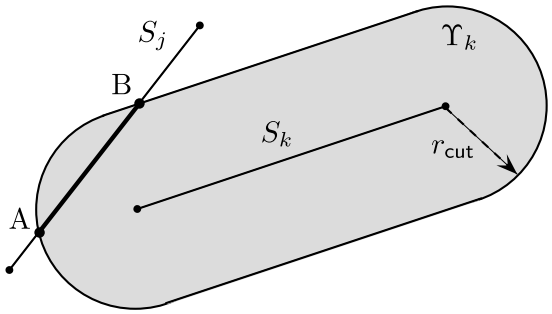

Figure 3.2: Test integration interval AB, where the interactions from segment S_k are non-negligible.

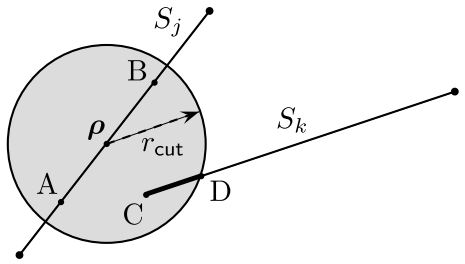

Figure 3.3: Basis integration interval CD, for test point $\boldsymbol{\rho}$.

For $\sigma \gg \omega\epsilon_0$, it is evident from (3.8) that $r_{\mathsf{cut}} \sim \delta$, implying that the number of oscillations of $H_\eta^{(2)}(\gamma r)$ in $r \in [0, r_{\mathsf{cut}}]$ is bounded for high conductivities. For $\sigma \ll \omega\epsilon_0$, $r_{\mathsf{cut}} > l$ and the number of oscillations of $H_\eta^{(2)}(\gamma r)$ for $r \in [0, l]$ in a dielectric region is also bounded. A measure for the maximum number of oscillations of the integrands is given by

$$Z = \max_{\substack{\sigma\in[0,\infty[\\ \beta\in[0,\omega\sqrt{\epsilon_0\mu_0}] \\ \eta\in\{0,1,2\} \\ \mathcal{P}\in\{\Re,\Im\}}} z(\mathcal{P}H_\eta^{(2)}(\gamma r), [0, \min(r_{\mathsf{cut}}, l)]), \tag{3.12}$$

where $z(f(r), \mathcal{A})$ denotes the number of zero-crossings of $f(r)$ in $r \in \mathcal{A}$. It can be easily verified that $Z = 2$, 4 and 6 if $\Delta_{\mathsf{cut}} = 10^{-3}$, 10^{-6} and 10^{-9}, respectively, which shows that the number of oscillations increases if a higher accuracy is required (larger r_{cut}), but remains small, allowing a low quadrature order, independent of σ. In conclusion, the cutoff distance alleviates both problems of exponentially damped and highly oscillatory kernels in conductive media. This approach is an extension of the traditional method in [21], to accurately evaluate the interaction integrals in media with arbitrary conductivity.

3.5.2 Singularity Extraction

The three types of interaction integrals (3.2)–(3.4) can be written as

$$\mathsf{I}_{jk}^{(l)} = \int_{\tilde{\Gamma}} w_j^{(l)}(\boldsymbol{\rho}) \int_{\tilde{\Gamma}} b_k^{(l)}(\boldsymbol{\rho}')\mathbb{H}(r_{\mathsf{cut}} - r) \sum_{\eta=0}^{2} f_\eta^{(l)}(\boldsymbol{\rho}, \boldsymbol{\rho}') H_\eta^{(2)}(\gamma r) \mathrm{d}c' \; \mathrm{d}c, \tag{3.13}$$

with $r = |\boldsymbol{\rho} - \boldsymbol{\rho}'|$. The test and basis functions are given by

$$w_j^{(1)}(\boldsymbol{\rho}) = w_j^{(2)}(\boldsymbol{\rho}) = p_j(\boldsymbol{\rho}), \tag{3.14}$$
$$w_j^{(3)}(\boldsymbol{\rho}) = t_j(\boldsymbol{\rho}), \tag{3.15}$$
$$b_k^{(1)}(\boldsymbol{\rho}') = p_k(\boldsymbol{\rho}'), \tag{3.16}$$
$$b_k^{(2)}(\boldsymbol{\rho}') = b_k^{(3)}(\boldsymbol{\rho}') = t_k(\boldsymbol{\rho}'). \tag{3.17}$$

As shown in appendix 3.8, the functions $f_\eta^{(l)}(\boldsymbol{\rho}, \boldsymbol{\rho}')$ that are not identically zero are given by

$$f_0^{(1)} = -\frac{j}{4}, \tag{3.18}$$
$$f_1^{(2)} = -\frac{j\gamma}{4}(\hat{\mathbf{n}}' \cdot \hat{\mathbf{r}}), \tag{3.19}$$
$$f_0^{(3)} = -\frac{j\gamma^2}{8}(\hat{\mathbf{n}} \cdot \hat{\mathbf{n}}'), \tag{3.20}$$
$$f_2^{(3)} = \frac{j\gamma^2}{8}\left(2(\hat{\mathbf{n}} \cdot \hat{\mathbf{r}})(\hat{\mathbf{n}}' \cdot \hat{\mathbf{r}}) - \hat{\mathbf{n}} \cdot \hat{\mathbf{n}}'\right). \tag{3.21}$$

If the test and basis functions' supports overlap or lie next to each other, the integrands in (3.13) have a singularity in the integration domain. We employ a singularity extraction technique with an extracted singular part that is also limited by the cutoff distance, given by

$$\mathsf{I}_{jk,\mathsf{sing}}^{(l)} = \int_{\tilde{\Gamma}} w_j^{(l)}(\boldsymbol{\rho}) \int_{\tilde{\Gamma}} b_k^{(l)}(\boldsymbol{\rho}')\mathbb{H}(r_{\mathsf{cut}} - r) \sum_{\eta=0}^{2} f_\eta^{(l)}(\boldsymbol{\rho}, \boldsymbol{\rho}') \mathcal{S}_\eta(\gamma r) \mathrm{d}c' \; \mathrm{d}c. \tag{3.22}$$

The functions $\mathcal{S}_\eta$ are given by

$$\mathcal{S}_0(\gamma r) = \frac{2j}{\pi} \log r, \tag{3.23}$$
$$\mathcal{S}_1(\gamma r) = -\frac{2j}{\pi\gamma r}, \tag{3.24}$$
$$\mathcal{S}_2(\gamma r) = -\frac{4j}{\pi\gamma^2 r^2}. \tag{3.25}$$

The integrals of the limited singular parts are known in closed-form. For example, the self-patch term of the first type is given by

$$\mathsf{I}^{(1)}_{jj,\mathsf{sing}} = \frac{j}{\pi} a((4l_j - 2a)\log a - 4l_j + a), \tag{3.26}$$

with $a = \min(r_{\mathsf{cut}}, l_j)$.

3.6 Numerical Results

Plane wave scattering at a conductive cylinder is used to validate the accuracy of the proposed method as a function of the accuracy parameter Δ_{cut}, for a wide range of electrical conductivities in the general case of oblique incidence ($\beta \neq 0$), and to compare it with existing methods. The next examples are practically relevant shielding problems, in which a conductive and (non-)magnetic enclosure with apertures is used to shield the interior from the fields generated by an exterior electric current source. The new method is able to accurately calculate the shielding performance over a broad frequency range, and outperforms existing methods in terms of accuracy and simulation time.

3.6.1 Scattering at a Conductive Cylinder

To validate the accuracy of the proposed 2.5-D BEM for conductive media and compare it with existing numerical methods, we consider the problem of plane wave scattering at a conductive cylinder (diameter d, finite conductivity σ and permittivity $\epsilon_0 - j\sigma/\omega$), embedded in free space (Fig. 3.4). An analytical expression of the solution can be obtained via separation of variables [25]. The accuracy of the proposed method is compared with the traditional method without cutoff distance, and with a surface impedance approximation, over a wide conductivity range, from the low-loss dielectric ($\omega\epsilon_0 \gg \sigma$) to the conductive region ($\omega\epsilon_0 \ll \sigma$).

The numerically obtained radar cross section (RCS), denoted $S_n(\phi)$, is compared with the analytical solution, denoted $S_a(\phi)$. The relative error between these cross sections is defined by

$$\mathcal{E} = \sqrt{\frac{\sum_{k=1}^{K} |S_n(\phi_k) - S_a(\phi_k)|^2}{\sum_{k=1}^{K} |S_a(\phi_k)|^2}}, \tag{3.27}$$

with $\phi_k = 2\pi k/K$ and $K = 100$. Figures 3.5-3.6 show the relative error as a function of the skin depth for the two polarizations (VV and VH) of oblique plane wave incidence ($\alpha = 45°$). The skin depth $\delta = \sqrt{2/(\omega\mu_0\sigma)}$ ranges from 10^{-5} m to 10 m, covering the region between a good conductor with conductivity $\sigma = 10^7$ S/m and a low-loss dielectric with relative dielectric constant $1 - 5 \cdot 10^{-4} j$. Observe that, in general, the error decreases if the

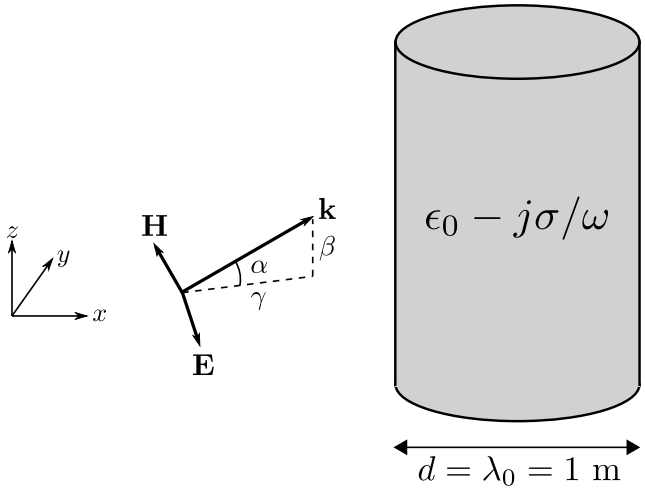

Figure 3.4: Plane wave scattering at a conductive cylinder with conductivity σ, permittivity $\epsilon_0 - j\sigma/\omega$ and diameter $d = 1$ m. The cylinder is illuminated by a linearly polarized plane wave, with free space wavelength $\lambda_0 = 1$ m, impinging at an angle α w.r.t. the (x, y) plane.

accuracy threshold Δ_{cut} becomes smaller. The relative error saturates around five significant digits for small and large skin depths, but this lower bound is determined mostly by the boundary meshing of the circular cross section into straight segments. The asymptotic value for the cutoff distance in (3.8), in case of high conductivity, is shown in the legend. For $r_{\mathsf{cut}} > d$, no interactions are neglected, and the numerical solution becomes independent of Δ_{cut}, as can be seen for high δ/d values.

The inability of the traditional method without cutoff distance (i.e. the proposed method with $r_{\mathsf{cut}} = \infty$) to accurately evaluate the interaction integrals in conductive media, for a fixed quadrature order and constant number of boundary segments, is clearly demonstrated in Fig. 3.6. The problems mentioned in section 3.4, i.e. the exponential decay combined with strong oscillation of the integrands, render the traditional method inaccurate or useless for low values of δ/d. The proposed method focuses the quadrature points in the region where the integrands are non-negligible, by introducing the cutoff distance (3.8) and a singularity extraction with limited extracted part, which in turn limits the number of oscillations. This leads to a near constant accuracy over the considered conductivity range (if enough oscillations are taken into account, i.e. for sufficiently low Δ_{cut}). For $r_{\mathsf{cut}} > d$, or equivalently for high δ/d values, our new method reduces to the traditional one, and the numerical solution is the same for both methods.

Another approach to incorporate good conductors in a BEM is the use of a

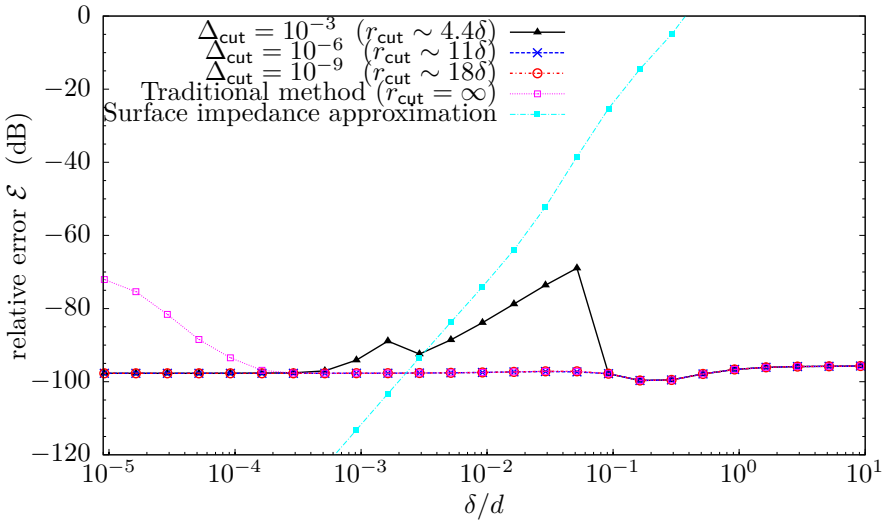

Figure 3.5: Relative error of the co-polarization RCS (VV) as a function of the skin depth δ for oblique incidence ($\alpha = 45°$) for the proposed method, the traditional method without cutoff distance and limited extracted part, and a surface impedance approximation. The quadrature order of the interaction integrals ($Q = 32$) and number of boundary segments ($N = 630$) are constant.

surface impedance approximation, by imposing the condition $\mathbf{E} \times \hat{\mathbf{n}} = Z_s(\hat{\mathbf{n}} \times \mathbf{H} \times \hat{\mathbf{n}})$ on the conductor boundary, with $Z_s = (1+j)\sqrt{\frac{\omega\mu_0}{2\sigma}}$ and $\hat{\mathbf{n}}$ the outward normal to the conductive region. Figures 3.5-3.6 show that this is a good approximation for low values of δ/d, i.e. in the conductor skin-effect regime (note that the error does not saturate around 100 dB because the analytical solution with surface impedance approximation is considered). It is apparent from Fig. 3.6 that the proposed method (with $\Delta_{\mathsf{cut}} = 10^{-9}$) outperforms the surface impedance approximation and traditional method in terms of accuracy, in the transition region between low-loss dielectric and skin-effect regime.

3.6.2 Slotted Coaxial Shield

In this example, we investigate the shielding performance of a coaxial enclosure with one or two slots at angles α_1 and α_2 (Fig. 3.7). The coaxial enclosure is illuminated by an electric line current $I_0\delta(\boldsymbol{\rho} - \boldsymbol{\rho}_0)\hat{\mathbf{z}}$ (hence $\beta = 0$), which induces an unwanted noise current I_1 in the enclosed copper signal conductor. Remark that, in addition to our MoM integral equation technique, scattering at a concentrically loaded cylindrical shield with $n-1$ apertures can be solved by reducing an n-series problem to an equivalent Riemann-Hilbert problem [26], [27]. A similar radial mode matching technique has been employed for multi-slotted shields with finite thickness [28]. We consider three enclosure

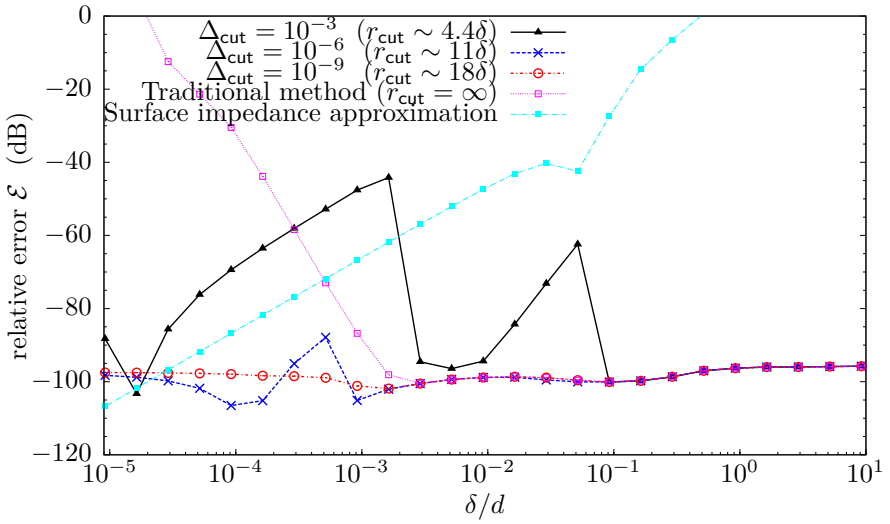

Figure 3.6: Relative error of the cross-polarization RCS (VH) as a function of the skin depth δ for oblique incidence ($\alpha = 45°$) for the proposed method, the traditional method without cutoff distance and limited extracted part, and a surface impedance approximation. The quadrature order of the interaction integrals ($Q = 32$) and number of boundary segments ($N = 630$) are constant.

materials: copper ($\sigma = 5.8 \cdot 10^7$ S/m, $\mu_r = 1$), a magnetic conductor with the same skin depth ($\sigma = 5.8 \cdot 10^4$ S/m, $\mu_r = 1000$), and a perfect electric conductor ($\sigma = \infty$). The configurations with one and two slots are described by $\alpha_1 = 90°$ and $(\alpha_1, \alpha_2) = (60°, 120°)$, respectively.

Figure 3.8 shows the relative noise current amplitude $|I_1/I_0|$ of the copper and perfect electric conducting (PEC) enclosure, over a broad frequency range (from 100 Hz to 1 GHz). Observe that the analytical solution for the closed coaxial enclosure (no slots) coincides with the numerical solution. At low frequencies, there is leakage through the copper enclosure, as the skin depth is comparable to the thickness, and the presence of slots does not deteriorate the shielding performance significantly. At high frequencies, the predominant leakage mechanism is diffraction of the fields at the slots, and the copper and PEC shields exhibit the same behavior. For the given position of the slots and line current, the noise current for two slots is about 15 dB higher than for one slot.

Figure 3.9 shows the relative noise current amplitude for the magnetic conducting enclosure. For the configuration without slots, the numerical and analytical solution coincide. Compared to the copper enclosure, at low frequencies, the presence of slots now has a larger influence. This is due to a different shielding mechanism in the magnetic conductor, adding to the effect of the conductivity.

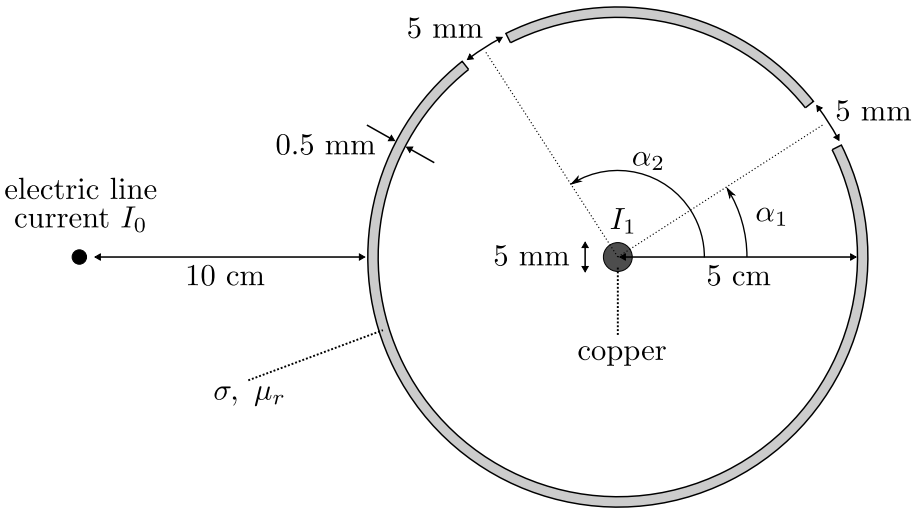

Figure 3.7: Cross section of a coaxial enclosure with conductivity σ and relative permeability μ_r, illuminated by an electric line current I_0, and enclosing a copper signal conductor with induced noise current I_1. There are one or two slots present at angles α_1 and α_2.

If $\mu_r > 1$, the magnetic induction produced by the source is diverted into the enclosure, then shunted within the material in a direction nearly parallel to its surface, and finally released back into free space [29]. The presence of slots disturbs the flux shunting, and negatively affects the shielding performance.

It is interesting to compare our new method with the traditional method ($r_{\mathsf{cut}} = \infty$) in terms of accuracy and simulation time. Fig. 3.10 shows the calculated shielding performance as a function of the quadrature order Q, for the copper shield with two slots. For $\Delta_{\mathsf{cut}} = 10^{-9}$, the new method already converges to the solution for $Q = 10$, compared to $Q = 80$ for the traditional method. For the same quadrature order $Q = 10$, the traditional method fails to accurately predict the shielding performance, due to the problems mentioned in section 3.4. Evidently, the need for a smaller quadrature order to obtain the same accuracy leads to a decrease in simulation time (Table 3.1). Even for the same quadrature order ($Q = 10$), our method is faster than the traditional method because interactions between segments separated by at least the cutoff distance are not taken into account.

3.6.3 Cable Tray Shield

The geometry of a metal cable tray with polygonal cross section (Fig. 3.11) is similar to the previous example, but arguably more interesting from a practical perspective. In this case, no closed-form analytical solution is available for

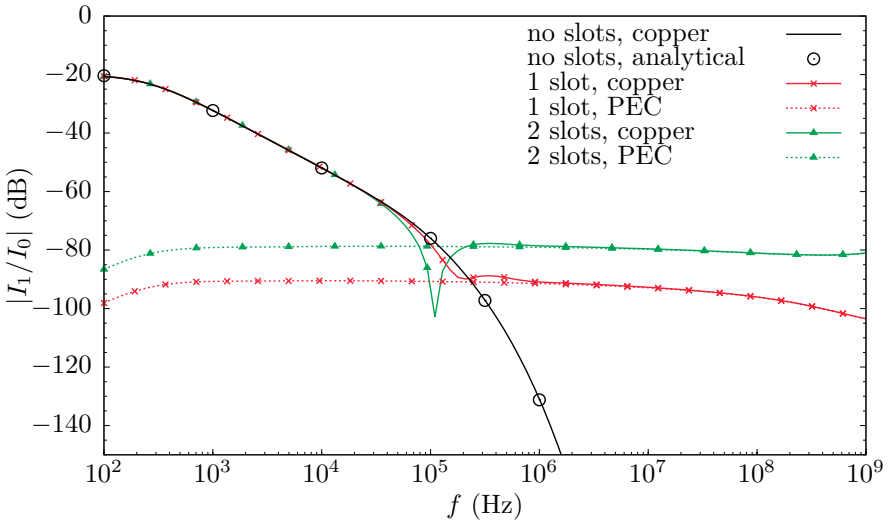

Figure 3.8: Shielding performance of the coaxial enclosure as a function of frequency, for a copper and perfect electric conducting (PEC) enclosure, with a varying number of slots.

Table 3.1: Simulation time of the new method (top) and the traditional method (bottom), versus the quadrature order Q (see Fig. 3.10).

Q	Time (s)
10	10
10	17
20	45
40	150
80	575

the closed cable tray ($g = 0$). The enclosure is illuminated by an electric line current $I_0\delta(\boldsymbol{\rho} - \boldsymbol{\rho}_0)\hat{\mathbf{z}}$ (hence $\beta = 0$), which induces unwanted noise currents I_i in the three copper signal conductors. Figure 3.12 shows the relative current magnitude $|I_2/I_0|$ in the middle conductor, for an open and closed cable tray (aperture length $g = 5.5$ mm and $g = 0$, respectively). We consider three enclosure materials: copper ($\sigma = 5.8 \cdot 10^7$ S/m, $\mu_r = 1$), a magnetic conductor with the same skin depth ($\sigma = 5.8 \cdot 10^4$ S/m, $\mu_r = 1000$), and a perfect electric conductor ($\sigma = \infty$).

At low frequencies (up to 10^5 Hz), we notice that the influence of the apertures can be neglected, as the open and closed cable tray yield approximately the same shielding performance, for both copper and the magnetic conductor. In this region, the skin depth is comparable to the thickness, allowing the

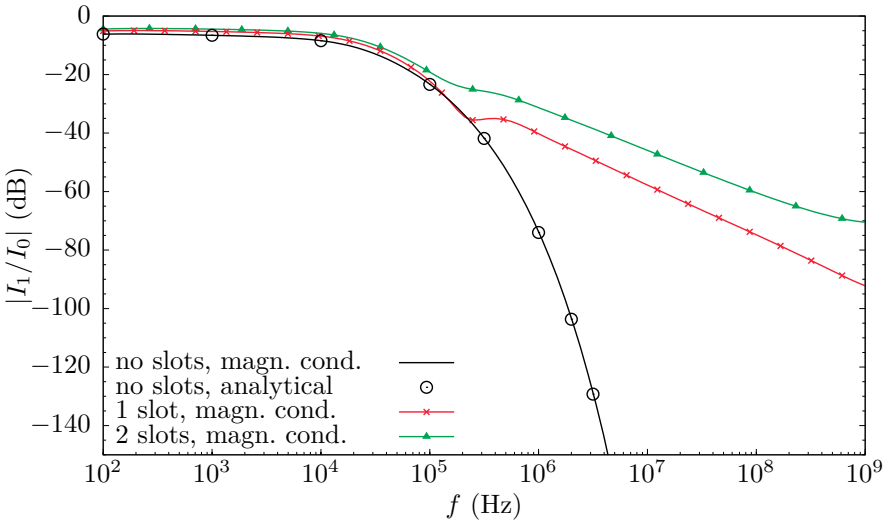

Figure 3.9: Shielding performance of the coaxial enclosure as a function of frequency, for the magnetic conductor, with a varying number of slots.

fields to penetrate the enclosure. At high frequencies, the copper and perfectly conducting open cable tray behave in the same way, indicating that diffraction of the fields through the aperture is the predominant leakage mechanism. Observe that the magnetic conductor exhibits a worse shielding performance than copper, for all considered frequencies.

3.7 Conclusions

This chapter presents a novel method to accurately and efficiently calculate 2.5-D MoM interactions integrals in conductive media, with arbitrary permeability. The resulting BEM is practically relevant to a large number of application domains, including full-wave modal analysis of non-perfect multiconductor waveguides (see chapter 4), scattering problems, and shielding problems with general three-dimensional sources.

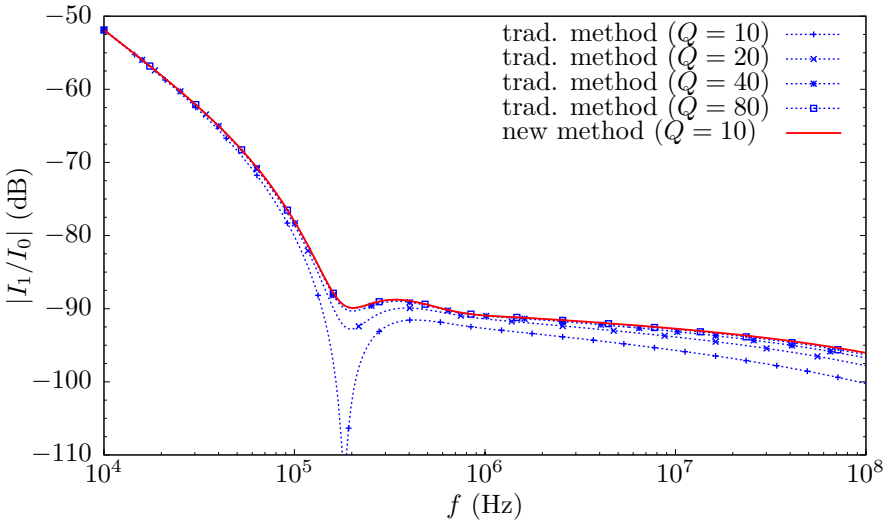

Figure 3.10: Comparison between the traditional method (with $r_{\mathsf{cut}} = \infty$) and the new method in this chapter (with $\Delta_{\mathsf{cut}} = 10^{-9}$), of the calculated shielding performance of the copper coaxial enclosure with two slots, for a varying quadrature order Q.

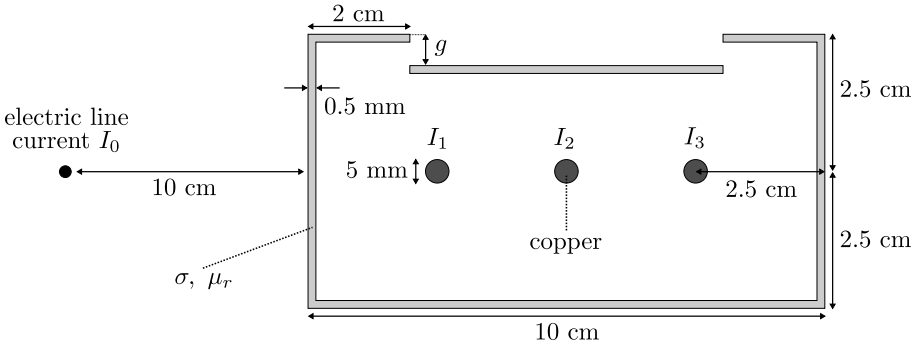

Figure 3.11: Cross section of an open cable tray with conductivity σ and relative permeability μ_r, illuminated by an electric line current I_0, and enclosing three copper signal conductors with induced noise currents I_1 to I_3. The geometry is symmetrical w.r.t. a vertical line through the center of the middle conductor.

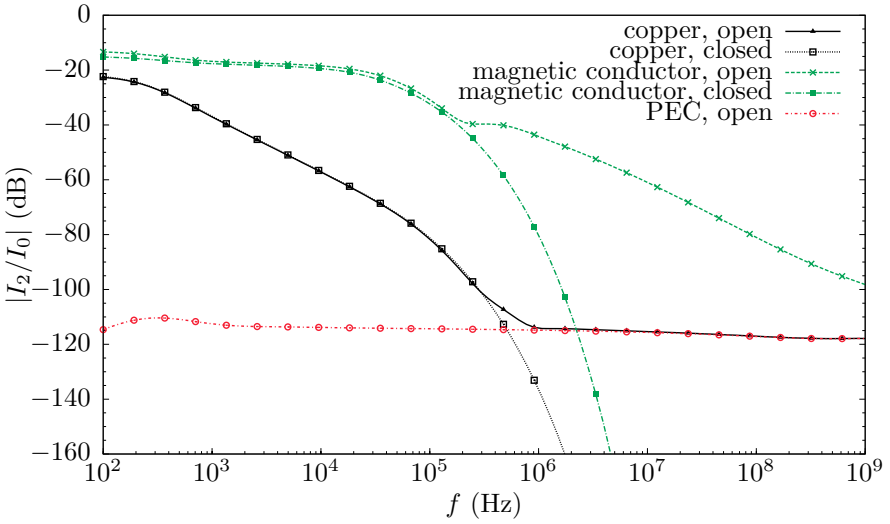

Figure 3.12: Shielding performance of the open ($g = 5.5$ mm) and closed ($g = 0$) cable tray as a function of frequency, for various shielding materials.

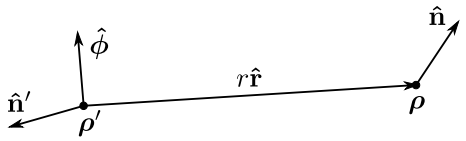

Figure 3.13: Relevant to the derivation of the normal derivatives.

3.8 Derivation of the Green's function's normal derivatives

Using the notations of Figure 3.13, the transverse gradients of the Green's function $G(\boldsymbol{\rho}-\boldsymbol{\rho}') = -\frac{j}{4}H_0^{(2)}(\gamma r)$ w.r.t. the observation point $\boldsymbol{\rho}$ and source point $\boldsymbol{\rho}'$ are given by

$$\nabla_t G(\boldsymbol{\rho}-\boldsymbol{\rho}') = -\nabla_t' G(\boldsymbol{\rho}-\boldsymbol{\rho}') = \frac{j\gamma}{4}H_1^{(2)}(\gamma r)\hat{\mathbf{r}}. \tag{3.28}$$

From these expressions, the normal derivatives of the Green's function follow immediately:

$$\frac{\partial G(\boldsymbol{\rho}-\boldsymbol{\rho}')}{\partial n} = \frac{j\gamma}{4}H_1^{(2)}(\gamma r)(\hat{\mathbf{n}}\cdot\hat{\mathbf{r}}), \tag{3.29}$$

$$\frac{\partial G(\boldsymbol{\rho}-\boldsymbol{\rho}')}{\partial n'} = -\frac{j\gamma}{4}H_1^{(2)}(\gamma r)(\hat{\mathbf{n}}'\cdot\hat{\mathbf{r}}). \tag{3.30}$$

Taking the gradient w.r.t. $\boldsymbol{\rho}'$ of (3.28) leads to the following dyadic, with the dot representing the derivative of a holomorphic function:

$$\begin{aligned}\nabla_t'\nabla_t G(\boldsymbol{\rho}-\boldsymbol{\rho}') &= -\nabla_t'\left(\frac{j\gamma}{4}\dot{H}_0^{(2)}(\gamma r)\right)\hat{\mathbf{r}} - \frac{j\gamma}{4}\dot{H}_0^{(2)}(\gamma r)\nabla_t'\hat{\mathbf{r}} \\ &= \frac{j\gamma^2}{4}\ddot{H}_0^{(2)}(\gamma r)\hat{\mathbf{r}}\hat{\mathbf{r}} + \frac{j\gamma}{4r}\dot{H}_0^{(2)}(\gamma r)\hat{\boldsymbol{\phi}}\hat{\boldsymbol{\phi}}.\end{aligned} \tag{3.31}$$

After some manipulations, the second order normal derivative of the Green's function can finally be written as

$$\begin{aligned}\frac{\partial^2 G(\boldsymbol{\rho}-\boldsymbol{\rho}')}{\partial n\partial n'} &= \hat{\mathbf{n}}'\cdot\nabla_t'\nabla_t G\cdot\hat{\mathbf{n}} \\ &= -\frac{j\gamma^2}{8}\left(H_0^{(2)}(\gamma r)+H_2^{(2)}(\gamma r)\right)\hat{\mathbf{n}}\cdot\hat{\mathbf{n}}' + \frac{j\gamma^2}{4}H_2^{(2)}(\gamma r)(\hat{\mathbf{n}}\cdot\hat{\mathbf{r}})(\hat{\mathbf{n}}'\cdot\hat{\mathbf{r}}).\end{aligned} \tag{3.32}$$

References

[1] D. Dobbelaere, H. Rogier, and D. De Zutter, "Accurate 2D MoM technique for arbitrary dielectric, magnetic and conducting media applied to shielding problems", in *URSI International Symposium on Electromagnetic Theory*, Hiroshima, Japan: IEEE, 2013, pp. 738–741.

[2] D. Dobbelaere, H. Rogier, and D. De Zutter, "Accurate 2.5-D boundary element method for conductive media", *Radio Science*, vol. 49, no. 6, pp. 389–399, 2014.

[3] G. Coluccini, M. Lucido, and G. Panariello, "Spectral domain analysis of open single and coupled microstrip lines with polygonal cross-section in bound and leaky regimes", *Microwave Theory and Techniques, IEEE Transactions on*, vol. 61, no. 2, pp. 736–745, 2013.

[4] M. Tong, G. Pan, and G. Lei, "Full-wave analysis of coupled lossy transmission lines using multiwavelet-based method of moments", *Microwave Theory and Techniques, IEEE Transactions on*, vol. 53, no. 7, pp. 2362–2370, 2005.

[5] D. Dobbelaere, H. Rogier, and D. De Zutter, "Properties and numerical solutions of dispersion curves in general isotropic waveguides", *IEEE Transactions on Microwave Theory and Techniques*, vol. 61, no. 9, pp. 3161–3168, 2013.

[6] D. Dobbelaere, H. Rogier, and D. De Zutter, "Analytic properties of dispersion curves for efficient eigenmode analysis of isotropic waveguides using a boundary element method", in *Proceedings of the IEEE International Conference on Numerical Electromagnetic Modeling and Optimization for RF, Microwave, and Terahertz Applications*, Pavia, Italy: IEEE, 2014, pp. 1–4.

[7] R. A. Murphy, C. G. Christodoulou, and R. L. Phillips, "Electromagnetic scattering from a finite cylinder with complex permittivity", *Proc. SPIE*, vol. 1558, pp. 295–305, 1991.

[8] D. Wilton, S. Rao, A. Glisson, D. Schaubert, O. Al-Bundak, and C. Butler, "Potential integrals for uniform and linear source distributions on polygonal and polyhedral domains", *Antennas and Propagation, IEEE Transactions on*, vol. 32, no. 3, pp. 276 –281, Mar. 1984.

[9] P. Yla-Oijala and M. Taskinen, "Calculation of CFIE impedance matrix elements with RWG and n $\times$ RWG functions", *Antennas and Propagation, IEEE Transactions on*, vol. 51, no. 8, pp. 1837 –1846, Aug. 2003.

[10] R. Graglia, "On the numerical integration of the linear shape functions times the 3-D Green's function or its gradient on a plane triangle", *Antennas and Propagation, IEEE Transactions on*, vol. 41, no. 10, pp. 1448 –1455, Oct. 1993.

[11] M. Khayat and D. Wilton, "Numerical evaluation of singular and near-singular potential integrals", *Antennas and Propagation, IEEE Transactions on*, vol. 53, no. 10, pp. 3180 –3190, Oct. 2005.

[12] R. Graglia and G. Lombardi, "Machine precision evaluation of singular and nearly singular potential integrals by use of Gauss quadrature formulas for rational functions", *Antennas and Propagation, IEEE Transactions on*, vol. 56, no. 4, pp. 981 –998, Apr. 2008.

[13] A. Polimeridis and J. Mosig, "Evaluation of weakly singular integrals via generalized cartesian product rules based on the double exponential formula", *Antennas and Propagation, IEEE Transactions on*, vol. 58, no. 6, pp. 1980 –1988, Jun. 2010.

[14] S. Chakraborty and V. Jandhyala, "Evaluation of Green's function integrals in conducting media", *Antennas and Propagation, IEEE Transactions on*, vol. 52, no. 12, pp. 3357 –3363, Dec. 2004.

[15] S. Rao, D. Wilton, and A. Glisson, "Electromagnetic scattering by surfaces of arbitrary shape", *Antennas and Propagation, IEEE Transactions on*, vol. 30, no. 3, pp. 409 –418, May 1982.

[16] J. Peeters, I. Bogaert, and D. De Zutter, "Calculation of MoM interaction integrals in highly conductive media", *Antennas and Propagation, IEEE Transactions on*, vol. 60, no. 2, pp. 930–940, 2012.

[17] A. Poggio and E. Miller, "Integral equation solution of three-dimensional scattering problems", in *Computer Techniques for Electromagnetics*, R. Mittra, Ed., Pergamon Press, 1973, ch. 4.

[18] Y. Chang and R. Harrington, "A surface formulation for characteristic modes of material bodies", *Antennas and Propagation, IEEE Transactions on*, vol. 25, no. 6, pp. 789 –795, Nov. 1977.

[19] T. Wu and L. Tsai, "Scattering from arbitrarily-shaped lossy dielectric bodies of revolution", *Radio Science*, pp. 709–718, Sep. 1977.

[20] F. Olyslager, D. De Zutter, and K. Blomme, "Rigorous analysis of the propagation characteristics of general lossless and lossy multiconductor transmission lines in multilayered media", *Microwave Theory and Techniques, IEEE Transactions on*, vol. 41, no. 1, pp. 79 –88, Jan. 1993.

[21] J. Fostier, B. Michiels, I. Bogaert, and D. D. Zutter, "A Fast 2D Parallel MLFMA Solver for Oblique Plane Wave Incidence", *Radio Science*, Nov. 2011.

[22] G. Watson, *A Treatise on the Theory of Bessel Functions*. Cambridge University Press, 1995, Cambridge Mathematical Library.

[23] F. W. Olver, D. W. Lozier, R. F. Boisvert, and C. W. Clark, *NIST Handbook of Mathematical Functions*. New York, NY, USA: Cambridge University Press, 2010.

[24] I. S. Gradshteyn and I. M. Ryzhik, *Table of Integrals, Series and Products, seventh edition*. Academic Press, 2007.

[25] J. Van Bladel, *Electromagnetic Fields*. John Wiley & Sons, 2007, IEEE Press Series on Electromagnetic Wave Theory.

[26] R. Ziolkowski, "n-Series problems and the coupling of electromagnetic waves to apertures: a Riemann-Hilbert approach", *SIAM Journal on Mathematical Analysis*, vol. 16, no. 2, pp. 358–378, 1985.

[27] R. Ziolkowski and J. Grant, "Scattering from cavity-backed apertures: the generalized dual series solution of the concentrically loaded E-pol slit cylinder problem", *Antennas and Propagation, IEEE Transactions on*, vol. 35, no. 5, pp. 504–528, 1987.

[28] W.-S. Lee, H.-L. Lee, H.-S. Jang, H.-S. Tae, and J.-W. Yu, "Analysis of scattering with multi-slotted cylinder with thickness: TM case", *Progress In Electromagnetics Research*, vol. 128, pp. 105–120, 2012.

[29] S. Celozzi, R. Araneo, and G. Lovat, *Electromagnetic Shielding*. John Wiley & Sons, 2008, Wiley Series in Microwave and Optical Engineering.

4

Analytic Properties of Dispersion Curves for an Efficient Full-Wave Multiconductor Waveguide Analysis

based on the contributions [1] and [2]

★ ★ ★

In this chapter, some properties of numerical dispersion curves in general isotropic piecewise homogeneous waveguides are rigorously derived. These properties are leveraged in a numerical implementation capable of determining the dispersion curves and eigenmodes of such waveguides with cross-sectional materials that can be highly conductive (such as copper). The influence of a lossy shielding conductor on the complex modes of a shielded dielectric image guide is investigated for the first time. Another numerical example illustrates the proposed full-wave modal analysis of a multiconductor waveguide, whose efficiency stems from incorporating the derived theorems.

4.1 Introduction

The recent development of computer-based information systems shows a clear tendency towards higher bit rates and miniaturization of (opto-)electronic components. The design of reliable information-carrying waveguides, driven at high frequencies to sustain the bandwidth requirements, is hampered by the

presence of modal dispersion, crosstalk and losses. Accurate prediction of all electromagnetic phenomena occurring in the waveguide cross section, including the dispersion curves of the eigenmode propagation constants, is of utmost importance for the design and optimization of wave-guiding structures. This chapter derives properties that contribute to this goal, and presents an efficient full-wave modal analysis of waveguides (cf. section 2.5).

There are many techniques available, developed during the past decades, to determine waveguide propagation characteristics. The effective dielectric constant method is an approximate technique that has been used to predict the dispersion relations of several types of dielectric waveguides [3]. However, it only works well under certain assumptions.

The mode-matching technique [4], [5] has the benefits of being both exact (provided a sufficient number of modes is considered) and yielding full modal information, i.e., both propagation constants and modal field distributions. The method requires that the individual constituents of the cross section are of simple geometrical shape, such that the modes can be determined analytically.

Finite difference and finite element techniques have been successfully applied to the analysis of dielectric waveguide structures [6], [7]. Advantages of the methods are the easy incorporation of inhomogeneous material regions, where the material parameters can vary continuously as a function of place, and the straightforward determination of the modal characteristics by solving an eigenvalue problem. Although its linear system is sparse, the employed volume discretization technique can yield a large number of unknowns in comparison with a boundary element method. Moreover, the analysis of open waveguides is somewhat problematic, as it leads to a larger simulation domain and the introduction of (non-perfect) boundary conditions or an absorbing layer at the boundary. Finally, these methods require a sufficiently fine mesh in regions with rapid field variations, and, therefore, become infeasible in highly conductive regions with skin effect phenomena.

Methods based on the Green's functions of the material regions can be classified into domain and boundary integral methods. The first type was used to study the properties of open planar stratified dielectric waveguides with embedded inhomogeneous material regions [8], [9]. For waveguides with piecewise homogeneous material regions, a boundary integral formulation was applied to analyze dielectric waveguides and lossy multiconductor transmission lines in multilayered media [10], [11]. However, the use of a spectral representation of the Green's function in [10] requires a final spatial inverse Fourier transform, which becomes numerically infeasible for material regions with high losses. For open waveguides, Green's function based methods automatically ensure the radiation conditions at infinity and the prediction of leaky waves. Moreover, less unknowns are needed than with a finite difference or finite element method, as only the inhomogeneous domains and boundaries of piecewise homogeneous domains need to be meshed. Drawbacks of the methods are the non-sparseness

of the resulting linear system and the less trivial determination of the dispersion curves, based on the search of the (complex) zeros of the system matrix's determinant.

The study of modal interactions has been thoroughly investigated in the past [12], [13], and the smoothness of the characteristic determinant in the dispersion equation is generally taken as an *ansatz* (based on the physical nature of the problem). In this chapter, we investigate the behavior of a single dispersion curve in general isotropic waveguides. The numerical description allows us to explicitly establish the (domain of) holomorphy of the characteristic determinant and prove some useful theorems regarding the properties of dispersion curves. The explicit incorporation of the numerical framework in the derived properties is by no means a limitation, considering existing convergence theorems, but this has not been investigated in this chapter.

A Green's function based boundary element method is employed to calculate the dispersion curves of waveguides with arbitrarily shaped piecewise homogeneous material regions. Use of a technique to evaluate method of moments (MoM) interaction integrals in highly conductive materials allows the treatment of both dielectric and electric waveguides with non-perfect conductors. As the formulation is based on a two-dimensional version of the PMCHWT (Poggio-Miller-Chang-Harrington-Wu-Tsai) integral equation [14]–[16], spurious modes are nonexistent. It is shown that the evolution of a propagation constant in the complex plane as a function of frequency can be tracked efficiently based on the derived theorems.

In section 4.2, the geometry of the considered waveguides is presented, along with the employed boundary integral equations. The obtained system of coupled integral equations is then transformed to a finite-dimensional linear system by means of the MoM, as explained in section 4.3. Some properties regarding the MoM system matrix that will be needed in the sequel are also derived. The properties of the dispersion curves that simplify and speed up a numerical implementation are derived in section 4.4. Section 4.5 discusses these numerical techniques to search for and track the propagation constants in the complex plane as a function of frequency. Numerical examples demonstrating the correctness and accuracy of the methods are presented in section 4.6.

4.2 Geometry and Boundary Integral Equations

Consider a waveguide whose cross section, in line with assumption (2.1) of section 2.1, is the union of linear isotropic piecewise homogeneous material regions Ω_i characterized by their *complex* electric permittivity ϵ_i and magnetic permeability μ_i, with Ω_0 the only unbounded domain. Assume that all sources and fields have a common time and longitudinal dependence $e^{j(\omega t-\beta z)}$ ($\beta \in \mathbb{C}$), i.e., the time- and space-harmonic Maxwell equations (1.13)–(1.16) hold for the phasor fields. The unknowns of the problem are the phasors of the time-

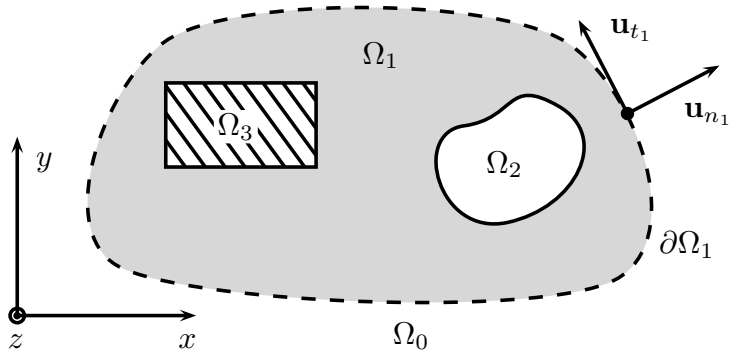

Figure 4.1: Waveguide cross section with arbitrarily shaped piecewise homogeneous material regions

and space-harmonic tangential electric and magnetic boundary fields, given by $\hat{\mathbf{n}}\times\mathbf{E}\times\hat{\mathbf{n}} = E_t\hat{\mathbf{t}}+E_z\hat{\mathbf{z}}$ and $\hat{\mathbf{n}}\times\mathbf{H}\times\hat{\mathbf{n}} = H_t\hat{\mathbf{t}}+H_z\hat{\mathbf{z}}$, with E_t and H_t the transverse tangential components, E_z and H_z the longitudinal components, $\hat{\mathbf{n}}$ the outward unit normal to Ω_i and $\hat{\mathbf{t}} = \hat{\mathbf{z}} \times \hat{\mathbf{n}}$. The representation formulas (1.34)–(1.37) hold, with $E_t^{(i)}\hat{\mathbf{t}} + E_z^{(i)}\hat{\mathbf{z}}$ and $H_t^{(i)}\hat{\mathbf{t}} + H_z^{(i)}\hat{\mathbf{z}}$ the incoming tangential electric and magnetic field generated by sources in Ω_i, respectively, $\tilde{\Gamma}$ the boundary of Ω_i, $\boldsymbol{\rho} = x\hat{\mathbf{x}} + y\hat{\mathbf{y}}$, $\epsilon = \epsilon_i$, $\mu = \mu_i$ and $\gamma = \gamma_i = \sqrt{\omega^2\epsilon_i\mu_i - \beta^2}$.

A system of coupled integral equations is obtained after imposing continuity of the tangential fields at the boundaries, yielding a 2.5-D version of the PMCHWT (Poggio-Miller-Chang-Harrington-Wu-Tsai) operator [14]–[16]. A finite-dimensional linear system is obtained with the MoM, as explained in the next section. The incoming tangential electric and magnetic fields $E_t^{(i)}\hat{\mathbf{t}} + E_z^{(i)}\hat{\mathbf{z}}$ and $H_t^{(i)}\hat{\mathbf{t}} + H_z^{(i)}\hat{\mathbf{z}}$, respectively, are due to sources in Ω_i, and contribute to the right hand side vector of the matrix equation after discretization in the MoM [17]. However, in an eigenmode analysis, no sources are present, implying that $E_t^{(i)} = E_z^{(i)} = H_t^{(i)} = H_z^{(i)} = 0$ in (1.34)–(1.37).

4.3 Discretized System with the Method of Moments

4.3.1 Properties of the Interaction Integrals

First, we briefly recall which types of interaction integrals occur in the MoM of the 2.5-D PMCHWT boundary integral equation [10], [17].

Assume that the boundaries $\partial\Omega_i$ are approximated by a union (denoted Γ_i) of straight segments S_j with length l_j and end points $\boldsymbol{\rho}_j$ and $\boldsymbol{\rho}_{j+1}$ (Fig. 4.2),

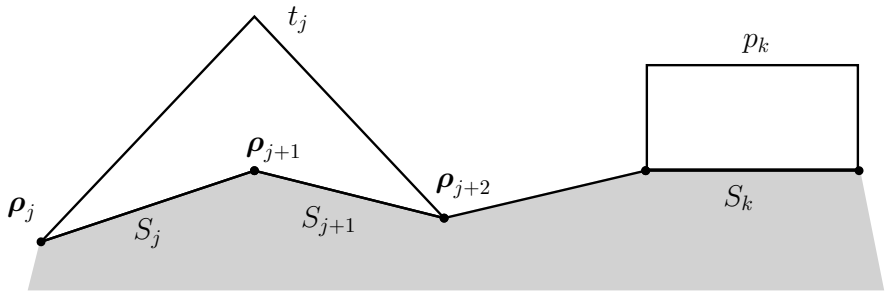

Figure 4.2: The boundaries are approximated by means of straight segments, over which triangular and pulse functions are defined

although the properties and numerical techniques derived in this chapter still hold for general curved segments. Following [10], the transverse tangential components E_t and H_t are expanded into pulse functions $p_j(\boldsymbol{\rho})$, with support over segment S_j, whereas the longitudinal components E_z and H_z are expanded into triangular functions $t_j(\boldsymbol{\rho})$, with support over S_j and S_{j+1}:

$$p_j(\boldsymbol{\rho}) = \frac{1}{l_j} \qquad \boldsymbol{\rho} \in S_j, \tag{4.1}$$

$$t_j(\boldsymbol{\rho}) = \begin{cases} 1 - |\boldsymbol{\rho} - \boldsymbol{\rho}_{j+1}|\ l_j^{-1} & \boldsymbol{\rho} \in S_j \\ 1 - |\boldsymbol{\rho} - \boldsymbol{\rho}_{j+1}|\ l_{j+1}^{-1} & \boldsymbol{\rho} \in S_{j+1}. \end{cases} \tag{4.2}$$

Moreover, a Petrov-Galerkin approach is employed, after choosing the same set of basis and test functions. Testing the continuity equations of the longitudinal components E_z and H_z with pulse functions, and the equations for E_t and H_t are with triangular functions leads to a stable discretization [10]. To calculate the elements in the PMCHWT MoM system matrix, the interaction integrals (4.3)–(4.5) below are evaluated numerically for basis functions, denoted p_k and t_k, and test functions, denoted p_j and t_j, with support over segments that have Ω_i as a neighboring medium, with $\tilde{\Gamma} = \Gamma_i$ the (approximated) boundary of Ω_i. This can easily be seen by inspecting (1.34) and (1.35). The tangential derivatives of the Green's function can be transferred to the test function using Stokes' theorem such that only the three types of interaction integrals (4.3)–(4.5) remain.

$$\mathsf{I}_{jk}^{(1)} = \int_{\tilde{\Gamma}} p_j(\boldsymbol{\rho}) \mathrm{d}c \int_{\tilde{\Gamma}} G(\boldsymbol{\rho} - \boldsymbol{\rho}')\ p_k(\boldsymbol{\rho}') \mathrm{d}c', \tag{4.3}$$

$$\mathsf{I}_{jk}^{(2)} = \int_{\tilde{\Gamma}} p_j(\boldsymbol{\rho}) \mathrm{d}c \int_{\tilde{\Gamma}} \frac{\partial G(\boldsymbol{\rho} - \boldsymbol{\rho}')}{\partial n'} t_k(\boldsymbol{\rho}') \mathrm{d}c', \tag{4.4}$$

$$\mathsf{I}_{jk}^{(3)} = \int_{\tilde{\Gamma}} t_j(\boldsymbol{\rho}) \mathrm{d}c \int_{\tilde{\Gamma}} \frac{\partial^2 G(\boldsymbol{\rho} - \boldsymbol{\rho}')}{\partial n \partial n'} t_k(\boldsymbol{\rho}') \mathrm{d}c'. \tag{4.5}$$

More explicitly, one can rewrite the interaction integrals as in (4.6)–(4.8) (see section 3.8 and Fig. 3.13). Note that the inner integral of the last type is to be interpreted in Hadamard finite part sense (p.f.).

$$\mathsf{I}_{jk}^{(1)} = -\int_{\tilde{\Gamma}} p_j(\boldsymbol{\rho}) \int_{\tilde{\Gamma}} \frac{j}{4} H_0^{(2)}(\gamma_i r)\; p_k(\boldsymbol{\rho}')\; \mathrm{d}c'\; \mathrm{d}c, \tag{4.6}$$

$$\mathsf{I}_{jk}^{(2)} = -\int_{\tilde{\Gamma}} p_j(\boldsymbol{\rho}) \int_{\tilde{\Gamma}} \frac{j\gamma_i}{4} H_1^{(2)}(\gamma_i r)(\hat{\mathbf{n}}' \cdot \hat{\mathbf{r}})\; t_k(\boldsymbol{\rho}')\; \mathrm{d}c'\mathrm{d}c, \tag{4.7}$$

$$\begin{aligned}\mathsf{I}_{jk}^{(3)} = \int_{\tilde{\Gamma}} t_j(\boldsymbol{\rho})\; p.f. \int_{\tilde{\Gamma}} \Bigg[& \frac{j\gamma_i^2}{4} H_2^{(2)}(\gamma_i r)(\hat{\mathbf{n}}\cdot\hat{\mathbf{r}})(\hat{\mathbf{n}}'\cdot\hat{\mathbf{r}}) \\ & -\frac{j\gamma_i^2}{8}\left(H_0^{(2)}(\gamma_i r) + H_2^{(2)}(\gamma_i r)\right)\hat{\mathbf{n}}\cdot\hat{\mathbf{n}}' \Bigg]\; t_k(\boldsymbol{\rho}')\; \mathrm{d}c'\mathrm{d}c. \end{aligned} \tag{4.8}$$

Consider a fixed mesh $\tilde{\Gamma}$, independent* of the frequency ω and longitudinal wavenumber β. The branch cuts $\mathcal{B}_i(\omega)$ of the transversal wavenumber $\gamma_i = \sqrt{\omega^2\epsilon_i\mu_i - \beta^2}$ at the frequency ω are chosen on the hyperbola in the complex β-plane with the real and imaginary axes as asymptotes such that $\Im\gamma_i < 0$ for $\beta \in (\mathbb{C} \setminus \mathcal{B}_i(\omega))$ [18]. Likewise, denote $\widetilde{\mathcal{B}}_i(\beta)$ as the branch cuts of γ_i, for a fixed β and viewed as a function of ω, such that $\Im\gamma_i < 0$ for $\omega \in (\mathbb{C} \setminus \widetilde{\mathcal{B}}_i(\beta))$. It is easy to see that $\gamma_i(\omega, \beta)$ is a holomorphic function of the two variables ω and β in the domain $\mathcal{O}_i = \mathbb{C}^2 \setminus \{(\omega, \beta) \mid \beta \in \mathcal{B}_i(\omega)\} = \mathbb{C}^2 \setminus \{(\omega, \beta) \mid \omega \in \widetilde{\mathcal{B}}_i(\beta)\}$. It will be proved in the following theorems that the interaction integrals (4.6)–(4.8) are also holomorphic functions of ω and β in $\mathcal{O}_i$.

Theorem 4.3.1. *Given $\nu \in \mathbb{N}$. Suppose $a(r)$ is a piecewise continuous complex function of a positive real argument $r > 0$ that vanishes for $r > R$. Then, if the function $F(\omega, \beta) = \lim_{\epsilon\to 0}\int_\epsilon^R a(r)H_\nu^{(2)}(\gamma_i(\omega,\beta)r)dr$ converges as an improper Riemann integral in $\mathcal{O}_i = \mathbb{C}^2 \setminus \{(\omega, \beta) \mid \beta \in \mathcal{B}_i(\omega)\}$, it is holomorphic in $\mathcal{O}_i$.*

Proof. Suppose that $F(\omega, \beta)$ converges as an improper Riemann integral in $\mathcal{O}_i$. We will first prove that, for fixed ω_0, $F(\omega_0, \beta)$ is holomorphic in the variable $\beta \in \Psi = \mathbb{C} \setminus \mathcal{B}_i(\omega_0)$. Consider a fixed $\epsilon > 0$. Thanks to the choice of the branch cuts $\mathcal{B}_i(\omega_0)$, $H_\nu^{(2)}(\gamma_i(\omega_0, \beta)r)$ is holomorphic for $r > 0$ and $\beta \in \Psi$. As by assumption $F_\epsilon(\beta) = \int_\epsilon^R a(r)H_\nu^{(2)}(\gamma_i(\omega_0,\beta)r)dr$ is Riemann integrable in Ψ, the sequence of its holomorphic Riemann sums converges uniformly on all compact subsets of Ψ. Therefore, for each value of ϵ, the limit of this sequence of holomorphic Riemann sums, namely $F_\epsilon(\beta)$, is found to be holomorphic too, by a well-known theorem of Weierstrass. As $\lim_{\epsilon\to 0} F_\epsilon(\beta)$ exists, the sequence of the holomorphic functions $F_{1/n}(\beta)$ for $n \to \infty$ also converges uniformly on all

*suppose that $\tilde{\Gamma}$ is sufficiently fine to model all wave phenomena in the frequency and longitudinal wavenumber range of interest

compact subsets of Ψ, implying that the limit function $F(\omega_0, \beta) = \lim_{\epsilon \to 0} F_\epsilon(\beta)$ is holomorphic in Ψ.

Completely analogously, one can prove that, for fixed β_0, $F(\omega, \beta_0)$ is holomorphic as a function of ω in $\mathbb{C} \setminus \widetilde{\mathcal{B}}_i(\beta_0)$. Application of Hartogs' fundamental theorem, also called the separate analyticity theorem [19], leads to the proposition. □

Theorem 4.3.2 (Holomorphy of the interaction integrals)**.** *The interaction integrals (4.6)–(4.8) are holomorphic functions of the two complex variables ω and β in the domain $\mathcal{O}_i$.*

Proof. It can be shown that interactions of the form (4.6) and (4.7) can be reduced to the form of $F(\omega, \beta)$ in theorem 4.3.1, which converges as an improper Riemann integral in $\mathcal{O}_i$. Interactions of the last form (4.8) cannot be written straightforwardly as an improper Riemann integral if the kernel in the integration domain contains a hypersingularity. By extracting the hypersingular part of the second order Hankel function, the regularized integrand is (improperly, if basis and test functions are overlapping or tangent) Riemann integrable, and by arguments similar to the proof in theorem 4.3.1, the integral leads to a holomorphic function in $\mathcal{O}_i$. The finite part integral of the hypersingular part is independent of ω and β, and thus trivially holomorphic. Indeed, it is given by:

$$\begin{aligned}\mathsf{I}^{(3)}_{jk,\mathsf{sing}} = \int_{\tilde{\Gamma}} t_j(\boldsymbol{\rho})\ \mathrm{d}c \quad p.f. \int_{\tilde{\Gamma}} \frac{1}{2\pi r^2} \big[\hat{\mathbf{n}} \cdot \hat{\mathbf{n}}' \\ - 2(\hat{\mathbf{n}} \cdot \hat{\mathbf{r}})(\hat{\mathbf{n}}' \cdot \hat{\mathbf{r}})\big]\ t_k(\boldsymbol{\rho}')\ \mathrm{d}c'.\end{aligned}$$

This lets us conclude that the interaction integrals are holomorphic functions of ω and β in $\mathcal{O}_i$. □

4.3.2 Properties of the System Matrix

We denote the MoM system matrix at frequency ω and longitudinal wavenumber β as $\mathsf{M}(\omega, \beta) \in \mathbb{C}^{n \times n}$, i.e., it has the same dimension n for all ω and β, resulting from the earlier assumed fixed discretization of the boundaries $\partial\Omega_i$. Its determinant will be written as $\mathfrak{D}(\omega, \beta) = \det \mathsf{M}(\omega, \beta)$. The employed methods to search for propagation constants of the waveguide, discussed in section 4.4, rely on the determination of the zeros of $\mathfrak{D}(\omega, \beta)$ in the β-plane. A few interesting properties of the dispersion curves as a function of frequency can be proved, taking into account the holomorphy of the determinant. The latter is the subject of the following theorems.

Theorem 4.3.3 (Holomorphy of the matrix elements)**.** *The matrix elements of $\mathsf{M}(\omega, \beta)$ are holomorphic functions of ω and β in the domain $\mathcal{O} = (\mathbb{C}_0 \times \mathbb{C}) \setminus (\cup_i \{(\omega, \beta) \mid \beta \in \mathcal{B}_i(\omega)\})$.*

Proof. The discretized linear system arises after expanding the tangential boundary field components into a set of basis functions and imposing moments of the continuity relations, arising from the representation formulas (1.34)–(1.37), as explained in section 4.2. Therefore, each matrix element can be written as a finite sum of products of the prototype integrals (4.6)–(4.8) (that are holomorphic in $\cap_i \mathcal{O}_i$, by theorem 4.3.2) with functions that are holomorphic in $\mathcal{O}$ (note that some factors have a pole at $\omega = 0$). □

Theorem 4.3.4 (Holomorphy of the determinant)**.** *The system matrix determinant $\mathfrak{D}(\omega, \beta)$ is holomorphic as a function of ω and β in the domain $\mathcal{O}$, defined in theorem 4.3.3.*

Proof. This follows immediately from theorem 4.3.3 and the fact that the determinant is a finite sum of finite products of matrix elements (up to a sign). □

The following theorem discusses the symmetry of the matrix determinant as a function of β, if the cross section consists entirely of *lossless* materials. This property implies that the numerically found complex waves (cf. Fig. 2.5(a)) always come in pairs with complex conjugate propagation constants.

Theorem 4.3.5 (Symmetry property of the determinant for lossless structures)**.** *Suppose $\epsilon_i, \mu_i \in \mathbb{R}_0$ and $(\omega, \beta) \in \mathcal{O}$, then $\mathfrak{D}(\omega, \overline{\beta}) = \overline{\mathfrak{D}(\omega, \beta)}$, where $\overline{a}$ stands for the complex conjugate of a.*

Proof. We shall make use of the identity $H_n^{(2)}(-\overline{z}) = (-1)^{n+1}\overline{H_n^{(2)}(z)}$ if $\Im z < 0$ and $n \in \mathbb{Z}$, which can be proved using elementary properties of Bessel functions [20]. When we replace β with $\overline{\beta}$ in the interaction integrals (4.6)–(4.8), we can use the previous identity for $(\omega, \beta) \in \mathcal{O}$, as then $\Im(\gamma_i r) < 0$. Note that in the process of replacing $\beta \to \overline{\beta}$, we have $\gamma_i \to -\overline{\gamma_i}$ and $\gamma_i^2 \to \overline{\gamma_i^2}$. This lets us conclude that $\mathsf{I}_{jk}^{(1)} \to \overline{\mathsf{I}_{jk}^{(1)}}$, $\mathsf{I}_{jk}^{(2)} \to \overline{\mathsf{I}_{jk}^{(2)}}$ and $\mathsf{I}_{jk}^{(3)} \to \overline{\mathsf{I}_{jk}^{(3)}}$ if $\beta \to \overline{\beta}$. By examining the additional factors in the representation formulas (1.34)–(1.37), it can be seen that some contributions, for example H_t as a source for E_z (denoted $[E_z H_t]$), will be transformed according to $[E_z H_t] \to -\overline{[E_z H_t]}$. Others, for example E_z as a source for E_z, will be transformed according to $[E_z E_z] \to \overline{[E_z E_z]}$. However, $\mathsf{M}(\omega, \overline{\beta})$ and $\overline{\mathsf{M}(\omega, \beta)}$ will only differ up to a multiplication of the same number of columns and rows with -1. This leads to the proposition. □

4.4 Properties of the Dispersion Curves

Given $(\omega_0, \beta_0) \in \mathcal{O}$, with $\omega_0 \in \mathbb{R}_0^+$. Suppose that β_0 is a zero of the determinant at the operating frequency ω_0, i.e., $\mathfrak{D}(\omega_0, \beta_0) = 0$. In the current context, β_0 corresponds to the propagation constant of one or more eigenmodes that can

exist in the structure. As a consequence of Hartogs' lemma, also called the Osgood-Brown theorem [19], the zero (ω_0, β_0) cannot be an isolated one. The Weierstrass preparation theorem and the fact that $\mathfrak{D}(\omega, \beta)$ may be expressed a power series around (ω_0, β_0), which has a term only involving $\beta - \beta_0$, independent of $\omega - \omega_0$ (otherwise $\mathfrak{D}(\omega_0, \beta)$ would be identically zero in the neighborhood where the power series holds, and thus, by analytic continuation, the determinant would vanish for $\omega = \omega_0$), allows to write the following local representation for $\mathfrak{D}(\omega, \beta)$, valid in a neighborhood* $U_\epsilon = B(\omega_0, \epsilon) \times B(\beta_0, \epsilon)$ of (ω_0, β_0) [21]:

$$\mathfrak{D}(\omega, \beta) = \left[(\beta - \beta_0)^\nu + \sum_{i=0}^{\nu-1} c_i(\omega)(\beta - \beta_0)^i \right] \phi(\omega, \beta), \tag{4.9}$$

where $\phi(\omega, \beta)$ is holomorphic and zero-free in U_ϵ, $\nu \in \mathbb{N}_0$ and the functions $c_i(\omega)$ are holomorphic in $B(\omega_0, \epsilon)$ and vanish at ω_0. From (4.9), it is clear that the zero β_0 of the function $\mathfrak{D}(\omega_0, \beta)$ has multiplicity ν. The following theorem describes the behavior of this zero as a function of ω, in a neighborhood of ω_0 on the real axis.

Theorem 4.4.1 (Behavior of a dispersion curve as a function of frequency)**.** *Suppose that (ω_0, β_0) is a zero of $\mathfrak{D}(\omega, \beta)$ with multiplicity ν, with $\omega_0 \in \mathbb{R}_0^+$ and U_ϵ a neighborhood of (ω_0, β_0) where (4.9) holds. If, for each ω in a real interval $(a, b) \subset (\omega_0 - \epsilon, \omega_0 + \epsilon)$ (with $b > a$), it holds that $\mathfrak{D}(\omega, \beta)$ has exactly one zero $(\omega, \beta_1(\omega))$ with multiplicity ν in U_ϵ, then the same holds for all $\omega \in B(\omega_0, \epsilon)$, for which $\mathfrak{D}(\omega, \beta)$ has zeros inside U_ϵ. Moreover, the dispersion curve of the zero $\beta_1(\omega)$ inside U_ϵ will be smooth.*

Proof. For $\omega \in (a, b)$, there is only one zero with multiplicity ν inside U_ϵ. This means that the term in brackets in (4.9) is uniquely factorized in the following way, for $\omega \in (a, b)$:

$$(\beta - \beta_0)^\nu + \sum_{i=0}^{\nu-1} c_i(\omega)(\beta - \beta_0)^i = (\beta - \beta_1(\omega))^\nu \tag{4.10}$$

$$= \sum_{i=0}^{\nu} \binom{\nu}{i} (-1)^{\nu-i} (\beta - \beta_0)^i (\beta_1(\omega) - \beta_0)^{\nu-i}. \tag{4.11}$$

This implies that $c_i(\omega) = \binom{\nu}{i}(-1)^{\nu-i}(\beta_1(\omega) - \beta_0)^{\nu-i}$ for $i = 0, 1, ..., \nu - 1$. Or, equivalently, the following relations hold:

$$\beta_1(\omega) = \beta_0 - \frac{1}{\nu} c_{\nu-1}(\omega), \tag{4.12}$$

$$c_i(\omega) = \binom{\nu}{i} \left(\frac{c_{\nu-1}(\omega)}{\nu} \right)^{\nu-i}. \tag{4.13}$$

*$B(z_0, \epsilon) = \{z \in \mathbb{C} : |z - z_0| < \epsilon\}$, is the open disk centered at z_0 with radius ϵ, whereas $\overline{B}(z_0, \epsilon)$ denotes its closure.

As the interval (a, b) *contains* a limit point, the relations (4.13) will hold for all $\omega \in B(\omega_0, \epsilon)$. Thus, the factorization (4.10) holds in the whole neighborhood U_ϵ, implying that for all $\omega \in B(\omega_0, \epsilon)$, for which $\mathfrak{D}(\omega, \beta)$ has zeros inside U_ϵ, the zero is unique and has multiplicity ν. From (4.12), it clear that $\beta_1(\omega)$ is holomorphic in $B(\omega_0, \epsilon)$ and thus smooth for $\omega \in (\omega_0 - \epsilon, \omega_0 + \epsilon)$. □

Corollary 4.4.2 (Dispersion curves cannot split up by themselves)**.** Suppose that $\beta_1(\omega)$ is a complex-valued function of real argument $\omega \in (\omega_0 - \epsilon, \omega_0]$, representing a zero of the determinant with constant multiplicity ν, i.e., $\mathfrak{D}(\omega, \beta_1(\omega)) = 0$. Then there exists a $\delta > 0$ such that $\beta_1(\omega)$ can be smoothly extended to the interval $\omega \in (\omega_0 - \epsilon, \omega_0 + \delta)$, still obeying $\mathfrak{D}(\omega, \beta_1(\omega)) = 0$ with multiplicity ν. Therefore, dispersion curves cannot split up by themselves. There has to be at least an intersection with another curve or an intersection with a branch cut $\mathcal{B}_i(\omega)$.

Fig. 4.3 visualizes some implications of corollary 4.4.2. The bifurcation of the dispersion curve $\beta_1(\omega)$ at the frequency ω_0 is possible, as this happens on the branch cut $\mathcal{B}_i(\omega_0)$. A physical example of this situation is the bifurcation of a mode into two complex modes [22]. However, the bifurcation of $\beta_2(\omega)$ at ω_0 is not possible, as it would violate corollary 4.4.2.

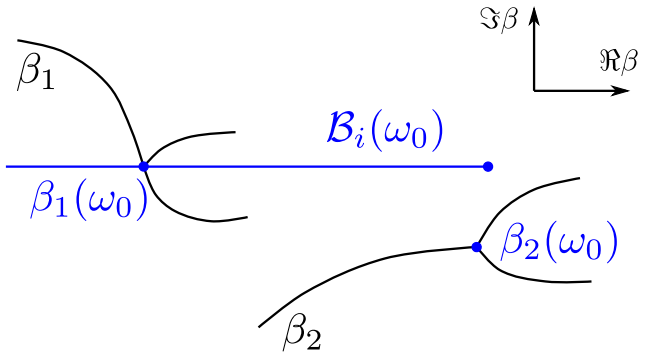

Figure 4.3: Corollary 4.4.2 implies that the bifurcation of the dispersion curve $\beta_1(\omega)$ at the frequency ω_0 is possible, as it happens on the branch cut $\mathcal{B}_i(\omega_0)$. However, the bifurcation of $\beta_2(\omega)$ at ω_0 is not possible.

The following theorem provides a connection between the multiplicity of a propagation constant and the dimension of the null space of the system matrix.

Theorem 4.4.3. *Suppose $\mathfrak{D}(\omega_0, \beta_0) = 0$, i.e., β_0 is a zero at the frequency ω_0 with multiplicity $\nu(\beta_0)$. Denote the nullity of the MoM matrix as $\nu(\mathsf{M}(\omega_0, \beta_0))$. Then $\nu(\mathsf{M}(\omega_0, \beta_0)) \leq \nu(\beta_0)$.*

Proof. As $\mathsf{M}(\omega_0, \beta)$ is an square matrix of dimension n with holomorphic elements in a neighborhood of β_0 (see theorem 4.3.3), it can there be expanded into the following Taylor series:

$$\mathsf{M}(\omega_0, \beta) = \sum_{i=0}^{\infty} \mathsf{M}_i (\beta - \beta_0)^i, \tag{4.14}$$

with $\mathsf{M}_i \in \mathbb{C}^{n \times n}$ and, as β_0 is a zero of the determinant function, $\det \mathsf{M}_0 = 0$. Suppose the dimension of the null space of the matrix M_0 is equal to ν_0, i.e., $\nu_0 = \nu(\mathsf{M}_0) = \nu(\mathsf{M}(\omega_0, \beta_0))$. Now let us write the determinant function in the following form:

$$\mathfrak{D}(\beta) = \det \left(\sum_{i=0}^{\infty} \mathsf{M}_i (\beta - \beta_0)^i \right) = \sum_{j=0}^{\infty} \alpha_j (\beta - \beta_0)^j, \tag{4.15}$$

with $\alpha_j \in \mathbb{C}$, with $\alpha_0 = 0$. Let us look at a term $\alpha_j (\beta - \beta_0)^j$ for $0 < j < \nu_0$. It can be seen that α_j can be written as a sum of determinants of matrices M_0 with $k \leq j$ rows replaced by corresponding rows of the matrices M_i (for $i > 0$). Because only $k \leq j < \nu_0$ rows are replaced in this process, the untouched $n - k$ rows of M_0 will be linearly dependent, implying $\alpha_j = 0$ for $j < \nu_0$, and thus $\nu(\mathsf{M}(\omega_0, \beta_0)) \leq \nu(\beta_0)$. □

4.5 Numerical Techniques

The location of the propagation constants in the complex plane, as found with the argument principle, is refined using an adaptive quadrature scheme with adjustable accuracy. The tracking of a propagation constant as a function of frequency is eased by considering the derived theorems.

4.5.1 Argument Principle

As a first coarse estimate of the distribution of the propagation constants for a fixed angular frequency ω, we use Cauchy's argument principle (as in [23]). The regions where propagation constants are likely to be found are meshed into rectangular boxes that contain no branch cuts. The argument principle can then be used to determine the number of zeros of the determinant function, counted with their multiplicity, inside a rectangular box R in the β-plane with the sole knowledge of the function values on the boundary. Indeed, if $R \subset (\mathbb{C} \setminus \cup_i \mathcal{B}_i(\omega))$ (no branch cuts through R) and $\mathfrak{D}(\omega, \beta) \neq 0$ for $\beta \in \partial R$ (no zero on the boundary), then the determinant function has the following number of zeros inside R, where the contour integral is taken in counterclockwise direction:

$$n_R = \frac{1}{2\pi j} \oint_{\partial R^+} \frac{\partial_\beta \mathfrak{D}(\omega, \beta)}{\mathfrak{D}(\omega, \beta)} d\beta. \tag{4.16}$$

The winding number n_R of the determinant function along ∂R and is equal to the number of times the curve $\{\mathfrak{D}(\omega, \beta) \mid \beta \in \partial R\}$ circles around the origin. This last quantity can be easily calculated numerically by inspecting the change in argument of the determinant function between neighboring sample points on the boundary [24].

4.5.2 Adaptive Quadrature Scheme

A more accurate estimate of the distribution of the propagation constants can be obtained by subsequently refining boxes with $n_R > 0$ and applying the argument principle. However, this approach becomes infeasible if one wants to know the location of the zeros up to a fixed (and high) accuracy. To solve this issue, the coarse search with the argument principle is followed by a refinement step, consisting of numerically evaluating the following integral:

$$\overline{z} = \frac{1}{2\pi n_R j} \oint_{\partial R^+} \beta \frac{\partial_\beta \mathfrak{D}(\omega, \beta)}{\mathfrak{D}(\omega, \beta)} d\beta. \tag{4.17}$$

If there is only one zero with multiplicity n_R inside R, then $\overline{z}$ precisely represents the location of this zero. Otherwise, $\overline{z}$ represents the *center of mass* of the enclosed zeros, weighted with their multiplicities. A sufficient refinement of the boxes via the argument principle is able to exclude the latter case.

We have implemented a numerical quadrature scheme, capable of evaluating (4.17) to a given precision of the real and imaginary part, taking into account the rather high cost of evaluating the determinant function in a point. These considerations lead to a Gauss-Kronrod quadrature rule, as the addition of $N + 1$ Kronrod nodes to the N Gauss-Legendre nodes in order to estimate the error of the original Gauss-Legendre rule, allows to reuse the function values at the Gauss-Legendre nodes.

In this way, the integral in (4.17) is split up into four parts, with each one corresponding to a segment of ∂R. The integrand of such a segment integral is smooth (by theorem 4.3.4) and the derivative $\partial_\beta \mathfrak{D}(\omega, \beta)$ at the $2N + 1$ quadrature points is numerically estimated by a linear transformation of the determinant values at the nodes, which is essentially a projector of the function values at the quadrature nodes onto a set of orthogonal polynomials, followed by a derivative operator of the polynomials at the same nodes. If the error of the segment integral is too high to guarantee the accuracy of the end result, the segment is divided into two equal segments where the same procedure is performed [25]. The quadrature scheme can thus be classified as an adaptive Gauss-Kronrod scheme.

4.5.3 Frequency sweep

The numerical procedure of tracking the dispersion curve of a propagation constant as a function of frequency is greatly facilitated by the use of previously

derived theorems. At the start of the frequency sweep, we choose a fixed mesh along the material boundaries that is fine enough to accurately represent the boundary and electromagnetic wave behavior at the considered frequencies and longitudinal wavenumbers. In this way, the curve $\beta(\omega)$ we are looking for, starting from a seed value β_0 at ω_0, will be smooth as a function of frequency (by theorem 4.4.1). This allows the use of an extrapolation method to accurately estimate the location of the propagation constant at the next frequency point. This prediction will then be refined by using the adaptive quadrature scheme, discussed in the previous paragraph.

The property that the winding number of the curve $\beta(\omega)$ stays constant, as a consequence of theorem 4.4.1 (unless two curves cross or a branch cut is met), is used to check if the box around the estimation contains no extra propagation constants. If the box around the estimated propagation constant at the next frequency point is chosen too large, such that another zero of the determinant lies inside it, formula (4.17) will give the center of mass of the enclosed zeros, and not the sought value. However, this case can be detected as the winding number increases, which signals the numerical procedure to reduce the box.

4.5.4 Calculation of the Cross-sectional Eigenmode Profiles

The cross-sectional eigenmode profiles, i.e., the electric and magnetic field distribution of the eigenmodes corresponding to a propagation constant β_0 at the frequency ω_0, are calculated from the tangential boundary fields using representation formulas. The eigenvectors in the null space of $\mathsf{M}(\omega_0, \beta_0)$ are the expansion coefficients of the tangential traces of the eigenmodes on the material boundaries. The number of linearly independent eigenvectors is upper bounded by $\nu(\beta_0)$ (Theorem 4.4.3).

4.6 Examples

4.6.1 Complex Modes in a Shielded Dielectric Image Guide

In this example, the presented boundary element method is employed to numerically determine the dispersion curves of complex modes. These modes can arise in certain inhomogeneous waveguides, and have propagation constants with non-zero real and imaginary part, even if all material regions in the cross section are lossless. Consider the shielded dielectric image guide of Figure 4.4, which is essentially a rectangular waveguide loaded with a dielectric material region with relative permittivity $\epsilon_r = 9$, located at the bottom conductor.

It is well-known that complex modes can exist in this type of waveguide [7]. If the shielding conductor Ω_c is a perfect electric conductor (PEC), there are no losses inside the structure, which is reflected by the fact that complex modes exist in pairs with conjugate propagation constants [22], [26]. In the lossless

case, the complex conjugate symmetry of the propagation constants of the mode pair is nicely predicted by the numerical framework (see theorem 4.3.5). If the dielectric load material is lossy, the propagation constants are no longer each other's complex conjugate [7]. We will show that the same applies for the case with non-perfectly conducting waveguide walls and lossless dielectric load material.

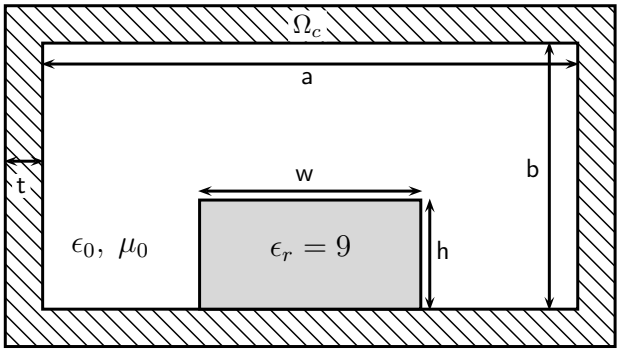

Figure 4.4: Cross section of a shielded dielectric image guide

To illustrate the applicability of the boundary element method to a highly conductive region, consider a non-perfect shielding conductor Ω_c with electric conductivity σ and thickness $t = 1$ mm. In the numerical examples, we study the effect of the conductivity by choosing two distinct values $\sigma_a = 5.8e7$ S/m (copper) and $\sigma_b = 10^{-4}\sigma_a$. We use the same geometry as in [7], i.e., $a = 2b = 15.798$ mm, $w = 6.9$ mm and $h = 3.2$ mm. Figures 4.5 and 4.6 show the normalized real and absolute value of the normalized imaginary part of two propagation constant curves, termed $\beta_1(f)$ and $\beta_2(f)$, for the two conductivities, with the frequency $f = \omega/2\pi$ varying between 12 GHz and 15 GHz.

In the waveguide with PEC boundary, a true bifurcation of the complex modes occurs around $f_b = 14.5$ GHz, and the modes are exactly each other's complex conjugate before the bifurcation, i.e., $\beta_1(f) = \overline{\beta_2(f)}$ if $f < f_b$ [7]. At first glance, the bifurcation for a lossless waveguide with PEC boundary seems to be in contradiction with corollary 4.4.2. However, this bifurcation happens on the branch cuts of the transversal wavenumbers of both lossless material regions (free space and the dielectric load material), i.e., on the real axis in the complex β-plane around $0.4k_0$, and theorem 4.4.1 only holds for $(\omega_0, \beta_0) \in \mathcal{O}$, i.e., outside the branch cuts $\mathcal{B}_i(\omega)$.

For the considered case of a lossy shielding conductor, the bifurcation disappears and the two modes are no longer conjugate (Fig. 4.5 and 4.6). It was verified that by increasing the conductivity of the shielding conductor, the dispersion curve $\beta_1(f)$ converges to $\overline{\beta_2(f)}$ for $f < f_b$. This can be expected, as a PEC

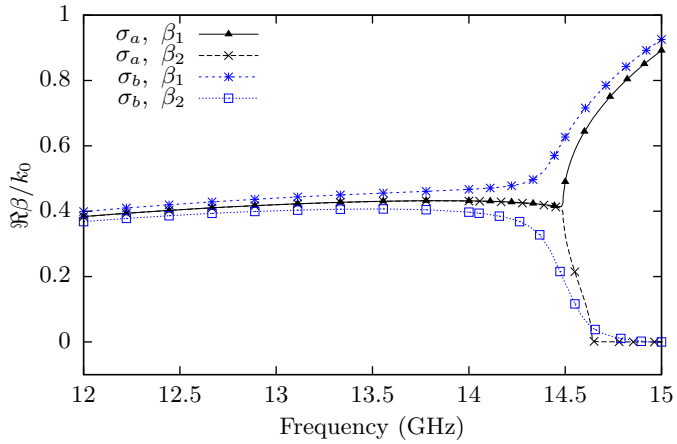

Figure 4.5: Real part of the normalized dispersion curves for different conductivities

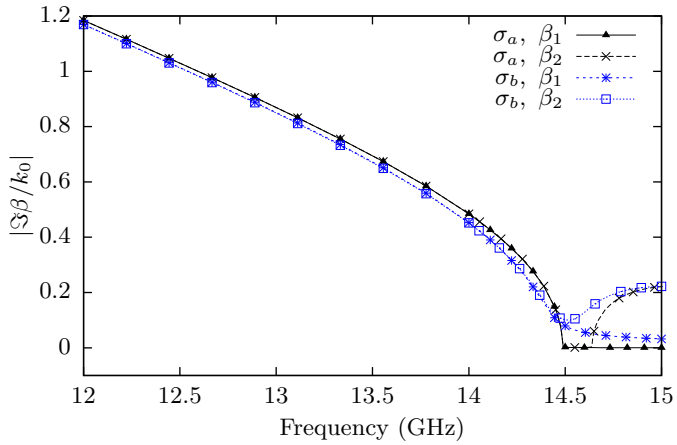

Figure 4.6: Absolute value of the imaginary part of the normalized dispersion curves for different conductivities

boundary corresponds to the case $\sigma \to \infty$. As the curves $\beta_1(f)$ and $\beta_2(f)$ do not cross a branch cut, and because they cannot cross each other (both lie on the opposite side of the branch cuts), no bifurcation is allowed (corollary 4.4.2). Moreover, their curves in the complex plane are smooth, but this is not really apparent from Figures 4.5 and 4.6. However, Figures 4.7 and 4.8 clearly demonstrate this fact, by showing the logarithm of the real part and the absolute value of the normalized imaginary part of both curves.

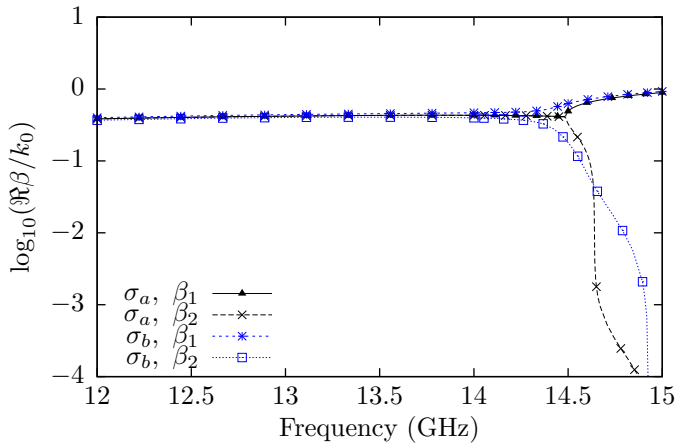

Figure 4.7: Logarithm of the real part of the normalized dispersion curves for different conductivities

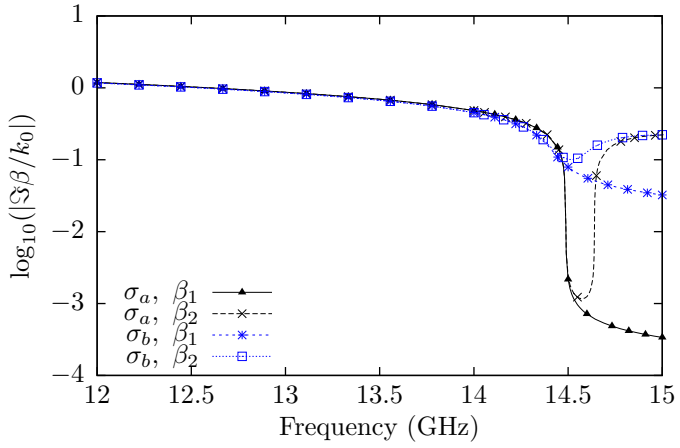

Figure 4.8: Logarithm of the absolute value of the imaginary part of the normalized dispersion curves for different conductivities

4.6.2 Coupled Microstrip Lines on a Finite Substrate

The presented method allows an efficient eigenmode analysis of a pair of coupled microstrip lines on a finite substrate and ground conductor (inset of Fig. 4.9). The two microstrip lines and the ground conductor have electric conductivity $\sigma = 5.8 \cdot 10^7\ (\Omega\mathrm{m})^{-1}$, the substrate has relative permittivity $\epsilon_r = 9.8$ and the background medium is free space. The dimensions of the waveguide are given by $d = 1$ mm, $w = d/0.635$, $t = 0.3w$ and $h = w$.

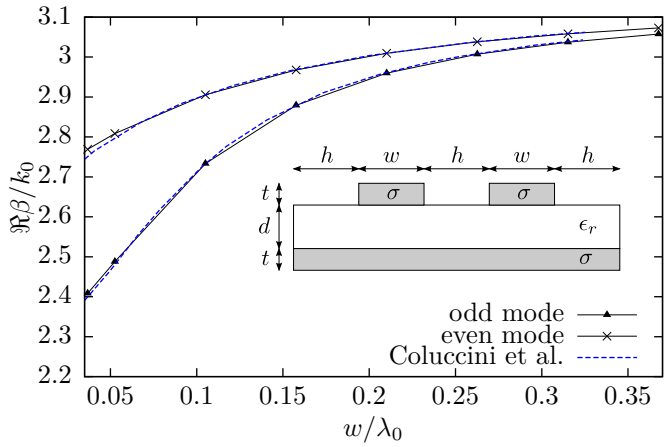

Figure 4.9: Real part of the dispersion curves of the fundamental modes of the two coupled microstrip lines sketched in the inset. $d = 1$ mm, $w = d/0.635$, $t = 0.3w$, $h = w$, $\epsilon_r = 9.8$ and $\sigma = 5.8 \cdot 10^7$ $(\Omega\text{m})^{-1}$. Symbols: this method with copper conductors and finite substrate, dashed lines: Coluccini et al. [27] with perfect conductors and infinite substrate.

Fig. 4.9 shows the real part of the propagation constant of the two fundamental modes, normalized to the free space wave number $k_0 = \omega\sqrt{\epsilon_0\mu_0}$, as a function of $w/\lambda_0 = wf/c$, with c the speed of light in vacuo and f varying between 7 GHz and 70 GHz. At high frequencies, the curves coincide with published results for the microstrip pair with perfect conductors and infinite substrate and ground plane [27]. The electric and magnetic field of the eigenmodes at high frequencies (Fig. 4.11 and 4.12) are mostly confined in the substrate region directly below the microstrip lines, so that the finity of the substrate has no major influence on the propagation constants.

The imaginary part of the propagation constant of the two fundamental modes is shown in Fig. 4.10, and represents the waveguide losses that are caused by the finite conductivity of the conductors. For a waveguide of length l, the power loss of a propagating eigenmode is equal to $1 - e^{2l\Im\beta}$. Observe that the power loss increases with frequency, which is caused by two phenomena. First, the thickness of the skin effect layer in the conductors decreases with frequency, which increases the resistance per unit length ($\sqrt{f}$ behavior). Second, at higher frequencies, the current in the microstrip lines is mostly flowing on the bottom edge and is less spread over the conductor boundary than at lower frequencies (this can be observed from the magnetic field distribution in Fig. 4.12), which further increases losses.

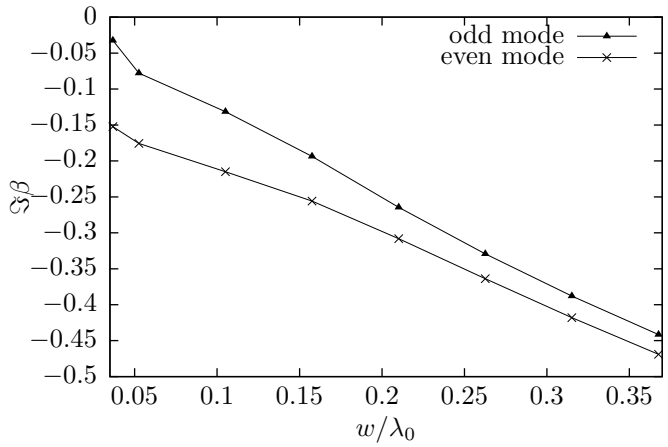

Figure 4.10: Imaginary part of the dispersion curves of the fundamental modes of the two coupled microstrip lines.

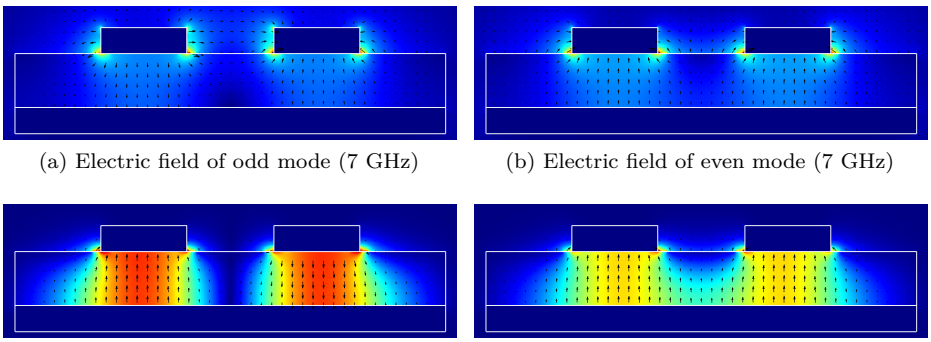

(a) Electric field of odd mode (7 GHz)

(b) Electric field of even mode (7 GHz)

(c) Electric field of odd mode (70 GHz)

(d) Electric field of even mode (70 GHz)

Figure 4.11: Cross-sectional tangential electric field distribution (normalized) of the two fundamental modes of the coupled microstrip lines at the frequencies 7 GHz ($w/\lambda_0 \approx 0.037$) and 70 GHz ($w/\lambda_0 \approx 0.37$).

4.7 Conclusions

Theorems were presented stating some properties of the dispersion curves for general isotropic piecewise homogeneous waveguides. These theorems were leveraged in a numerical implementation of a set of boundary integral equations to determine the waveguide eigenmodes and their propagation constants. These boundary integral equations can handle highly conductive materials (such as copper).

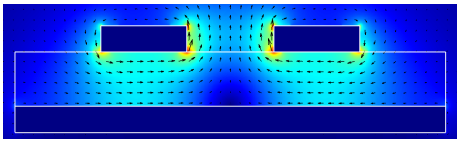

(a) Magnetic field of odd mode (7 GHz)

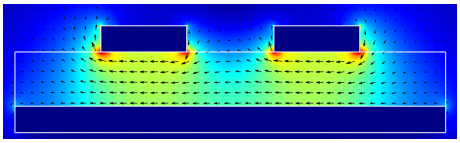

(b) Magnetic field of even mode (7 GHz)

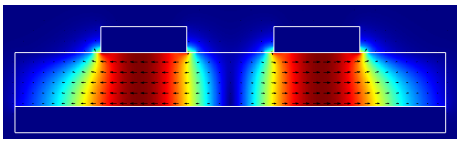

(c) Magnetic field of odd mode (70 GHz)

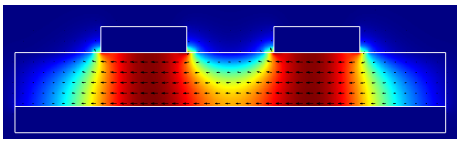

(d) Magnetic field of even mode (70 GHz)

Figure 4.12: Cross-sectional tangential magnetic field distribution (normalized) of the two fundamental modes of the coupled microstrip lines at the frequencies 7 GHz ($w/\lambda_0 \approx 0.037$) and 70 GHz ($w/\lambda_0 \approx 0.37$).

Challenging numerical examples demonstrate the possibilities of our tool. To the best of our knowledge, this is the first time that the effect of a lossy shielding conductor on the complex modes of a shielded dielectric image guide has been numerically investigated.

References

[1] D. Dobbelaere, H. Rogier, and D. De Zutter, "Properties and numerical solutions of dispersion curves in general isotropic waveguides", *IEEE Transactions on Microwave Theory and Techniques*, vol. 61, no. 9, pp. 3161–3168, 2013.

[2] D. Dobbelaere, H. Rogier, and D. De Zutter, "Analytic properties of dispersion curves for efficient eigenmode analysis of isotropic waveguides using a boundary element method", in *Proceedings of the IEEE International Conference on Numerical Electromagnetic Modeling and Optimization for RF, Microwave, and Terahertz Applications*, Pavia, Italy: IEEE, 2014, pp. 1–4.

[3] W. McLevige, T. Itoh, and R. Mittra, "New waveguide structures for millimeter-wave and optical integrated circuits", *Microwave Theory and Techniques, IEEE Transactions on*, vol. 23, no. 10, pp. 788 –794, Oct. 1975.

[4] R. Mittra, Y.-L. Hou, and V. Jamnejad, "Analysis of open dielectric waveguides using mode-matching technique and variational methods", *Microwave Theory and Techniques, IEEE Transactions on*, vol. 28, no. 1, pp. 36 –43, Jan. 1980.

[5] J. Strube and F. Arndt, "Rigorous hybrid-mode analysis of the transition from rectangular waveguide to shielded dielectric image guide", *Microwave Theory and Techniques, IEEE Transactions on*, vol. 33, no. 5, pp. 391 –401, May 1985.

[6] K. Bierwirth, N. Schulz, and F. Arndt, "Finite-difference analysis of rectangular dielectric waveguide structures", *Microwave Theory and Techniques, IEEE Transactions on*, vol. 34, no. 11, pp. 1104 –1114, Nov. 1986.

[7] F. Fernandez, Y. Lu, J. Davies, and S. Zhu, "Finite element analysis of complex modes in inhomogeneous waveguides", *Magnetics, IEEE Transactions on*, vol. 29, no. 2, pp. 1601 –1604, Mar. 1993.

[8] J. Bagby, D. Nyquist, and B. Drachman, "Integral formulation for analysis of integrated dielectric waveguides", *Microwave Theory and Techniques, IEEE Transactions on*, vol. 33, no. 10, pp. 906 –915, Oct. 1985.

[9] J.-F. Kiang, S. Ali, and J. Kong, "Integral equation solution to the guidance and leakage properties of coupled dielectric strip waveguides", *Microwave Theory and Techniques, IEEE Transactions on*, vol. 38, no. 2, pp. 193 –203, Feb. 1990.

[10] F. Olyslager, D. De Zutter, and K. Blomme, "Rigorous analysis of the propagation characteristics of general lossless and lossy multiconductor transmission lines in multilayered media", *Microwave Theory and Techniques, IEEE Transactions on*, vol. 41, no. 1, pp. 79 –88, Jan. 1993.

[11] F. Olyslager and D. De Zutter, "Rigorous boundary integral equation solution for general isotropic and uniaxial anisotropic dielectric waveguides in multilayered media including losses, gain and leakage", *Microwave Theory and Techniques, IEEE Transactions on*, vol. 41, no. 8, pp. 1385 –1392, Aug. 1993.

[12] A. Yakovlev and G. Hanson, "Fundamental modal phenomena on isotropic and anisotropic planar slab dielectric waveguides", *Antennas and Propagation, IEEE Transactions on*, vol. 51, no. 4, pp. 888–897, 2003.

[13] A. Yakovlev and G. Hanson, "Analysis of mode coupling on guided-wave structures using morse critical points", *Microwave Theory and Techniques, IEEE Transactions on*, vol. 46, no. 7, pp. 966–974, 1998.

[14] A. Poggio and E. Miller, "Integral equation solution of three-dimensional scattering problems", in *Computer Techniques for Electromagnetics*, R. Mittra, Ed., Pergamon Press, 1973, ch. 4.

[15] Y. Chang and R. Harrington, "A surface formulation for characteristic modes of material bodies", *Antennas and Propagation, IEEE Transactions on*, vol. 25, no. 6, pp. 789 –795, Nov. 1977.

[16] T. Wu and L. Tsai, "Scattering from arbitrarily-shaped lossy dielectric bodies of revolution", *Radio Science*, pp. 709–718, Sep. 1977.

[17] J. Fostier, B. Michiels, I. Bogaert, and D. D. Zutter, "A Fast 2D Parallel MLFMA Solver for Oblique Plane Wave Incidence", *Radio Science*, Nov. 2011.

[18] F. Olyslager, *Electromagnetic Waveguides and Transmission Lines*. Oxford University Press, 1999, vol. 51, Oxford Engineering Science Series.

[19] T. Nishino, *Function Theory in Several Complex Variables*. American Mathematical Society, 2001, Translations of Mathematical Monographs.

[20] F. W. Olver, D. W. Lozier, R. F. Boisvert, and C. W. Clark, *NIST Handbook of Mathematical Functions*. New York, NY, USA: Cambridge University Press, 2010.

[21] L. Hörmander, *An introduction to complex analysis in several variables*. North-Holland, 1990, North-Holland mathematical library.

[22] R. Islam and G. Eleftheriades, "On the independence of the excitation of complex modes in isotropic structures", *Antennas and Propagation, IEEE Transactions on*, vol. 58, no. 5, pp. 1567–1578, 2010.

[23] R. Smith, S. N. Houde-Walter, and G. W. Forbes, "Mode determination for planar waveguide using the four-sheeted dispersion relation", *Quantum Electronics, IEEE Journal of*, vol. 28, no. 6, pp. 1520–1526, 1992.

[24] P. Henrici, *Applied and Computational Complex Analysis*. Wiley, 1988, Wiley Classics Library.

[25] W. Press, S. Teukolsky, W. Vetterling, and B. Flannery, *Numerical Recipes 3rd Edition: The Art of Scientific Computing*. Cambridge University Press, 2007, Numerical Recipes: The Art of Scientific Computing.

[26] J. Rhodes, "General constraints on propagation characteristics of electromagnetic waves in uniform inhomogeneous waveguides", *Electrical Engineers, Proceedings of the Institution of*, vol. 118, no. 7, pp. 849 –856, Jul. 1971.

[27] G. Coluccini, M. Lucido, and G. Panariello, "Spectral domain analysis of open single and coupled microstrip lines with polygonal cross-section in bound and leaky regimes", *Microwave Theory and Techniques, IEEE Transactions on*, vol. 61, no. 2, pp. 736–745, 2013.

Part II

Preconditioning Techniques

5 Introduction

★ ★ ★

We briefly recall the main results that lead to a Calderón multiplicative preconditioner for the electric field integral equation (EFIE), based on a family of basis functions that are dual to the Rao-Wilton-Glisson (RWG) functions. The final cornerstone was provided by Buffa and Christiansen in [1], with the introduction of so-called Buffa-Christiansen (BC) functions. Arguably, the first paper that diffused these findings to the engineering community is [2].

5.1 A Calderón multiplicative preconditioner for the electric field integral equation

Denote $V = \mathbf{H}^{-\frac{1}{2}}(\mathsf{div}_\Gamma, \Gamma)$ the Sobolev space of tangential current densities on the boundary Γ of a Lipschitz domain $\Omega \subset \mathbb{R}^3$, with norm $\|.\|_V$ and dual space $W = \mathbf{H}^{-\frac{1}{2}}(\mathsf{curl}_\Gamma, \Gamma)$ (with $\mathbf{L}^2(\Gamma)$ as pivot space [3]).

The solution of a scattering problem at a perfect electric conducting domain Ω with outward unit normal vector $\hat{\mathbf{n}}$ can be obtained with the *electric field integral equation* (EFIE)*, i.e., find $\mathbf{j} \in V$ such that

$$a(\boldsymbol{\lambda}, \mathbf{j}) \triangleq \langle \boldsymbol{\lambda}, \hat{\mathbf{n}} \times \mathcal{T}_k \mathbf{j} \rangle = -\langle \boldsymbol{\lambda}, \hat{\mathbf{n}} \times \mathbf{e}^{(i)} \rangle \qquad \forall \boldsymbol{\lambda} \in V, \tag{5.1}$$

*at least, in absence of resonances, i.e., if the squared wavenumber k^2 does not belong to the denumerable set of interior electric Maxwell eigenvalues [4]

with $\hat{\mathbf{n}} \times \mathbf{e}^{(i)} \in V$ the (rotated) tangential incident electric field, $\mathcal{T}_k$ defined in (1.25), and $\langle ., . \rangle$ the duality pairing of V and W [4]. As $\mathcal{T}_k$ is continuous in V [4], the sesquilinear form a is continuous too.

Let $R_h \subset V$ and $B_h \subset V$ be finite-dimensional subspaces of Rao-Wilton-Glisson [5] (RWG) and Buffa-Christiansen [1] (BC) basis functions, respectively, depending on a mesh density parameter h, and with $\dim R_h = \dim B_h$. Under some regularity assumptions on the family of meshes, it can be shown that the bilinear form $d : R_h \times B_h \to \mathbb{C} : (\mathbf{r}_h, \mathbf{b}_h) \mapsto \int_\Gamma \mathbf{r}_h \cdot (\hat{\mathbf{n}} \times \mathbf{b}_h)\, \mathrm{d}S$ is continuous and satisfies the inf-sup condition (5.2), with $c_d > 0$ independent of h [1].

$$\inf_{\mathbf{r}_h \in R_h} \sup_{\mathbf{b}_h \in B_h} \frac{|d(\mathbf{r}_h, \mathbf{b}_h)|}{\|\mathbf{r}_h\|_V \|\mathbf{b}_h\|_V} \geq c_d \tag{5.2}$$

Moreover, under the same regularity assumptions of the meshes, it can be shown that the two discrete inf-sup conditions (5.3)–(5.4) hold, with $c_1, c_2 > 0$ independent of h [1].

$$\inf_{\mathbf{r}_h \in R_h} \sup_{\tilde{\mathbf{r}}_h \in R_h} \frac{|a(\mathbf{r}_h, \tilde{\mathbf{r}}_h)|}{\|\mathbf{r}_h\|_V \|\tilde{\mathbf{r}}_h\|_V} \geq c_1 \tag{5.3}$$

$$\inf_{\mathbf{b}_h \in B_h} \sup_{\tilde{\mathbf{b}}_h \in B_h} \frac{|a(\mathbf{b}_h, \tilde{\mathbf{b}}_h)|}{\|\mathbf{b}_h\|_V \|\tilde{\mathbf{b}}_h\|_V} \geq c_2 \tag{5.4}$$

After picking bases $\{\mathbf{r}_h^1, \mathbf{r}_h^2, ..., \mathbf{r}_h^n\}$ and $\{\mathbf{b}_h^1, \mathbf{b}_h^2, ..., \mathbf{b}_h^n\}$ in R_h and B_h, respectively, with $n = \dim R_h = \dim B_h$, we define the Galerkin discretizations of a w.r.t. these bases as $\mathsf{T}, \mathsf{T}_{\mathsf{bc}} \in \mathbb{C}^{n \times n}$, defined in (5.5)–(5.6).

$$(\mathsf{T})_{ij} \triangleq a(\mathbf{r}_h^i, \mathbf{r}_h^j) \tag{5.5}$$

$$(\mathsf{T}_{\mathsf{bc}})_{ij} \triangleq a(\mathbf{b}_h^i, \mathbf{b}_h^j) \tag{5.6}$$

Moreover, define the so-called mixed Gram matrix $\mathsf{G} \in \mathbb{C}^{n \times n}$ with

$$(\mathsf{G})_{ij} \triangleq d(\mathbf{r}_h^i, \mathbf{b}_h^j). \tag{5.7}$$

It follows from [6, Theorem 2.1] and [7, §1.2.2] that

$$\kappa(\mathsf{G}^{-T} \mathsf{T}_{\mathsf{bc}} \mathsf{G}^{-1} \mathsf{T}) \leq \frac{\|a\|^2 \|d\|^2}{c_1 c_2 c_d^2}, \tag{5.8}$$

with $\kappa(.)$ the *spectral* condition number of a square matrix. Although the condition number of T diverges for $h \to 0$ (i.e., for an increasing number of basis functions n), as shown numerically in [2], $\kappa(\mathsf{G}^{-T} \mathsf{T}_{\mathsf{bc}} \mathsf{G}^{-1} \mathsf{T})$ is bounded independently of h (for h small enough). We call $\mathsf{G}^{-T} \mathsf{T}_{\mathsf{bc}} \mathsf{G}^{-1}$ (or $\mathsf{T}_{\mathsf{bc}} \mathsf{G}^{-1}$, as G is well-conditioned) a Calderón multiplicative preconditioner for the Galerkin discretization T of the electric field integral operator $\mathcal{T}_k$.

References

[1] A. Buffa and S. H. Christiansen, "A dual finite element complex on the barycentric refinement", *Comptes Rendus Mathematique*, vol. 340, no. 6, pp. 461–464, 2005.

[2] F. Andriulli, K. Cools, H. Bagci, F. Olyslager, A. Buffa, S. Christiansen, and E. Michielssen, "A multiplicative Calderon preconditioner for the electric field integral equation", *Antennas and Propagation, IEEE Transactions on*, vol. 56, no. 8, pp. 2398–2412, 2008.

[3] M. Cessenat, *Mathematical Methods in Electromagnetism: Linear Theory and Applications*. World Scientific, 1996, Series on Advances in Mathematics for Applied Sciences.

[4] A. Buffa and R. Hiptmair, "Galerkin boundary element methods for electromagnetic scattering", in *Topics in Computational Wave Propagation*, M. Ainsworth, P. Davies, D. Duncan, B. Rynne, and P. Martin, Eds., vol. 31, Lecture Notes in Computational Science and Engineering, Springer Berlin Heidelberg, 2003, pp. 83–124.

[5] S. Rao, D. Wilton, and A. Glisson, "Electromagnetic scattering by surfaces of arbitrary shape", *Antennas and Propagation, IEEE Transactions on*, vol. 30, no. 3, pp. 409–418, 1982.

[6] R. Hiptmair, "Operator preconditioning", *Comput. Math. Appl.*, vol. 52, no. 5, pp. 699–706, Sep. 2006.

[7] S. H. Christiansen, "Résolution des équations intégrales pour la diffraction d'ondes acoustiques et électromagnétiques - Stabilisation d'algorithmes itératifs et aspects de l'analyse numérique", PhD thesis, Ecole Polytechnique, Jan. 2002.

6

A Calderón Multiplicative Preconditioner for the Poincaré-Steklov Operator of a Heterogeneous Domain

based on the contribution [1]

★ ★ ★

We prove that the Poincaré-Steklov operator acting on traces of solutions to the time-harmonic Maxwell equations in a heterogeneous domain with a smooth boundary is regularized by a well-known boundary integral operator related to the homogeneous exterior domain. This property allows us to simultaneously construct a Calderón multiplicative preconditioner for the discretized operator and for a 3-D hybrid finite/boundary element method formulation. Numerical examples demonstrate the effectiveness of the preconditioner, even for heterogeneous domains with non-smooth boundaries.

6.1 Introduction

A Poincaré-Steklov operator (PS for short), also called Dirichlet-to-Neumann operator, embodies a connection between the boundary values and (a function of) their derivatives of solutions to a boundary value problem of a linear partial differential operator. PS operators and their discretizations are present in continuous and discrete formulations of a wide spectrum of equations in

computational physics, including heat problems, fluid dynamics [2], structural mechanics, acoustics and electromagnetics [3]–[5]. They naturally allow to impose field continuity constraints at the interface between physical domains and are consequently found in domain decomposition methods of finite element methods [6]–[8] and in hybrid finite/boundary element method (FEM-BEM) formulations [3], [4], [9]. For differential operators acting on scalar fields, for example the Helmholtz operator $\Delta + k^2$, the PS operator maps the scalar boundary value of a solution onto its normal derivative [10]. In this chapter, we focus on the vectorial time-harmonic electromagnetic PS operator mapping the tangential boundary value of the electric field $\mathbf{e}$, which satisfies the *heterogeneous* vector Helmholtz equation $\nabla \times \nabla \times \mathbf{e} + k^2(x, y, z)\mathbf{e} = 0$ in the interior domain, onto the corresponding tangential component of the magnetic field trace [5], [11].

The presence of ill-conditioned discretized PS operators in numerical formulations severely increases the number of iterations and hampers the convergence speed of Krylov iterative methods. This has incited the development of preconditioners in past research, of which we intend to give a few examples. The Neumann-Neumann and Interface Strip preconditioner have been proposed for the global PS operator in domain decomposition methods [2], [12]. Moreover, we note that the application of a Calderón preconditioner for the Poincaré-Steklov operator of the 2-D scalar heterogeneous Helmholtz equation on a structured square domain has been investigated in [13].

In this chapter, we propose a Calderón multiplicative preconditioner for the finite element Schur complement discretization of the PS operator, denoted $\mathcal{P}$, for the vector *heterogeneous* Helmholtz equation on a general 3-D domain. First, we prove a decomposition of $\mathcal{P}$ in terms of well-known boundary integral operators. Then, we show that $\mathcal{P}$ is regularized by the so-called electric field integral operator $\mathcal{T}_k$, further defined in (6.10), meaning that their product can be written as a compact perturbation of a well-conditioned operator. The self-regularizing property of $\mathcal{T}_k$ itself, i.e., the fact that $\mathcal{T}_k^2$ is a compact perturbation of the identity operator (up to a constant multiplicative factor) on domains with smooth boundaries, was the source of inspiration for efficient preconditioners in BEMs for various integral equations, such as the electric field integral equation (EFIE) [14], [15], the combined field integral equation (CFIE) [16], the regularized combined field integral equations (CFIER) of [17], a single source CFIE for dielectric scattering [18], the Poggio-Miller-Chan-Harrington-Wu-Tsai (PMCHWT) equation [19], an electric current formulation [20] and the EFIE in a layered medium [21]. We emphasize that the cited BEMs are restricted to piecewise homogeneous scatterers, and are not applicable to general heterogeneous domains. The multiplicative nature of the preconditioners in [15], [16], [18]–[20] and the specific choice for Buffa-Christiansen (BC) basis functions [22], for the discretization of the $\mathcal{T}_k$ operator appearing in the preconditioner, has the benefit that existing method of moments (MoM) algorithms for Rao-Wilton-Glisson (RWG) functions [23] can still be used, albeit on the barycentrically

refined mesh.

A wide class of preconditioners for hybrid FEM-BEM formulations exists [24]–[28], with an important subset of them relying on domain decomposition methods [29], [30]. For the first time, a Calderón multiplicative preconditioner is applied to a novel reduced hybrid FEM-BEM formulation for electromagnetic scattering at a heterogeneous obstacle, and is compatible with existing matrix vector product acceleration schemes, such as the multilevel fast multipole algorithm (MLFMA) [31]–[34].

This chapter is structured as follows: in section 6.2 we introduce the electromagnetic Poincaré-Steklov operator $\mathcal{P}$ of a heterogeneous domain and derive a decomposition in terms of $\mathcal{T}_k$, which implies that $\mathcal{T}_k$ regularizes $\mathcal{P}$, in a Sobolev space framework. Inspired by these properties, we construct a Calderón multiplicative preconditioner (CMP) for a Schur complement finite element discretization of $\mathcal{P}$ and investigate its effect on the singular value distribution of the discretized PS operator in section 6.3. We present a novel hybrid FEM-BEM formulation, whose reduced form is amenable to the CMP, in section 6.4, and demonstrate the effectiveness of the preconditioner in the numerical examples of section 6.5.

6.2 Electromagnetic Poincaré-Steklov Operator of a Heterogeneous Domain

In this section, the governing time-harmonic Maxwell equations for scattering at a bounded heterogeneous domain are introduced. We define the Poincaré-Steklov operator $\mathcal{P}$ of the heterogeneous domain and derive some of its continuous properties, for the first time, in a Sobolev space framework. An interesting corollary is the regularization of $\mathcal{P}$ by a boundary integral operator $\mathcal{T}_k$, sometimes called the electric field integral operator [35], which is frequently used in scattering at perfect electric conducting objects [15], [36], [37]. This property hints at a discrete Calderón multiplicative preconditioner for the ill-conditioned discretization of $\mathcal{P}$, which is numerically investigated in section 6.3.

6.2.1 Scattering at a Bounded Heterogeneous Domain: Maxwell's equations

Consider a connected open bounded Lipschitz (see e.g. [38] for a definition) domain $\Omega^- \subset \mathbb{R}^3$, with boundary Γ and external unit normal $\hat{\mathbf{n}}$, representing a heterogeneous isotropic region with permittivity $\epsilon_1(\mathbf{r}) \in \mathbb{C}$ and constant permeability $\mu_0 > 0$ (Fig. 6.1). The domain Ω^- is embedded in a homogeneous medium, with permittivity $\epsilon_0 > 0$ and permeability μ_0. The structure is excited by an incoming field $(\mathbf{e}^{(i)}, \mathbf{h}^{(i)})$ in the homogeneous exterior region $\Omega^+ = \mathbb{R}^3 \setminus \overline{\Omega^-}$, with $\overline{\Omega^-} = \Omega^- \cup \Gamma$ being the closure of Ω^-. The solution $(\mathbf{e}, \mathbf{h})$ satisfies Maxwell's equations (6.1)–(6.2) in the frequency domain (angular

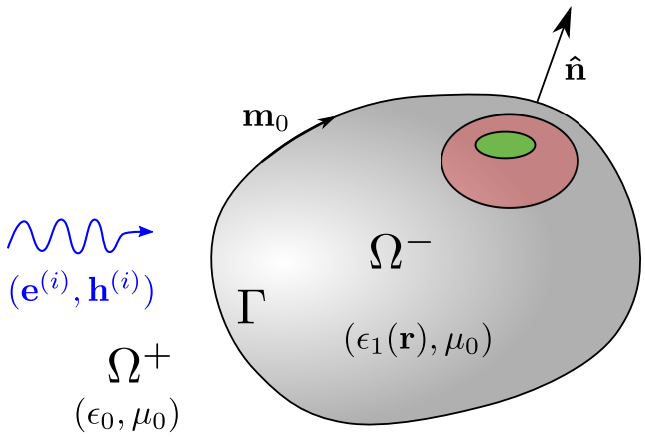

Figure 6.1: Geometry consisting of a heterogeneous domain Ω^-, embedded in a homogeneous space.

frequency ω, time factor $e^{j\omega t}$), boundary conditions (6.3) at Γ, and a suitable radiation condition (6.4) [36], [39]:

$$\nabla \times \mathbf{e} = -j\omega\mu_0\mathbf{h},\ \nabla \times \mathbf{h} = j\omega\epsilon_0\mathbf{e} \qquad (\text{in } \Omega^+), \tag{6.1}$$

$$\nabla \times \mathbf{e} = -j\omega\mu_0\mathbf{h},\ \nabla \times \mathbf{h} = j\omega\epsilon_1(\mathbf{r})\mathbf{e} \qquad (\text{in } \Omega^-), \tag{6.2}$$

$$[\hat{\mathbf{n}} \times \mathbf{e}]_\Gamma = \hat{\mathbf{n}} \times \mathbf{e}^{(i)},\ [\hat{\mathbf{n}} \times \mathbf{h}]_\Gamma = \hat{\mathbf{n}} \times \mathbf{h}^{(i)} \qquad (\text{on } \Gamma), \tag{6.3}$$

$$\lim_{|\mathbf{r}|\to\infty} \mathbf{e} \times \mathbf{r} + \eta|\mathbf{r}|\mathbf{h} = 0, \tag{6.4}$$

with $\eta = \sqrt{\mu_0/\epsilon_0}$ the characteristic impedance of the exterior medium and $[\boldsymbol{\psi}]_\Gamma = \lim_{\Omega^- \ni \mathbf{r}\to\Gamma} \boldsymbol{\psi} - \lim_{\Omega^+ \ni \mathbf{r}\to\Gamma} \boldsymbol{\psi}$, i.e., the jump of $\boldsymbol{\psi}$ across the interface Γ.

6.2.2 Function Spaces and Calderón Projectors

The precise statement and the proofs of the properties of the PS operator in §6.2.3 make use of the following Sobolev spaces (see [40], [41] for definitions):

$$\mathbf{L}^2(\Omega^-) = (L^2(\Omega^-))^3, \tag{6.5}$$

$$\mathbf{H}^s(\Omega^-) = (H^s(\Omega^-))^3, \tag{6.6}$$

$$\mathbf{H}^s(\Gamma) = \{\boldsymbol{\chi} \in (H^s(\Gamma))^3 \mid \boldsymbol{\chi} \cdot \hat{\mathbf{n}} = 0\}, \tag{6.7}$$

$$\mathbf{H}^s(\mathsf{curl}, \Omega^-) = \{\boldsymbol{\phi} \in \mathbf{H}^s(\Omega^-) \mid \nabla \times \boldsymbol{\phi} \in \mathbf{H}^s(\Omega^-)\}, \tag{6.8}$$

$$\mathbf{H}^s(\mathsf{div}_\Gamma, \Gamma) = \{\boldsymbol{\psi} \in \mathbf{H}^s(\Gamma) \mid \mathsf{div}_\Gamma \boldsymbol{\psi} \in H^s(\Gamma)\}, \tag{6.9}$$

with $H^s(\Gamma) = W^{s,2}(\Gamma)$ and $H^s(\Omega^-) = W^{s,2}(\Omega^-)$ Hilbert spaces for all $s \in \mathbb{R}$, with the convention that $s = 0$ if omitted, i.e., $H = H^0 = L^2$ the space of square integrable densities, and all derivatives considered in distributional sense.

Assume that the fields $\mathbf{e}$ and $\mathbf{h}$ belong to $\mathbf{H}(\mathsf{curl}, \Omega^-)$. The trace theorem shows that the tangential traces $\hat{\mathbf{n}}\times\mathbf{e}$ and $\hat{\mathbf{n}}\times\mathbf{h}$ in that case belong to $\mathbf{H}^{-\frac{1}{2}}(\mathsf{div}_\Gamma, \Gamma)$ [41]. Moreover, we define the following boundary integral operators* in $\mathbf{H}^{-\frac{1}{2}}(\mathsf{div}_\Gamma, \Gamma)$, related to the homogeneous exterior domain Ω^+:

$$\begin{aligned}\mathcal{T}_k : \mathbf{m} \mapsto \hat{\mathbf{n}} \times jk \int_\Gamma g(\mathbf{r}-\mathbf{r}')\mathbf{m}(\mathbf{r}')\mathrm{d}S' \\ - \hat{\mathbf{n}} \times \frac{1}{jk} \int_\Gamma \nabla g(\mathbf{r}-\mathbf{r}')\nabla' \cdot \mathbf{m}(\mathbf{r}')\mathrm{d}S',\end{aligned} \tag{6.10}$$

$$\mathcal{K}_k : \mathbf{m} \mapsto \hat{\mathbf{n}} \times \left[\nabla \times \int_\Gamma g(\mathbf{r}-\mathbf{r}')\mathbf{m}(\mathbf{r}')\mathrm{d}S'\right], \tag{6.11}$$

with $k = \omega\sqrt{\epsilon_0\mu_0}$ the exterior wavenumber and $g(\mathbf{r}-\mathbf{r}') = e^{-jk|\mathbf{r}-\mathbf{r}'|}/(4\pi|\mathbf{r}-\mathbf{r}'|)$ the outgoing fundamental solution of the scalar Helmholtz equation. Recall that, in a completely homogeneous free space $\mathbb{R}^3$, electric and magnetic surface current densities on Γ, denoted $\mathbf{j}, \mathbf{m} \in \mathbf{H}^{-\frac{1}{2}}(\mathsf{div}_\Gamma, \Gamma)$, respectively, give rise to the following field traces:

$$\lim_{\Omega^\pm \ni \mathbf{r} \to \Gamma} \begin{pmatrix} \hat{\mathbf{n}} \times \mathbf{e} \\ \hat{\mathbf{n}} \times \mathbf{h} \end{pmatrix} = \mathbb{P}^\pm \begin{pmatrix} \mathbf{m} \\ \mathbf{j} \end{pmatrix}, \ \mathbb{P}^\pm = \begin{pmatrix} \mathcal{K}_k \pm \frac{1}{2} & -\eta\mathcal{T}_k \\ \mathcal{T}_k/\eta & \mathcal{K}_k \pm \frac{1}{2} \end{pmatrix}, \tag{6.12}$$

with $\mathbb{P}^+$ and $\mathbb{P}^-$ the exterior and interior Calderón projectors, respectively [37], [41]. The projector property $(\mathbb{P}^\pm)^2 = \mathbb{P}^\pm$ immediately implies the so-called Calderón identities

$$\mathcal{T}_k\mathcal{K}_k + \mathcal{K}_k\mathcal{T}_k = 0, \tag{6.13}$$

$$\mathcal{K}_k^2 - \mathcal{T}_k^2 = \frac{1}{4}. \tag{6.14}$$

Lemma 6.2.1. *$\mathcal{K}_k$ is compact in $\mathbf{H}^{-\frac{1}{2}}(\mathsf{div}_\Gamma, \Gamma)$ on smooth Γ.*

Proof. This follows from the fact that $\mathcal{K}_k : \mathbf{H}^{-\frac{1}{2}}(\mathsf{div}_\Gamma, \Gamma) \to \mathbf{H}^{\frac{1}{2}}(\mathsf{div}_\Gamma, \Gamma)$ is continuous on smooth Γ (as proven in [41, Lemma 11]) and the compact embedding $\mathbf{H}^{\frac{1}{2}}(\mathsf{div}_\Gamma, \Gamma) \subset\subset \mathbf{H}^{-\frac{1}{2}}(\mathsf{div}_\Gamma, \Gamma)$. □

6.2.3 Definition and Properties of the Poincaré-Steklov Operator

The electromagnetic Poincaré-Steklov operator, denoted $\mathcal{P}$, is defined in this chapter† as the boundary operator that maps the tangential electric field trace $\hat{\mathbf{n}} \times \mathbf{e}|_\Gamma$ of a solution to the sourceless Maxwell equations inside Ω^- onto the corresponding tangential magnetic field trace $\hat{\mathbf{n}} \times \mathbf{h}|_\Gamma$.

*all integrals are considered in Cauchy principal value sense, i.e., as the limit for $\delta \to 0$ of the integrals over the surface $\Gamma \setminus \Gamma_\delta$, with Γ_δ the intersection of Γ with a ball with radius δ, centered around the singularity $\mathbf{r} \in \Gamma$ of the integrands [36]

†note that $\hat{\mathbf{n}} \times \mathcal{P}$ is called the Poincaré-Steklov operator in [5]

Definition 2 (Poincaré-Steklov Operator)**.** $\mathcal{P} : \mathbf{H}^{-\frac{1}{2}}(\mathsf{div}_\Gamma, \Gamma) \to \mathbf{H}^{-\frac{1}{2}}(\mathsf{div}_\Gamma, \Gamma) : \hat{\mathbf{n}} \times \mathbf{e}|_\Gamma \mapsto \hat{\mathbf{n}} \times \mathbf{h}|_\Gamma$, with

$$\nabla \times \mathbf{e} = -j\omega\mu_0\mathbf{h},\ \nabla \times \mathbf{h} = j\omega\epsilon_1\mathbf{e} \qquad (\text{in } \Omega^-). \tag{6.15}$$

In the sequel, we prove a specific decomposition of $\mathcal{P}$ (under certain restrictions on Γ and ϵ_1). This decomposition explains the dense mesh discretization breakdown of a finite-dimensional discretization of $\mathcal{P}$, denoted $\mathsf{P} \in \mathbb{C}^{n\times n}$, implying that the condition number of P grows without bound for an increasing number n of basis functions, as observed in section 6.3.

Theorem 6.2.2 (Decomposition of $\mathcal{P}$)**.** *Suppose the boundary Γ is smooth, and the permittivity $\epsilon_1 \in C^1(\mathbb{R}^3)$, with $\epsilon_1(\boldsymbol{\rho}) \neq 0\ \forall \boldsymbol{\rho} \in \mathbb{R}^3$ and $\epsilon_1|_{\Omega^+} = \epsilon_0$. Let $k > 0$ not be a resonant wavenumber of Ω^-. Then*

$$\mathcal{P} = -\frac{2}{\eta}\mathcal{T}_k(1 + \mathcal{C}),$$

with $\mathcal{C}$ compact in $\mathbf{H}^{-\frac{1}{2}}(\mathsf{div}_\Gamma, \Gamma)$.

Proof. Consider a magnetic current density $\mathbf{m} \in \mathbf{H}^{-\frac{1}{2}}(\mathsf{div}_\Gamma, \Gamma)$ that flows on Γ and generates electric and magnetic fields $\mathbf{e}$ and $\mathbf{h}$ inside Ω^-. With $\epsilon_1 = \epsilon_0(1+\widetilde{\epsilon})$, Maxwell's equations (6.15) can be written as

$$\nabla \times \mathbf{e} = -j\omega\mu_0\mathbf{h}, \tag{6.16}$$

$$\nabla \times \mathbf{h} = j\omega\epsilon_0\mathbf{e} + \mathbf{j}_c, \tag{6.17}$$

where $\mathbf{j}_c = j\omega\epsilon_0\widetilde{\epsilon}\mathbf{e}$ is the so-called contrast current. Consider the following operators:

$$\mathcal{A} : \mathbf{H}^{-\frac{1}{2}}(\mathsf{div}_\Gamma, \Gamma) \to \mathbf{H}(\mathsf{curl}, \Omega^-) : \mathbf{m} \mapsto \nabla \times \int_\Gamma g(\mathbf{r} - \mathbf{r}')\mathbf{m}(\mathbf{r}')\mathrm{d}S', \tag{6.18}$$

$$\mathcal{B} : \mathbf{H}(\mathsf{curl}, \Omega^-) \to \mathbf{H}(\mathsf{curl}, \Omega^-) : \mathbf{e} \mapsto k^2 \int_{\Omega^-} g(\mathbf{r} - \mathbf{r}')\widetilde{\epsilon}(\mathbf{r}')\mathbf{e}(\mathbf{r}')\mathrm{d}V' + \nabla \int_{\Omega^-} g(\mathbf{r} - \mathbf{r}')\frac{1}{1+\widetilde{\epsilon}}\nabla'\widetilde{\epsilon} \cdot \mathbf{e}\ \mathrm{d}V'. \tag{6.19}$$

The operator $\mathcal{A}$ maps the magnetic current density onto the electric field it generates in a homogeneous region Ω^- (with constant permittivity ϵ_0). It follows from [41, Theorem 5] that $\mathcal{A}$ is bounded. Taking the divergence of equation (6.17) shows that $\nabla \cdot [\widetilde{\epsilon}\mathbf{e}] = \frac{1}{1+\widetilde{\epsilon}}\nabla\widetilde{\epsilon} \cdot \mathbf{e}$, so that the operator $\mathcal{B}$ maps this incoming electric field onto the electric field generated by the contrast current $j\omega\epsilon_0\widetilde{\epsilon}\mathbf{e}$. The assumption $\epsilon_1 \in C^1(\mathbb{R}^3)$ implies that $|\epsilon_1|$ and $|\nabla\epsilon_1|$ are continuous on the compact set $\overline{\Omega^-}$ and, hence, by the extreme value theorem, they attain a minimum and maximum in $\overline{\Omega^-}$, implying that $|\nabla\epsilon_1| = |\nabla\widetilde{\epsilon}|$ and $|\tilde{\epsilon}|$ are bounded in Ω^-. Moreover, by the assumption that $\epsilon_1(\boldsymbol{\rho}) \neq 0\ \forall \boldsymbol{\rho} \in \mathbb{R}^3$,

the attained minimal value of $|\epsilon_1| = |\epsilon_0| \cdot |1 + \tilde{\epsilon}|$ is bigger than zero, implying that $\exists c > 0 : |1 + \widetilde{\epsilon}| \geq c$ in Ω^-. Therefore, $|\nabla\widetilde{\epsilon}/(1 + \widetilde{\epsilon})|$ is also bounded in Ω^-, implying that $\mathcal{B}$ is a weakly singular integral operator, and thus compact in $\mathbf{L}^2(\Omega^-)$. Moreover, $\nabla \times \mathcal{B}$ is also a weakly singular integral operator, and thus compact in $\mathbf{L}^2(\Omega^-)$ [42]. This implies that $\mathcal{B}$ is compact in $\mathbf{H}(\mathsf{curl}, \Omega^-)$ and that, as the heterogeneous scattering problem has a unique solution [43, section 9.2], $(1 - \mathcal{B})^{-1}$ is bounded in $\mathbf{H}(\mathsf{curl}, \Omega^-)$. In the last step, we transform the electric scattered field back to the boundary with the trace operator $\gamma_{\mathbf{t}} : \mathbf{H}(\mathsf{curl}, \Omega^-) \to \mathbf{H}^{-\frac{1}{2}}(\mathsf{div}_\Gamma, \Gamma) : \mathbf{u} \mapsto \hat{\mathbf{n}} \times \mathbf{u}|_\Gamma$. The continuity of this operator is well-established [41]. This leads to the following expression for the scattered electric field, generated by the contrast currents, for the given incoming field $\mathcal{A}\mathbf{m}$:

$$\hat{\mathbf{n}} \times \mathbf{e}_c = \gamma_{\mathbf{t}} \mathcal{B} \left(1 - \mathcal{B}\right)^{-1} \mathcal{A}\mathbf{m}, \tag{6.20}$$

with $\mathcal{Q} = \gamma_{\mathbf{t}} \mathcal{B} \left(1 - \mathcal{B}\right)^{-1} \mathcal{A}$ compact in $\mathbf{H}^{-\frac{1}{2}}(\mathsf{div}_\Gamma, \Gamma)$, as $\mathcal{B}$ is compact and $\mathcal{A}$, $(1 - \mathcal{B})^{-1}$ and $\gamma_{\mathbf{t}}$ are all bounded. The scattered magnetic field follows from the observation that the scattered field is a solution of Maxwell's equations (6.1) in Ω^+ satisfying the radiation condition (6.3). This means that its traces belong to the kernel of the interior Calderón projector $\mathbb{P}^-$ [41, Theorem 8], defined in (6.12), leading to

$$\hat{\mathbf{n}} \times \mathbf{h}_c = \frac{1}{\eta} \mathcal{T}_k \left(\mathcal{K}_k + \frac{1}{2}\right)^{-1} \mathcal{Q}\mathbf{m}. \tag{6.21}$$

To conclude, the total tangential electric and magnetic fields on the boundary (by taking the limit from the interior region Ω^-) can be written as a sum of the incoming fields, generated by $\mathbf{m}$, and scattered fields, generated by the contrast currents, as:

$$\hat{\mathbf{n}} \times \mathbf{e} = \left[\mathcal{K}_k - \frac{1}{2} + \mathcal{Q}\right] \mathbf{m}, \tag{6.22}$$

$$\hat{\mathbf{n}} \times \mathbf{h} = \left[\frac{1}{\eta} \mathcal{T}_k + \frac{1}{\eta} \mathcal{T}_k \left(\mathcal{K}_k + \frac{1}{2}\right)^{-1} \mathcal{Q}\right] \mathbf{m}. \tag{6.23}$$

This yields the following expression for the Poincaré-Steklov operator:

$$\mathcal{P} = \frac{1}{\eta} \mathcal{T}_k \left[1 + \left(\mathcal{K}_k + \frac{1}{2}\right)^{-1} \mathcal{Q}\right] \left[\mathcal{K}_k - \frac{1}{2} + \mathcal{Q}\right]^{-1}. \tag{6.24}$$

In case of a homogeneous interior domain, $\widetilde{\epsilon} = 0$ implies that $\mathcal{Q} = 0$ and (6.24) reduces to the well-known result $\mathcal{P} = \frac{1}{\eta} \mathcal{T}_k \left[\mathcal{K}_k - \frac{1}{2}\right]^{-1}$ [17].

For smooth Γ, the operator $\mathcal{K}_k$ is compact (see Lemma 6.2.1). Note that the inverses $(\mathcal{K}_k + \frac{1}{2})^{-1}$ and $(\mathcal{K}_k - \frac{1}{2} + \mathcal{Q})^{-1}$ in (6.24) exist, because we assume

that $k > 0$ is not a resonant wavenumber of the heterogeneous (permittivity ϵ_1) or homogeneous (constant permittivity ϵ_0) domain Ω^-. By the compactness of $\mathcal{K}_k$ and $\mathcal{Q}$, these inverses are also bounded. Combining the compactness of $\mathcal{Q}$ and the boundedness of $(\mathcal{K}_k + \frac{1}{2})^{-1}$ and $(\mathcal{K}_k - \frac{1}{2} + \mathcal{Q})^{-1}$ leads to the proposition. □

Corollary 6.2.3. Under the stated assumptions, $\mathcal{T}_k\mathcal{P} = \frac{1}{2\eta} + \mathcal{D}$, with $\mathcal{D}$ compact in $\mathbf{H}^{-\frac{1}{2}}(\mathsf{div}_\Gamma, \Gamma)$.

Proof. This follows directly from the decomposition of $\mathcal{P}$ in Theorem 6.2.2, together with the Calderón identity (6.14) and Lemma 6.2.1. □

Moreover, every operator $\mathcal{T}_{k'}$ (with wavenumber $k' > 0$) can be used to regularize $\mathcal{P}$, as indicated by the following corollary. It explains the successful application of the Calderón multiplicative preconditioner (6.43) to the hybrid system (6.42) for scattering at a heterogeneous domain with $\epsilon_1|_\Gamma \neq \epsilon_0$ (i.e., with a discontinuous jump of the permittivity at the boundary), as demonstrated in the examples of Section 6.5.

Corollary 6.2.4. Under the stated assumptions, $\mathcal{T}_{k'}\mathcal{P} = \frac{1}{2\eta}\left(\frac{k'}{k}\Pi_{\nabla_\Gamma} + \frac{k}{k'}\Pi_{\underrightarrow{\mathsf{curl}}_\Gamma}\right) + \mathcal{D}'$, with $\mathcal{D}'$ compact in $\mathbf{H}^{-\frac{1}{2}}(\mathsf{div}_\Gamma, \Gamma)$ $\forall k' > 0$, Π_{∇_Γ} and $\Pi_{\underrightarrow{\mathsf{curl}}_\Gamma}$ orthogonal projectors and $\Pi_{\nabla_\Gamma} + \Pi_{\underrightarrow{\mathsf{curl}}_\Gamma} = 1$ in $\mathbf{H}^{-\frac{1}{2}}(\mathsf{div}_\Gamma, \Gamma)$.

Proof. The proposition follows directly from Theorem 6.2.2 and the fact that $\mathcal{T}_{k'}\mathcal{T}_k$ is a compact perturbation of $-\frac{1}{4}\left(\frac{k'}{k}\Pi_{\nabla_\Gamma} + \frac{k}{k'}\Pi_{\underrightarrow{\mathsf{curl}}_\Gamma}\right)$ for $k' > 0$ [17], with Π_{∇_Γ} and $\Pi_{\underrightarrow{\mathsf{curl}}_\Gamma}$ the orthogonal projectors associated to the Helmholtz decomposition of $\mathbf{H}^{-\frac{1}{2}}(\mathsf{div}_\Gamma, \Gamma)$ and defined in [17]. □

6.3 Discretized Poincaré-Steklov Operator

The numerical simulation of the time-harmonic Maxwell equations (6.2) in a heterogeneous domain may typically involve the finite element method (FEM) [44], [45]. The hereafter introduced discretization of the PS operator, denoted P, originates from the Schur complement of the FEM matrix w.r.t. the boundary degrees of freedom. Its conditioning, including dense mesh discretization breakdown and the effect of the proposed Calderón multiplicative preconditioner on its singular values and condition number, stem from the derived theorems in §6.2.3 and are investigated as a function of the mesh density.

6.3.1 Finite Element Schur Complement Discretization

Consider the electric field wave equation in the heterogeneous domain (6.25), which follows directly from (6.2), and its weak formulation (6.26).

$$\nabla \times \nabla \times \mathbf{e} - \omega^2 \mu_0 \epsilon_1(\mathbf{r}) \mathbf{e} = 0 \tag{6.25}$$

$$\int_{\Omega^-} \boldsymbol{\psi} \cdot (\nabla \times \nabla \times \mathbf{e} - \omega^2 \mu_0 \epsilon_1(\mathbf{r}) \mathbf{e}) \, \mathrm{d}V = 0 \tag{6.26}$$

By a suitable Green's theorem [36], (6.26) reduces to

$$\int_{\Omega^-} ((\nabla \times \boldsymbol{\psi}) \cdot (\nabla \times \mathbf{e}) - \omega^2 \mu_0 \epsilon_1(\mathbf{r}) \boldsymbol{\psi} \cdot \mathbf{e}) \, \mathrm{d}V = \int_{\Gamma} (\hat{\mathbf{n}} \times \boldsymbol{\psi}) \cdot (\nabla \times \mathbf{e}) \, \mathrm{d}S. \tag{6.27}$$

Electric fields $\mathbf{e} \in \mathbf{H}(\mathsf{curl}, \Omega^-)$ that satisfy (6.27) $\forall \boldsymbol{\psi} \in \mathbf{H}(\mathsf{curl}, \Omega^-)$ are *exact* solutions to the Maxwell equations in the heterogeneous domain. In the finite element method, $\mathbf{e}$ and $\boldsymbol{\psi}$ are restricted to a finite-dimensional finite element space $\mathcal{V}^h \subset \mathbf{H}(\mathsf{curl}, \Omega^-)$, with $h > 0$ denoting the characteristic size of the mesh elements, i.e., we are interested in *approximate* solutions $\mathbf{e} \in \mathcal{V}^h$ such that (6.27) holds $\forall \boldsymbol{\psi} \in \mathcal{V}^h$. Let us denote the subspace of finite elements with vanishing tangential trace as $\mathcal{V}_i^h = \{\mathbf{e} \in \mathcal{V}^h : \hat{\mathbf{n}} \times \mathbf{e}|_\Gamma = 0\}$, which contains the finite elements associated to the $N_i = \dim(\mathcal{V}_i^h)$ interior degrees of freedom, and a subspace denoted $\mathcal{V}_b^h$, containing the finite elements associated to the $N_b = \dim(\mathcal{V}_b^h)$ boundary degrees of freedom and isomorphic to the quotient space $\mathcal{V}^h / \mathcal{V}_i^h$. This implies the following splitting, with $\oplus$ the direct sum:

$$\mathcal{V}^h = \mathcal{V}_i^h \oplus \mathcal{V}_b^h. \tag{6.28}$$

Denote the components of $\mathbf{e} \in \mathcal{V}^h$ as $\mathbf{e}_i \in \mathcal{V}_i^h$ and $\mathbf{e}_b \in \mathcal{V}_b^h$, with $\mathbf{e} = \mathbf{e}_i + \mathbf{e}_b$ (and, mutatis mutandis, for $\boldsymbol{\psi}$). With the bases $\{\mathbf{b}_i^j\}_{1 \le j \le N_i}$ and $\{\mathbf{b}_b^j\}_{1 \le j \le N_b}$ of characteristic functions corresponding to the degrees of freedom in $\mathcal{V}_i^h$ and $\mathcal{V}_b^h$, respectively, denote $\bar{e}_i \in \mathbb{C}^{N_i}$ such that $\mathbf{e}_i = \sum_j (\bar{e}_i)_j \mathbf{b}_i^j$ (and likewise for $\mathbf{e}_b$). This reduces (6.27), with $\mathbf{e}, \boldsymbol{\psi} \in \mathcal{V}^h$, to the following linear system:

$$\begin{pmatrix} \mathsf{A}_{ii} & \mathsf{A}_{ib} \\ \mathsf{A}_{bi} & \mathsf{A}_{bb} \end{pmatrix} \begin{pmatrix} \bar{e}_i \\ \bar{e}_b \end{pmatrix} = \begin{pmatrix} \bar{0} \\ \bar{a}_b \end{pmatrix}. \tag{6.29}$$

The elements of the sparse complex symmetric system matrix and the right hand side vector are given by

$$(\mathsf{A}_{mn})_{kl} = \int_{\Omega^-} [(\nabla \times \mathbf{b}_m^k) \cdot (\nabla \times \mathbf{b}_n^l) - \omega^2 \mu_0 \epsilon_1(\mathbf{r}) \mathbf{b}_m^k \cdot \mathbf{b}_n^l] \, \mathrm{d}V, \quad m, n \in \{i, b\}, \tag{6.30}$$

$$(\bar{a}_b)_k = \int_{\Gamma} (\hat{\mathbf{n}} \times \mathbf{b}_b^k) \cdot (\nabla \times \mathbf{e}) \, \mathrm{d}S. \tag{6.31}$$

Definition 3 (Finite Element Discretization of $\mathcal{P}$)**.** If A_{ii} is invertible (i.e., away from Dirichlet and Neumann frequencies of the heterogeneous domain), the finite element discretization of $\mathcal{P}$ is defined as

$$\mathsf{P} = \frac{1}{j\omega\mu_0}\left(\mathsf{A}_{bb} - \mathsf{A}_{bi}\mathsf{A}_{ii}^{-1}\mathsf{A}_{ib}\right). \tag{6.32}$$

This immediately implies that

$$\mathsf{P}\bar{e}_b = \frac{1}{j\omega\mu_0}\bar{a}_b. \tag{6.33}$$

Lemma 6.3.1 provides a connection between P and $\mathcal{P}$.

Lemma 6.3.1. *If $\mathbf{e} \in \mathcal{V}^h$ is an exact solution to the wave equation (6.25), then $(\mathsf{P}\bar{e}_b)_k = \int_\Gamma \mathbf{b}_b^k \cdot \mathcal{P}(\hat{\mathbf{n}} \times \mathbf{e}_b)\, \mathrm{d}S$.*

Proof. If $\mathbf{e} \in \mathcal{V}^h$ satisfies (6.25), then $\mathbf{e}$ and $\mathbf{h} = \frac{j}{\omega\mu_0}\nabla \times \mathbf{e}$ satisfy (6.15), implying that $\hat{\mathbf{n}} \times (\frac{j}{\omega\mu_0}\nabla \times \mathbf{e}) = \mathcal{P}(\hat{\mathbf{n}} \times \mathbf{e}) = \mathcal{P}(\hat{\mathbf{n}} \times \mathbf{e}_b)$. By (6.33) and (6.31) we get

$$(\mathsf{P}\bar{e}_b)_k = \frac{1}{j\omega\mu_0}(\bar{a}_b)_k = \int_\Gamma \mathbf{b}_b^k \cdot (\hat{\mathbf{n}} \times (\frac{j}{\omega\mu_0}\nabla \times \mathbf{e}))\, \mathrm{d}S. \tag{6.34}$$

□

For an exact solution $\mathbf{e}$ to the wave equation (6.25) that lies not necessarily in $\mathcal{V}^h$, it can be shown that P converges to the continuous operator $\mathcal{P}$, in the sense that

$$(\mathsf{P}\bar{e}_b)_m \underset{h\to 0}{\longrightarrow} \int_\Gamma \mathbf{b}_b^m \cdot \mathcal{P}(\hat{\mathbf{n}} \times \mathbf{e})\, \mathrm{d}S, \tag{6.35}$$

if $\Pi^h(\hat{\mathbf{n}} \times \mathbf{e}) = \sum_k (\bar{e}_b)_k (\hat{\mathbf{n}} \times \mathbf{b}_b^k)$ is an interpolation of $\hat{\mathbf{n}} \times \mathbf{e}$ onto the set of functions $\hat{\mathbf{n}} \times \mathbf{b}_b^k$ (which depend on h) with $\Pi^h(\hat{\mathbf{n}} \times \mathbf{e}) \underset{h\to 0}{\longrightarrow} \hat{\mathbf{n}} \times \mathbf{e}$, and $\underset{h\to 0}{\longrightarrow}$ denoting convergence if the mesh size goes to zero (for a family of regular meshes [41], [44]). Therefore, P can be called an approximation of a Galerkin discretization of $\mathcal{P}$ w.r.t. the boundary functions $\mathbf{b}_b^k$.

6.3.2 Basis Functions

In this chapter, we approximate the domain Ω^- as a partition of tetrahedra, with $h > 0$ the maximum edge length. Consequently, the boundary Γ_h is a triangulated surface. Moreover, we choose $\mathcal{V}^h$ as the space of lowest order Nédélec curl conforming elements [46], with basis functions $\mathbf{b}_i^n$ and $\mathbf{b}_b^n$ associated to the tangential electric field degrees of freedom on the internal and boundary

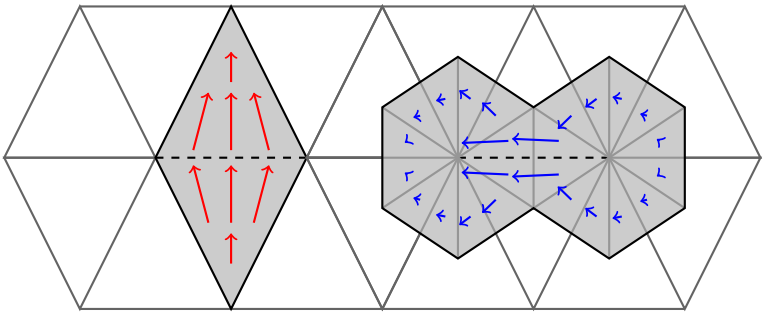

Figure 6.2: Divergence conforming Rao-Wilton-Glisson (left, $\hat{\mathbf{n}} \times \mathbf{b}_m^k$) and Buffa-Christiansen (right, $\mathbf{d}^n$) basis functions associated to the edges (in dotted line) of the triangulated surface mesh Γ_h.

edges, respectively. This implies in particular that the divergence conforming basis function $\hat{\mathbf{n}} \times \mathbf{b}_b^m$, i.e., the rotated trace of the Nédélec boundary edge element $\mathbf{b}_b^m$, corresponds to a lowest order Rao-Wilton-Glisson (RWG) function [23] (see Fig. 6.2). For the discretization of the boundary operators $\mathcal{T}_k$, which arises in the Calderón preconditioner, and $\mathcal{K}_k$, which arises in the hybrid formulation of section 6.4, we use the same triangular surface mesh Γ_h and define two types of basis functions on this mesh, associated with the edges (see Fig. 6.2). First, we use the RWG basis functions $\hat{\mathbf{n}} \times \mathbf{b}_b^k \in \mathbf{H}^{-\frac{1}{2}}(\mathsf{div}_\Gamma, \Gamma)$ for a Galerkin discretization of $\mathcal{T}_k$, denoted T.

$$(\mathsf{T})_{mn} = \int_\Gamma \mathbf{b}_b^m \cdot \mathcal{T}_k(\hat{\mathbf{n}} \times \mathbf{b}_b^n) \, \mathrm{d}S \tag{6.36}$$

The discretization of the left $\mathcal{T}_k$ operator in the well-conditioned operator products $\mathcal{T}_k\mathcal{T}_k$ and $\mathcal{T}_k\mathcal{P}$, which arise in the hybrid formulation of section 6.4, makes use of the basis of Buffa-Christiansen (BC) functions [22] $\mathbf{d}^n$, defined on the barycentrically refined mesh and *dual* to the RWG basis functions (Fig. 6.2). Denote the Galerkin discretization of $\mathcal{T}_k$ w.r.t. the BC basis $\mathbf{d}^n \in \mathbf{H}^{-\frac{1}{2}}(\mathsf{div}_\Gamma, \Gamma)$ as T_{bc}.

$$(\mathsf{T}_{\mathsf{bc}})_{mn} = \int_\Gamma (\hat{\mathbf{n}} \times \mathbf{d}^m) \cdot \mathcal{T}_k \mathbf{d}^n \, \mathrm{d}S \tag{6.37}$$

The mixed discretization of the operator $\mathcal{K}_k$, with RWG basis functions and $\hat{\mathbf{n}}\times$BC test functions, is denoted K.

$$(\mathsf{K})_{mn} = \int_\Gamma (\hat{\mathbf{n}} \times \mathbf{d}^m) \cdot \mathcal{K}_k(\hat{\mathbf{n}} \times \mathbf{b}_b^n) \, \mathrm{d}S \tag{6.38}$$

The mixed Gram matrix G links the RWG and BC bases.

$$(\mathsf{G})_{mn} = \int_\Gamma \mathbf{b}_b^m \cdot \mathbf{d}^n \, \mathrm{d}S \tag{6.39}$$

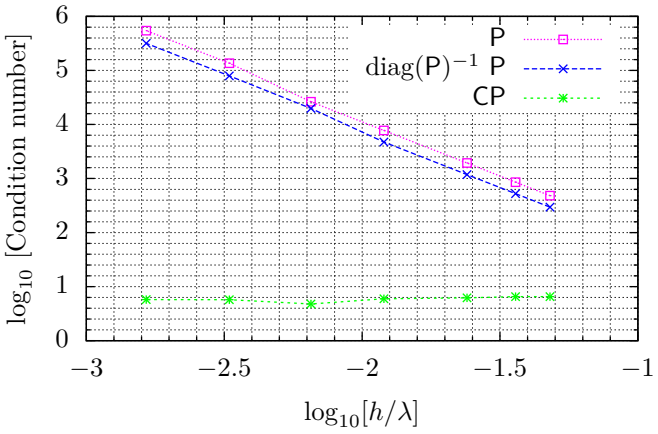

Figure 6.3: Condition number of P, with diagonal preconditioner $\mathrm{diag}(\mathsf{P})^{-1}$ and Calderón preconditioner C, versus the relative mesh element size h/λ for a Luneburg lens.

6.3.3 Dense Mesh Discretization Breakdown

Fig. 6.3 shows that the condition number of P (for the example of the Luneburg lens of §6.5.2) is already considerable for the moderate mesh size $h = 0.05\lambda$, and continues to grow monotonically if the mesh size decreases. This undesirable ill-conditioning, which is called dense mesh discretization breakdown, severely hampers both the accuracy (due to an increased sensitivity of the solution vector on the matrix and the right hand side accuracies) and convergence speed of iterative solvers [47]. The latter will be illustrated in the numerical examples of section 6.5.

The breakdown can be explained by the decomposition of $\mathcal{P}$ in Theorem 6.2.2. Note that $\mathcal{P}$ is proportional, up to a compact term (as $\mathcal{T}_k$ is bounded in $\mathbf{H}^{-\frac{1}{2}}(\mathsf{div}_\Gamma, \Gamma)$), to the Electric Field Integral Operator (EFIO) $\mathcal{T}_k$, whose Galerkin discretization is known to suffer from dense mesh discretization breakdown [15]. The compact term does not influence the singular value distribution of $\mathcal{P}$ significantly, as its singular values accumulate at 0. Indeed, the singular value distributions of T and P for a dense mesh ($h/\lambda = 1.7 \cdot 10^{-3}$, $N_b = 4521$ unknowns) are very similar (Fig. 6.4), with the well-known two branches of singular values accumulating at 0 and ∞ (for $N_b \to \infty$) clearly visible [15]. As a consequence, the h^{-2} behavior of the condition number of T [48] is also encountered in the discretization P (see Fig. 6.3).

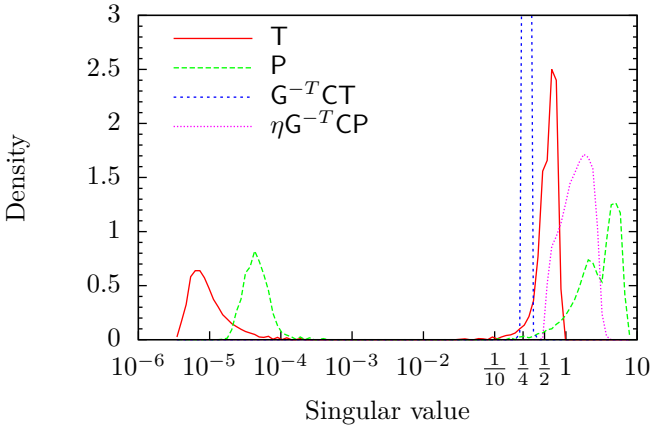

Figure 6.4: Singular value distribution of T and P, with and without Calderón preconditioner, for the Luneburg lens with $h/\lambda = 1.7 \cdot 10^{-3}$ and $N_b = 4521$ unknowns.

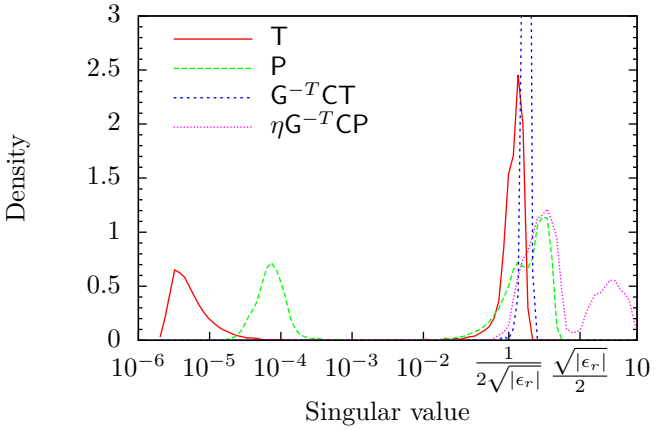

Figure 6.5: Singular value distribution of T and P, with and without Calderón preconditioner, for the homogeneous dielectric cube with $\epsilon_r = 10 - 0.1j$, $h/\lambda = 2.3 \cdot 10^{-3}$ and $N_b = 4962$ unknowns.

6.3.4 Calderón Multiplicative Preconditioner

Our goal is to propose a multiplicative preconditioner $\mathsf{C} \in \mathbb{C}^{N_b \times N_b}$ such that the condition number of CP is uniformly bounded as a function of N_b, i.e., such that C cures P of dense mesh discretization breakdown. Corollary 6.2.3 states that the operator product $2\eta\mathcal{T}_k\mathcal{P}$ is the sum of a compact operator (whose singular values accumulate at zero) and the identity operator, implying that $\mathcal{T}_k\mathcal{P}$ is well-conditioned in $\mathbf{H}^{-\frac{1}{2}}(\mathsf{div}_\Gamma, \Gamma)$ (its singular values accumulate at $\frac{1}{2\eta}$).

Inspired by these observations, we are looking for C such that CP is a discretization of the continuous operator $\mathcal{T}_k\mathcal{P}$. The specific expression for C described hereafter corresponds to the multiplicative preconditioner of the EFIO $\mathcal{T}_k$ based on RWG and BC basis functions for the discretization of the two operators in the product $\mathcal{T}_k\mathcal{T}_k$ [15], [22]. This has the additional advantage that C is also a preconditioner for T, which will be exploited in the construction of an efficient preconditioner for the proposed hybrid formulation in section 6.4. In line with [15] and with contributions on similar preconditioning strategies for other operators [16], [18]–[21], [49], [50], we call C a *Calderón* multiplicative preconditioner. Similar to [15], we choose

$$\mathsf{C} = \mathsf{T}_{\mathsf{bc}}\mathsf{G}^{-1}. \tag{6.40}$$

By (6.35), P is (an approximation of) a Galerkin discretization of $\mathcal{P}$ with RWG basis functions $\hat{\mathbf{n}} \times \mathbf{b}_b^m$. By (6.36), T_{bc} is a Galerkin discretization of $\mathcal{T}_k$ with BC basis functions $\mathbf{d}^m$. It has been proven that the condition number of the sparse mixed Gram G, linking RWG and BC functions, is uniformly bounded as a function of N_b (for regular meshes) [22], and is small in practice [15], which ensures a fast iterative solution of its inverse. The choice of BC functions for the discretization of $\mathcal{T}_k$, which leads to a well-conditioned mixed Gram matrix G, ensures that the beneficial spectral properties of $\mathcal{T}_k\mathcal{P}$ are inherited by the discretization CP.

Observe in Fig. 6.3 that the condition number of CP is relatively small and stays constant as a function of the relative mesh size h/λ. Unlike the diagonal preconditioner, the Calderón multiplicative preconditioner removes the dense mesh discretization breakdown of P. This is also reflected by the singular value distributions of the Calderón preconditioned operators $\eta\mathsf{G}^{-T}\mathsf{CP}$ and $\mathsf{G}^{-T}\mathsf{CT}$ for the Luneburg lens, shown in Fig. 6.4, which manifest one cluster of singular values (instead of the two separated branches of T and P) around $\frac{1}{2}$ and $\frac{1}{4}$, respectively, as expected from Corollary 6.2.3 and Calderón identity (6.14). Note that the transposed inverse (well-conditioned) Gram matrix G^{-T} does not significantly influence the condition number of CT and CP or the behavior of their singular value distribution, but is merely added such that the accumulation points $\frac{1}{2}$ and $\frac{1}{4}$ correspond to those of the continuous operators $\eta\mathcal{T}_k\mathcal{P}$ and $\mathcal{T}_k^2$, respectively.

Fig. 6.5 illustrates the effect of a discontinuity in the permittivity at the boundary Γ on the singular value distribution of the discretized operators,

for the example of the homogeneous dielectric cube of §6.5.3 with relative permittivity $\epsilon_r = 10 - 0.1j$. We observe two clusters of singular values of the Calderón preconditioned operator $\eta \mathsf{G}^{-T}\mathsf{CP}$ around $\left|\frac{k'}{2k}\right| = \frac{1}{2}|\epsilon_r|^{-1/2}$ and $\left|\frac{k}{2k'}\right| = \frac{1}{2}|\epsilon_r|^{1/2}$, in line with Corollary 6.2.4 (although Γ is strictly speaking not smooth), with k' the wavenumber of the homogeneous exterior domain in this case, and $k = \sqrt{\epsilon_r}k'$ and η the wavenumber and characteristic impedance of the homogeneous cube, respectively. Therefore, the preconditioner C (with wavenumber k' in the discretization T_{bc}) cures P (with wavenumber k at the boundary) from dense discretization breakdown, even if $k \neq k'$. However, the appearance of two clusters of singular values leads, in general, to a higher condition number of $\eta \mathsf{G}^{-T}\mathsf{CP}$ (whose logarithm is equal to the length of the smallest interval that contains the support of the curves in Figs. 6.4 and 6.5), in comparison with the case $k = k'$.

6.4 Preconditioned Reduced Hybrid FEM-BEM Formulation

The numerical simulation of the scattering problem (6.1)–(6.4) at a heterogeneous domain typically combines a boundary element method (BEM) [38], [41], [51], with unknown current densities in a finite-dimensional subspace of $\mathbf{H}^{-\frac{1}{2}}(\mathsf{div}_\Gamma, \Gamma)$, with a finite element method [44], [45], with an unknown electric field in a finite-dimensional subspace of $\mathbf{H}(\mathsf{curl}, \Omega^-)$, resulting in a hybrid FEM-BEM method, sometimes called FE-BI (finite element, boundary integral) method [39], [52]. In this way, the advantages of both methods, i.e., the natural incorporation of heterogeneous material parameters in FEM and the inherent validity of the radiation condition of the scattered fields in BEM, are combined.

In this section, we propose a hybrid FEM-BEM formulation whose reduced form (after elimination of the interior FEM degrees of freedom) is suitable for Calderón preconditioning. The proposed Calderón multiplicative preconditioner for the reduced FEM-BEM system relies on the fact that C (as introduced in §6.3.4) is a preconditioner for both T and P.

6.4.1 Formulation

Consider a tangential magnetic current density $\mathbf{m}_0 \in \mathbf{H}^{-\frac{1}{2}}(\mathsf{div}_\Gamma, \Gamma)$ flowing on Γ and generating scattered fields in the exterior domain Ω^+ (Fig. 6.1). In order to make the formulation amenable to multiplicative Calderón preconditioning, as explained in the next section, $\mathbf{m}_0$ is the only source for the scattered fields in Ω^+ (no electric current density is assumed). This implies that, in general, $\mathbf{m}_0$ is different from the trace of the total tangential electric field, similar to the magnetic current formulation of [53]. Along with the unknown current density $\mathbf{m}_0$, we consider this *total* tangential electric field at the boundary, i.e., the interior limit of $\hat{\mathbf{n}} \times \mathbf{e}$ to the boundary, as another independent unknown of the

formulation. The exterior traces of the total tangential electric and magnetic fields follow immediately from (6.12) and are given by $\hat{\mathbf{n}} \times \mathbf{e}^{(i)} + (\mathcal{K}_k + \frac{1}{2})\mathbf{m}_0$ and $\hat{\mathbf{n}} \times \mathbf{h}^{(i)} + \frac{1}{\eta}\mathcal{T}_k \mathbf{m}_0$, respectively. The interior traces of the total tangential electric and magnetic fields are given by $\hat{\mathbf{n}} \times \mathbf{e}$ and $\mathcal{P}(\hat{\mathbf{n}} \times \mathbf{e})$, respectively. Expressing the the tangential continuity of the electric and magnetic fields at the boundary leads to the following system (6.41).

$$\begin{cases} (\mathcal{K}_k + \frac{1}{2})\mathbf{m}_0 - \hat{\mathbf{n}} \times \mathbf{e} & = -\hat{\mathbf{n}} \times \mathbf{e}^{(i)} \\ \frac{1}{\eta}\mathcal{T}_k \mathbf{m}_0 - \mathcal{P}(\hat{\mathbf{n}} \times \mathbf{e}) & = -\hat{\mathbf{n}} \times \mathbf{h}^{(i)} \end{cases} \tag{6.41}$$

After expanding the unknowns $\mathbf{m}_0$ and $\hat{\mathbf{n}} \times \mathbf{e}$ into RWG functions $\hat{\mathbf{n}} \times \mathbf{b}_b^m$, testing the first equation of (6.41) with $\hat{\mathbf{n}}\times$ BC functions $\hat{\mathbf{n}} \times \mathbf{d}^m$ and the second equation with $\hat{\mathbf{n}}\times$RWG functions $\mathbf{b}_b^m$, and using equations (6.35)–(6.38), we obtain the discretized system

$$\begin{pmatrix} \mathsf{K} - \frac{1}{2}\mathsf{G}^T & -\mathsf{G}^T \\ \mathsf{T}/\eta & -\mathsf{P} \end{pmatrix} \begin{pmatrix} \bar{\alpha} \\ \bar{\beta} \end{pmatrix} = \begin{pmatrix} \bar{a} \\ \bar{b} \end{pmatrix}, \tag{6.42}$$

with $\bar{\alpha}$ and $\bar{\beta}$ the expansion coefficients of $\mathbf{m}_0$ and $\hat{\mathbf{n}} \times \mathbf{e}$, respectively, $(\bar{a})_m = -\int_\Gamma \mathbf{d}^m \cdot \mathbf{e}^{(i)} \mathrm{d}S$ and $(\bar{b})_m = \int_\Gamma (\hat{\mathbf{n}} \times \mathbf{b}_b^m) \cdot \mathbf{h}^{(i)} \mathrm{d}S$. The presence of the ill-conditioned submatrices T/η and P, which suffer from dense mesh discretization breakdown as explained in section 6.3.3, causes an ill-conditioned system matrix, which negatively affects the convergence speed of an iterative solution algorithm of system (6.42) (see section 6.5).

6.4.2 Calderón Multiplicative Preconditioner

It is well-known that the mixed Gram matrix does not suffer from dense mesh discretization breakdown and is well-conditioned [15], [22]. Moreover, the submatrix $\mathsf{K} - \frac{1}{2}\mathsf{G}^T$ in (6.42) is the so-called mixed discretization of the MFIE (magnetic field integral equation) operator $\mathcal{K}_k - \frac{1}{2}$, and is known to be well-conditioned [54]. Taking these observations into account and the fact that C is a preconditioner for both T and P, we propose the following Calderón multiplicative preconditioner for hybrid system (6.42), with I the identity matrix:

$$\mathsf{C}_s = \begin{pmatrix} \mathsf{I} & 0 \\ 0 & \mathsf{C} \end{pmatrix}. \tag{6.43}$$

This leads to the preconditioned reduced hybrid FEM-BEM system

$$\begin{pmatrix} \mathsf{K} - \frac{1}{2}\mathsf{G}^T & -\mathsf{G}^T \\ \mathsf{T}_{\mathsf{bc}}\mathsf{G}^{-1}\mathsf{T}/\eta & -\mathsf{T}_{\mathsf{bc}}\mathsf{G}^{-1}\mathsf{P} \end{pmatrix} \begin{pmatrix} \bar{\alpha} \\ \bar{\beta} \end{pmatrix} = \begin{pmatrix} \bar{a} \\ \mathsf{T}_{\mathsf{bc}}\mathsf{G}^{-1}\bar{b} \end{pmatrix}, \tag{6.44}$$

Note that the desired property that the preconditioned hybrid system matrix in (6.44) is well-conditioned does not necessarily follow from the fact that its submatrices are well-conditioned (an illustrative counterexample is a block matrix

filled with identity submatrices), but will be shown to hold for representative numerical examples in Section 6.5. The preconditioner C_s is fully compatible with existing matrix vector product acceleration schemes, such as the multilevel fast multipole algorithm (MLFMA) [31]–[34].

6.4.3 Low-frequency behavior

Suppose Ω^- is simply connected. Then it is well known that the mixed discretization $\mathsf{K} - \frac{1}{2}\mathsf{G}^T$ is an accurate and well-conditioned discretization of the MFIE operator $\mathcal{K}_k - \frac{1}{2}$ at arbitrarily low frequencies, without the explicit need to refine the mesh [55]. Moreover, in absence of numerical cancellation errors in the calculation of T, T_{bc} and the matrix products (which can be circumvented by using a loop-star decomposition), $\mathsf{T}_{\mathsf{bc}}\mathsf{G}^{-1}\mathsf{T}$ is an accurate and well-conditioned discretization of the Calderón preconditioned EFIE operator $\mathcal{T}_k^2$ for arbitrarily low frequencies [56]. Considering the similarities between the Calderón preconditioned EFIE and PS operators (cf. Corollary 6.2.3 and Section 6.3.4), it is expected that $\mathsf{T}_{\mathsf{bc}}\mathsf{G}^{-1}\mathsf{P}$ is an accurate and well-conditioned discretization of the Calderón preconditioned PS operator $\mathcal{T}_k\mathcal{P}$ for arbitrarily low frequencies, in which case the preconditioned reduced hybrid FEM-BEM system (6.44) is expected to be accurate and well-conditioned at arbitrarily low frequencies. However, these statements, along with a loop-star decomposition for $\mathsf{T}_{\mathsf{bc}}\mathsf{G}^{-1}\mathsf{P}$, require further investigation and are beyond the scope of this chapter.

For multiply connected Ω^-, nontrivial nullspaces of the static limits of the operators $\mathcal{K}_k - \frac{1}{2}$ and $\mathcal{T}_k^2$ lead to ill-conditioning of their respective discretizations $\mathsf{K} - \frac{1}{2}\mathsf{G}^T$ and $\mathsf{T}_{\mathsf{bc}}\mathsf{G}^{-1}\mathsf{T}$ at low frequencies [57]. By Theorem 6.2.2, the same phenomenon pertains to $\mathcal{T}_k\mathcal{P}$, although further investigation is required to solve the resulting ill-conditioning of $\mathsf{T}_{\mathsf{bc}}\mathsf{G}^{-1}\mathsf{P}$ at low frequencies for those multiply connected domains.

6.5 Numerical Examples

6.5.1 Scattering at a Homogeneous Dielectric Ball

This example investigates the accuracy of the proposed hybrid formulation (6.42), for the case of linearly polarized plane wave scattering at a dielectric ball with constant relative permittivity $\epsilon_r = \epsilon_1/\epsilon_0 = 2$ and diameter d. Fig. 6.7 shows excellent agreement between the scattered electric far field $\lambda^2 R|\mathbf{e}|$ (scaled with the distance R), obtained with the hybrid formulation for the mesh of Fig. 6.6, and the analytical Mie solution [58], [59], for low ($\lambda = 10d$, Rayleigh scattering regime) and high ($\lambda = d$) frequencies.

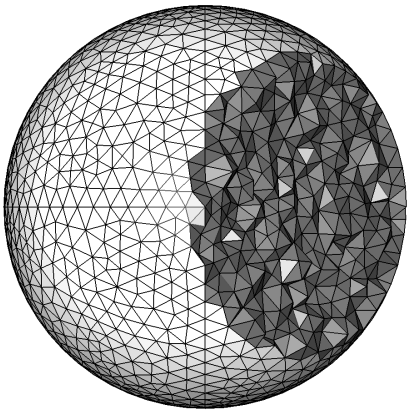

Figure 6.6: Truncated mesh of a spherical ball with diameter d, maximum edge length $h = 0.05d$, $N_b = 4491$ boundary edges and $N_i = 40393$ interior edges.

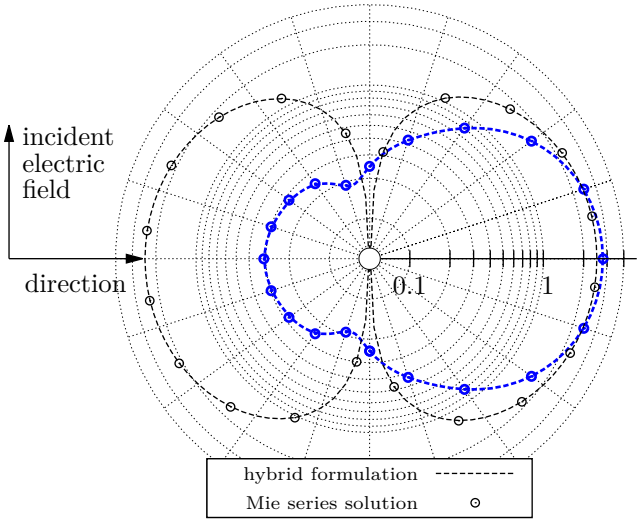

Figure 6.7: Scattered electric far field for the dielectric ball of Fig. 6.6 ($\epsilon_r = 2$) at low ($\lambda = 10d$) and high ($\lambda = d$, in bold lines and symbols) frequencies.

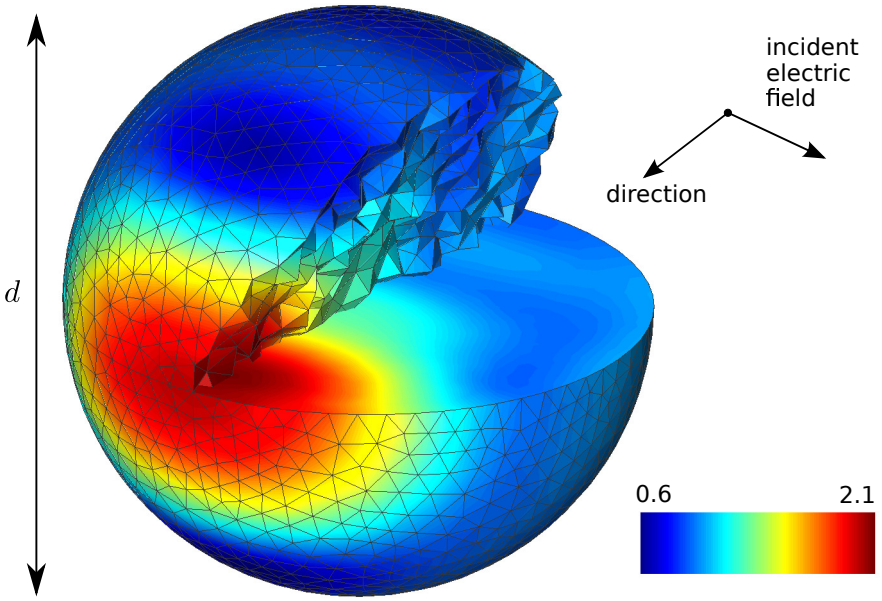

Figure 6.8: Relative electric field magnitude in a Luneburg lens with diameter d (cut to visualize the interior field) for linearly polarized plane wave scattering with wavelength $\lambda = 0.8d$ and unit electric field magnitude.

6.5.2 Scattering at a Luneburg Lens

In this example the effectiveness of the Calderón multiplicative preconditioner for the hybrid formulation (6.42) will be investigated. Consider scattering at a classical Luneburg lens, which is a spherical lens with diameter d with spherically symmetric relative permittivity $\epsilon_r = \epsilon_1/\epsilon_0 = 2 - r^2/(d/2)^2$ depending on the distance r to its center. In the high frequency limit, i.e. in the ray optics regime (valid for wavelengths $\lambda \ll d$), it has been proven that a parallel bundle of rays impinging on the lens is focused in a point at the other side on the spherical surface [60]. Fig. 6.8, which results from the solution of the preconditioned hybrid system with the mesh of Fig. 6.6, shows that this property is still approximately valid for plane wave incidence at $\lambda = 0.8d$.

Figs. 6.9 and 6.10 illustrate the effect of dense mesh discretization breakdown of the discretized Poincaré-Steklov operator P (as shown in Fig. 6.3) on the number of iterations and the convergence of the reduced hybrid FEM-BEM system (6.42), even with diagonal preconditioner. As expected the Calderón multiplicative preconditioner (6.43), which cures the system from the breakdown, leads to a nearly constant number of iterations for different mesh sizes h/λ, for fixed wavelength λ and precision of the iterative solution algorithm (TFQMR [61] is used in all examples).

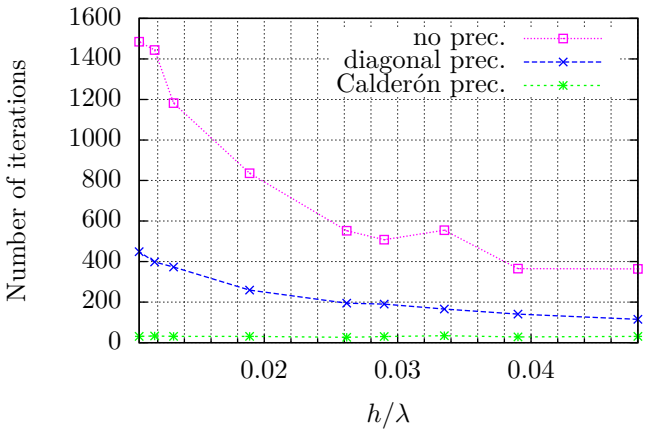

Figure 6.9: Number of iterations for the solution of (6.42) (TFQMR, 10^{-9} precision) for scattering at the Luneburg lens of Fig. 6.8, for different preconditioners, as a function of the relative mesh size h/λ (with $\lambda = 4d$).

The increase in number of iterations is reflected by the execution times in Fig. 6.11, where it should be noted that the execution time of the TFQMR algorithm with Calderón preconditioner increases for lower h/λ because of the increasing dimensionality of the system, but the number of iterations stays constant (see Fig. 6.9). The calculation of P, present in formulation (6.42), involves the calculation of a Schur complement of the sparse FEM system matrix, as shown in (6.32). This step is accomplished by the parallel sparse direct multifrontal solver MUMPS [62], and one observes in Fig. 6.11 that it executes faster than the iterative solution for the considered mesh sizes.

6.5.3 Scattering at a Lossy Homogeneous Dielectric Cube

In the previous example, the boundary Γ is smooth, allowing the direct application of Theorem 6.2.2 and Corollary 6.2.3 to explain the observed lack of dense mesh discretization breakdown of the preconditioned system (6.44). In order to investigate the effects of a non-smooth (but Lipschitzian) boundary and a discontinuity of the permittivity at Γ (i.e., a configuration where $\lim_{\Omega^- \ni \boldsymbol{\rho} \to \Gamma} \epsilon_1(\boldsymbol{\rho})$ is constant but different from the permittivity ϵ_0 of the exterior homogeneous domain Ω^+), we consider scattering at the lossy homogeneous dielectric cube of Fig. 6.12 with relative (with respect to ϵ_0) permittivity $\epsilon_r = 10 - 0.1j$.

In line with the results of scattering at the Luneburg lens, we observe in Fig. 6.13 that the Calderón preconditioned system (6.44) again outperforms the original system (6.42), with or without diagonal preconditioner, in terms of

	$\mathcal{E}$	h/λ	number of iterations		
			no prec.	diag. prec.	Cald. prec.
Luneburg lens	10^{-9}	$4.8 \cdot 10^{-2}$	364	115	31
	10^{-9}	$2.6 \cdot 10^{-2}$	552	195	26
	10^{-9}	$1.1 \cdot 10^{-2}$	1485	449	31
	10^{-6}	$1.1 \cdot 10^{-2}$	1019	224	22
	10^{-3}	$1.1 \cdot 10^{-2}$	406	145	10
Cube	10^{-6}	$4.2 \cdot 10^{-2}$	148	66	40
	10^{-6}	$1.0 \cdot 10^{-2}$	691	215	57
	10^{-6}	$4.9 \cdot 10^{-3}$	1421	395	79
Graded-index fiber	10^{-6}	$5.3 \cdot 10^{-3}$	566	171	29
	10^{-6}	$3.8 \cdot 10^{-3}$	950	225	34
	10^{-6}	$2.0 \cdot 10^{-3}$	2223	408	46

Table 6.1: Number of iterations for the solution of (6.42) for scattering at the Luneburg lens (cf. Figs. 6.9 and 6.10), the lossy dielectric cube (cf. Fig. 6.13) and the bent graded-index fiber (cf. Fig. 6.15), for different preconditioners, as a function of the relative residual error $\mathcal{E}$ of the iterative solver (TFQMR) and the relative mesh size h/λ (with $\lambda = 4d$, $10d$ and $9l$, respectively).

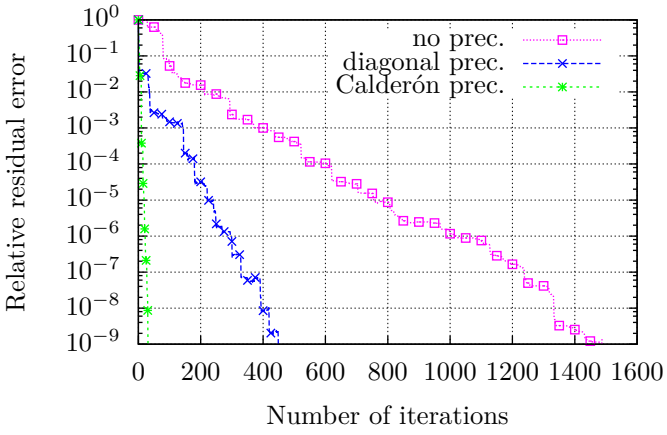

Figure 6.10: Relative residual error of the iterative solution algorithm (TFQMR) as a function of the number of iterations for the Luneburg lens with $h/\lambda = 0.01$ and $2N_b = 14016$ total unknowns.

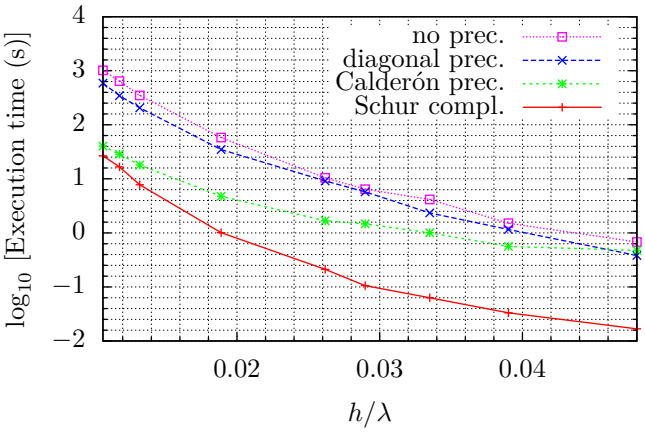

Figure 6.11: Execution times of the iterative solution for different preconditioners (for the same parameters of Fig. 6.9) and the Schur complement calculation using MUMPS.

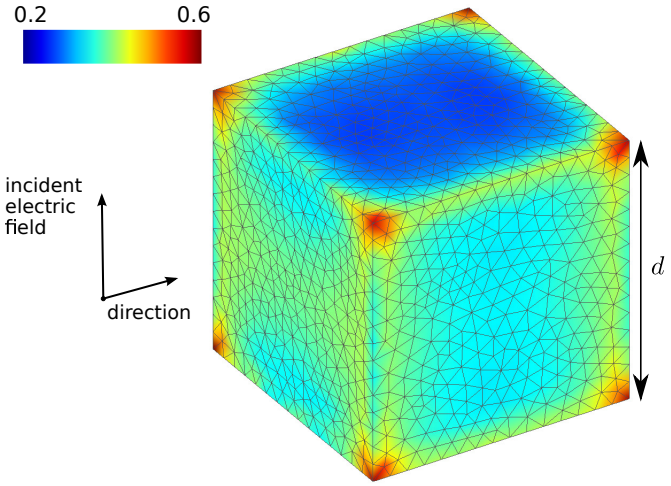

Figure 6.12: Relative electric field magnitude on the boundary (interior limit) of a lossy dielectric cube with relative permittivity $\epsilon_r = 10 - 0.1j$ and edge length d for linearly polarized plane wave scattering with wavelength $\lambda = 10d$ and unit electric field magnitude.

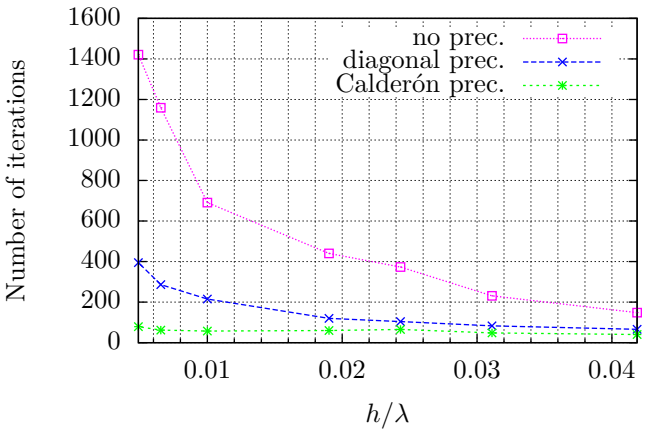

Figure 6.13: Number of iterations for the solution of (6.42) (TFQMR, 10^{-6} precision) for scattering at the homogeneous dielectric cube of Fig. 6.12, for different preconditioners, as a function of the relative mesh size h/λ (with $\lambda = 10d$).

number of iterations of the iterative solution. However, Table 6.1 reveals that the number of iterations, for a fixed precision $\mathcal{E}$, still increases slowly for a decreasing relative mesh size h/λ, which is not the case for the Luneburg lens. Therefore, the slow increase increase in number of iterations can be attributed to the non-smooth boundary, which causes singular tangential electric field components (of the exact solution) around the sharp corners (as can be observed in Fig. 6.12).

For the same precision $\mathcal{E} = 10^{-6}$ and comparable relative mesh sizes $h/\lambda = 1.0 \cdot 10^{-2}$ and $h/\lambda = 1.1 \cdot 10^{-2}$, we observe in Table 6.1 that the number of iterations for the cube is significantly higher than for the Luneburg lens (57 versus 22, respectively). This is due the higher condition number of the discrete preconditioned PS operator $\mathsf{T}_{\mathsf{bc}}\mathsf{G}^{-1}\mathsf{P}$ for the cube, which is caused by the jump in permittivity at the boundary, as explained in Section 6.3.4 and shown in Figs. 6.4 and 6.5 (where the logarithm of the condition number is equal to the length of the smallest interval that contains the support of the functions).

6.5.4 Scattering at a Bent Graded-index Fiber

Consider plane wave scattering at a bent graded-index fiber, with parabolically varying permittivity ϵ_1 ranging from $4\epsilon_0$ (at the center of the fiber) to $2\epsilon_0$ (on the boundary), as shown in Fig. 6.14. In addition to its practical relevance, this example is interesting because its permittivity, although in $C^1(\Omega^-)$, is not

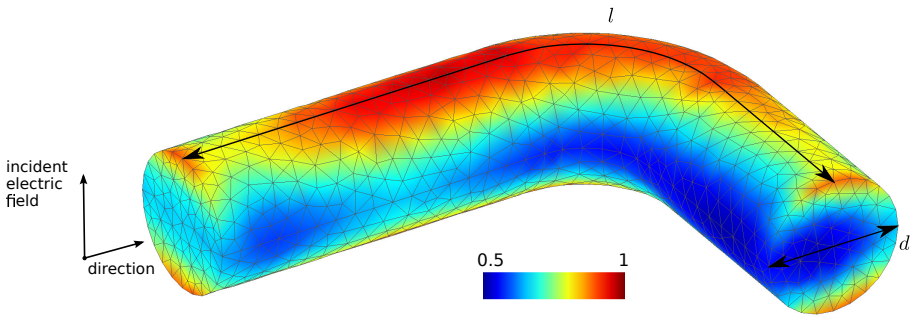

Figure 6.14: Relative electric field magnitude on the boundary (interior limit) of a bent graded-index fiber (with permittivity varying parabolically from $4\epsilon_0$ at the center to $2\epsilon_0$ on the boundary) with length l and diameter d for linearly polarized plane wave scattering with wavelength $\lambda = 5d = 0.9l$ and unit electric field magnitude.

constant on the boundary (it varies parabolically on the two cross sections).

Nevertheless, we observe in Fig. 6.15 and Table 6.1 that the Calderón preconditioner (6.43) cures the system (6.42) from dense mesh discretization breakdown, as indicated by the nearly constant number of iterations, whereas the number of iterations with diagonal preconditioner increases with decreasing mesh size. This is reflected by the execution times in Fig. 6.16, where we observe that the relative gain of the Calderón preconditioner w.r.t. the diagonal preconditioner increases for finer meshes, due to the earlier mentioned breakdown occurring with the latter preconditioner. Similar to the results in Fig. 6.11, the execution time of the iterative solution of the dense reduced hybrid system (6.42) dominates the calculation of the Schur complement (6.32) using the direct sparse solver MUMPS, as shown in Fig. 6.16, for all considered mesh sizes.

6.6 Conclusions

We prove that the electric field boundary integral operator can be used to regularize the continuous time-harmonic electromagnetic Poincaré-Steklov operator of a heterogeneous domain. The beneficial implications of a discrete Calderón multiplicative preconditioner (CMP) on the condition number of its finite element discretization are numerically investigated. This paves the way for an efficient iterative solution of reduced hybrid FEM-BEM problems. We demonstrate the accuracy of a formulation that is amenable to the CMP on a canonical problem and the effectiveness of the preconditioner in practically relevant scattering problems.

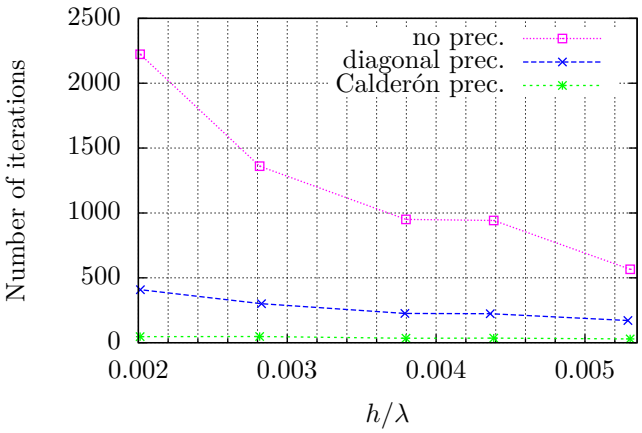

Figure 6.15: Number of iterations for the solution of (6.42) (TFQMR, 10^{-6} precision) for scattering at the bent graded-index fiber of Fig. 6.14, for different preconditioners, as a function of the relative mesh size h/λ (with $\lambda = 9l$).

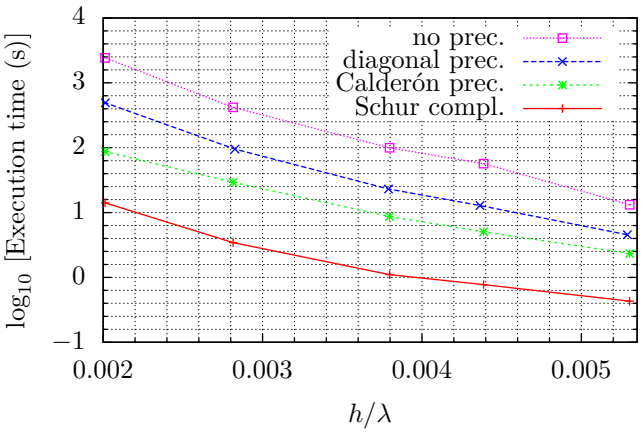

Figure 6.16: Execution times of the iterative solution for different preconditioners (for the same parameters of Fig. 6.15) and the Schur complement calculation using MUMPS.

References

[1] D. Dobbelaere, D. D. Zutter, J. V. Hese, J. Sercu, T. Boonen, and H. Rogier, "A Calderón multiplicative preconditioner for the electromagnetic Poincaré-Steklov operator of a heterogeneous domain with scattering applications", *Journal of Computational Physics*, `http://dx.doi.org/10.1016/j.jcp.2015.09.052`, 2015.

[2] R. R. Paz, N. M. Nigro, and M. A. Storti, "On the efficiency and quality of numerical solutions in CFD problems using the interface strip preconditioner for domain decomposition methods", *International journal for numerical methods in fluids*, vol. 52, no. 1, pp. 89–118, 2006.

[3] P. Demarcke and H. Rogier, "The Poincaré-Steklov operator in hybrid finite element-boundary integral equation formulations", *IEEE Antennas and Wireless Propagation Letters*, vol. 10, pp. 503–506, 2011.

[4] F. Boeykens, H. Rogier, J. Van Hese, J. Sercu, and T. Boonen, "Rigorous analysis of internal resonances in 3-D hybrid FE-BIE formulations by means of the Poincaré-Steklov operator", *Microwave Theory and Techniques, IEEE Transactions on*, vol. 61, no. 10, pp. 3503–3513, 2013.

[5] L. F. Knockaert and D. D. Zutter, "On the complex symmetry of the Poincaré-Steklov operator", *Progress In Electromagnetics Research B*, vol. 7, pp. 145–157, 2008.

[6] A. Quarteroni and A. Valli, "Theory and application of Steklov-Poincaré operators for boundary-value problems", in *Applied and Industrial Mathematics*, R. Spigler, Ed., vol. 56, Mathematics and Its Applications, Springer Netherlands, 1991, pp. 179–203.

[7] V. I Agoshkov, "Poincaré-Steklov operators and domain decomposition methods in finite dimensional spaces", in *First international symposium on domain decomposition methods for partial differential equations*, R. Glowinski, G. Golub, G. Meurant, and J. Périaux, Eds., SIAM, 1988, 73–112.

[8] A. Toselli and O. Widlund, *Domain Decomposition Methods - Algorithms and Theory*. Springer, 2005, Springer Series in Computational Mathematics.

[9] A. Krebs, M. Maischak, and E. P. Stephan, "Adaptive FEM-BEM coupling with a Schur complement error indicator.", *Appl. Numer. Math.*, vol. 60, no. 8, pp. 798–808, 2010.

[10] G. C. Hsiao and W. L. Wendland, *Boundary integral equations*. Berlin, Heidelberg: Springer, 2008, Applied Mathematical Sciences.

[11] F. Alouges, S. Borel, and D. Levadoux, "A stable well-conditioned integral equation for electromagnetism scattering", *Journal of Computational and Applied Mathematics*, vol. 204, no. 2, pp. 440 –451, 2007, Special Issue: The Seventh International Conference on Mathematical and Numerical Aspects of Waves (WAVES'05).

[12] M. A. Storti, L. Dalcín, R. Paz, A. Yommi, V. Sonzogni, and N. Nigro, "A preconditioner for the Schur complement matrix.", *Advances in Engineering Software*, vol. 37, no. 11, pp. 754–762, Jan. 13, 2009.

[13] A. Gillman, A. Barnett, and P.-G. Martinsson, "A spectrally accurate direct solution technique for frequency-domain scattering problems with variable media", *BIT Numerical Mathematics*, vol. 55, no. 1, pp. 141–170, 2015.

[14] R. Adams, "Physical and analytical properties of a stabilized electric field integral equation", *Antennas and Propagation, IEEE Transactions on*, vol. 52, no. 2, pp. 362–372, 2004.

[15] F. Andriulli, K. Cools, H. Bagci, F. Olyslager, A. Buffa, S. Christiansen, and E. Michielssen, "A multiplicative Calderon preconditioner for the electric field integral equation", *Antennas and Propagation, IEEE Transactions on*, vol. 56, no. 8, pp. 2398–2412, 2008.

[16] H. Bagci, F. P. Andriulli, K. Cools, F. Olyslager, and E. Michielssen, "A Calderón multiplicative preconditioner for the combined field integral equation", *Antennas and Propagation, IEEE Transactions on*, vol. 57, no. 10, pp. 3387–3392, 2009.

[17] Y. Boubendir and C. Turc, "Well-conditioned boundary integral equation formulations for the solution of high-frequency electromagnetic scattering problems", *Computers and Mathematics with Applications*, vol. 67, no. 10, pp. 1772 –1805, 2014.

[18] F. Valdes, F. Andriulli, H. Bagci, and E. Michielssen, "A Calderón-preconditioned single source combined field integral equation for analyzing scattering from homogeneous penetrable objects", *Antennas and Propagation, IEEE Transactions on*, vol. 59, no. 6, pp. 2315–2328, 2011.

[19] K. Cools, F. Andriulli, and E. Michielssen, "A Calderón multiplicative preconditioner for the PMCHWT integral equation", *Antennas and Propagation, IEEE Transactions on*, vol. 59, no. 12, pp. 4579–4587, 2011.

[20] P. Yla-Oijala, S. Kiminki, and S. Jarvenpaa, "Calderon preconditioned surface integral equations for composite objects with junctions", *Antennas and Propagation, IEEE Transactions on*, vol. 59, no. 2, pp. 546–554, 2011.

[21] Y. Chen, S. Sun, L. Jiang, and W. C. Chew, "A Calderón preconditioner for the electric field integral equation with layered medium Green's function", *Antennas and Propagation, IEEE Transactions on*, vol. 62, no. 4, pp. 2022–2030, 2014.

[22] A. Buffa and S. H. Christiansen, "A dual finite element complex on the barycentric refinement", *Comptes Rendus Mathematique*, vol. 340, no. 6, pp. 461–464, 2005.

[23] S. Rao, D. Wilton, and A. Glisson, "Electromagnetic scattering by surfaces of arbitrary shape", *Antennas and Propagation, IEEE Transactions on*, vol. 30, no. 3, pp. 409–418, 1982.

[24] J. Liu and J.-M. Jin, "A highly effective preconditioner for solving the finite element-boundary integral matrix equation of 3-D scattering", *Antennas and Propagation, IEEE Transactions on*, vol. 50, no. 9, pp. 1212–1221, 2002.

[25] J. Lee, C. Zhang, and C.-C. Lu, "Sparse inverse preconditioning of multilevel fast multipole algorithm for hybrid integral equations in electromagnetics", *Antennas and Propagation, IEEE Transactions on*, vol. 52, no. 9, pp. 2277–2287, 2004.

[26] M.-L. Yang and X.-Q. Sheng, "Hybrid h- and p-type multiplicative Schwarz (h-p-MUS) preconditioned algorithm of higher-order FE-BI-MLFMA for 3D scattering", *Magnetics, IEEE Transactions on*, vol. 48, no. 2, pp. 187–190, 2012.

[27] L. Li, T.-Z. Huang, G.-H. Cheng, Y.-F. Jing, Z.-G. Ren, and H.-B. Li, "Solution to 3-D electromagnetic problems discretized by a hybrid FEM/MOM method", *Computer Physics Communications*, vol. 184, no. 1, pp. 73 –78, 2013.

[28] O. Wiedenmann, L. Li, and T. Eibert, "A direct hierarchical multilevel preconditioner for the solution of finite element-boundary integral equations", in *Antennas and Propagation (EuCAP), 2014 8th European Conference on*, 2014, pp. 3412–3416.

[29] Y. Boubendir, A. Bendali, and M. B. Fares, "Coupling of a non-overlapping domain decomposition method for a nodal finite element method with a boundary element method", *International Journal for Numerical Methods in Engineering*, vol. 73, no. 11, pp. 1624–1650, 2008.

[30] M.-L. Yang, H.-W. Gao, W. Song, and X.-Q. Sheng, "An effective domain-decomposition-based preconditioner for the FE-BI-MLFMA method for 3D scattering problems", *Antennas and Propagation, IEEE Transactions on*, vol. 62, no. 4, pp. 2263–2268, 2014.

[31] L. Greengard and V. Rokhlin, "A fast algorithm for particle simulations", *J. Comput. Phys.*, vol. 73, no. 2, pp. 325–348, Dec. 1987.

[32] V. Rokhlin, "Rapid solution of integral equations of scattering theory in two dimensions", *J. Comput. Phys.*, vol. 86, no. 2, pp. 414–439, Feb. 1990.

[33] W. Chew, E. Michielssen, J. M. Song, and J. M. Jin, Eds., *Fast and Efficient Algorithms in Computational Electromagnetics*. Norwood, MA, USA: Artech House, Inc., 2001.

[34] H. Cheng, W. Y. Crutchfield, Z. Gimbutas, L. F. Greengard, J. F. Ethridge, J. Huang, V. Rokhlin, N. Yarvin, and J. Zhao, "A wideband fast multipole method for the helmholtz equation in three dimensions", *Journal of Computational Physics*, vol. 216, no. 1, pp. 300–325, 2006.

[35] F. Andriulli, K. Cools, I. Bogaert, and E. Michielssen, "On a Well-Conditioned Electric Field Integral Operator for Multiply Connected Geometries", *IEEE Transactions on Antennas and Propagation*, vol. 61, no. 4, pp. 2077–2087, 2013.

[36] J. Van Bladel, *Electromagnetic Fields*. John Wiley & Sons, 2007, IEEE Press Series on Electromagnetic Wave Theory.

[37] J. Nédélec, *Acoustic and Electromagnetic Equations: Integral Representations for Harmonic Problems*. Springer, 2001.

[38] S. Sauter and C. Schwab, *Boundary Element Methods*. Springer, 2010, Springer Series in Computational Mathematics.

[39] R. Hiptmair, "Coupling of finite elements and boundary elements in electromagnetic scattering", *SIAM Journal on Numerical Analysis*, vol. 41, no. 3, pp. 919–944, 2004.

[40] R. A. Adams and J. J. Fournier, *Sobolev Spaces*. Elsevier, 2003, Pure and Applied Mathematics.

[41] A. Buffa and R. Hiptmair, "Galerkin boundary element methods for electromagnetic scattering", in *Topics in Computational Wave Propagation*, M. Ainsworth, P. Davies, D. Duncan, B. Rynne, and P. Martin, Eds., vol. 31, Lecture Notes in Computational Science and Engineering, Springer Berlin Heidelberg, 2003, pp. 83–124.

[42] G. Hanson and A. Yakovlev, *Operator Theory for Electromagnetics: An Introduction*. Springer, 2002.

[43] D. Colton and R. Kress, *Inverse Acoustic and Electromagnetic Scattering Theory*. Springer, 1998, Applied Mathematical Sciences.

[44] P. Monk, *Finite Element Methods for Maxwell's Equations*. Clarendon Press, 2003, Numerical Mathematics and Scientific Computation.

[45] J. Jin, *The Finite Element Method in Electromagnetics*, 3rd. Wiley-IEEE Press, 2014.

[46] J. Nédélec, "Mixed finite elements in $\mathbb{R}_3$", *Numerische Mathematik*, vol. 35, no. 3, pp. 315–341, 1980.

[47] L. N. Trefethen and D. Bau, *Numerical Linear Algebra*. SIAM, 1997.

[48] F. Andriulli, A. Tabacco, and G. Vecchi, "Solving the EFIE at low-frequencies with a conditioning that grows only logarithmically with the number of unknowns", *IEEE Transactions on Antennas and Propagation*, vol. 58, no. 05, pp. 1614–1624, 2010.

[49] S. Yan, J.-M. Jin, and Z. Nie, "Calderón preconditioner: from EFIE and MFIE to N-Müller equations", *Antennas and Propagation, IEEE Transactions on*, vol. 58, no. 12, pp. 4105–4110, 2010.

[50] J. Zhu, Y. Hu, R. Chen, and H. Zhu, "Calderon multiplicative preconditioner based on curvilinear elements for fast analysis of electromagnetic scattering", *Microwaves, Antennas Propagation, IET*, vol. 5, no. 1, pp. 102–112, 2011.

[51] R. F. Harrington, *Field Computation by Moment Methods*. Wiley-IEEE Press, 1993.

[52] J. Volakis, K. Sertel, and B. Usner, *Frequency Domain Hybrid Finite Element Methods for Electromagnetics*. Morgan & Claypool Publishers, 2006, Synthesis Lectures on Computational Electromagnetics.

[53] R. F. Harrington, "Boundary integral formulations for homogeneous material bodies", *Journal of Electromagnetic Waves and Applications*, vol. 3, no. 1, pp. 1–15, 1989.

[54] K. Cools, F. Andriulli, D. De Zutter, and E. Michielssen, "Accurate and conforming mixed discretization of the MFIE ", *IEEE antennas and wireless propagation letters*, vol. 10, pp. 528 –531, 2011.

[55] I. Bogaert, K. Cools, F. Andriulli, and H. Bagci, "Low-frequency scaling of the standard and mixed magnetic field and Müller integral equations", *Antennas and Propagation, IEEE Transactions on*, vol. 62, no. 2, pp. 822–831, 2014.

[56] S. Yan, J.-M. Jin, and Z. Nie, "EFIE analysis of low-frequency problems with loop-star decomposition and Calderón multiplicative preconditioner", *Antennas and Propagation, IEEE Transactions on*, vol. 58, no. 3, pp. 857–867, 2010.

[57] K. Cools, F. Andriulli, F. Olyslager, and E. Michielssen, "Nullspaces of MFIE and Calderón preconditioned EFIE operators applied to toroidal surfaces", *Antennas and Propagation, IEEE Transactions on*, vol. 57, no. 10, pp. 3205–3215, 2009.

[58] G. Mie, "Beiträge zur Optik trüber Medien, speziell kolloidaler Metallösungen", *Annalen der Physik*, vol. 330, pp. 377–445, 1908.

[59] J. A. Stratton, *Electromagnetic Theory*, 1st ed. McGraw-Hill Companies (New York), 1941.

[60] R. K. Luneburg, *Mathematical Theory of Optics*. Brown U. Press, Providence, R.I., 1944, 189—213.

[61] R. W. Freund, "A transpose-free quasi-minimal residual algorithm for non-Hermitian linear systems", *SIAM J. Sci. Comput.*, vol. 14, no. 2, pp. 470–482, Mar. 1993.

[62] P. R. Amestoy, I. S. Duff, J.-Y. L'Excellent, and J. Koster, "A fully asynchronous multifrontal solver using distributed dynamic scheduling", *SIAM J. Matrix Anal. Appl.*, vol. 23, no. 1, pp. 15–41, 2001.

Conclusions and Future Research

Presented research

The first part presents a full-wave analysis technique for multiconductor waveguides with imperfect conductors, based on an efficient root-finding algorithm for the determinant of a MoM discretization of the 2.5-D PMCHWT integral equation, in the complex longitudinal wavenumber plane. Chapter 3 presents a novel technique to efficiently evaluate MoM interaction integrals in media with arbitrary conductivities, for a given precision, allowing an accurate prediction of all wave phenomena occurring inside conductors, including losses. In chapter 4, some analytic properties of the numerically obtained dispersion curves are derived, with the help of some known results of complex analysis in several variables. Some properties regarding the smoothness of dispersion curves, the possible intersections of dispersion curves, the multiplicity of the numerically found propagation constants and its relation to the nullity of the MoM matrix, are proven and incorporated into an efficient numerical framework that is capable of determining the propagation constants and eigenmode field distributions of a multiconductor waveguide as a function of frequency.

Part II presents a Calderón multiplicative preconditioner (CMP) for the Poincaré-Steklov (PS) operator of a heterogeneous domain, for the first time. In chapter 6, a specific decomposition of the PS operator is derived, under some regularity assumptions on the domain and permittivity, which implies that it is regularized by the electric field integral operator, i.e., that their product can be written as a compact perturbation of a well-conditioned operator, in the natural Sobolev space of tangential current densities. Moreover, a novel hybrid finite/boundary element method is presented whose reduced form is amenable to the proposed CMP. Numerical examples corroborate the correctness of the formulation, the effect of the CMP on the singular values of the discretized PS operator, and the effectiveness of the CMP for the reduction of the required number of iterations for the solution of the reduced hybrid formulation, in comparison with a diagonal preconditioner.

Future research

Unfortunately, some interesting questions and research topics that arose during the research or in retrospect have not been explored further, mainly due to lack of time. Nevertheless, it seems valuable to outline those research topics, not

only in view of potential future research, but also to better sketch the context of the presented research.

First, it seems interesting to compare the full-wave modal analysis to the quasi-T(E)M analysis of chapter 2, to investigate the validity range of the latter for different types of waveguides. Although the employed 2.5-D PMCHWT system has the advantages of a lack of resonances and a relatively high accuracy for the lowest-order basis functions, it remains susceptible to dense mesh discretization breakdown and low frequency breakdown. Possibly, both types of breakdown can be solved by a Calderón preconditioner, by analogy with the 3-D PMCHWT equation [1], although the presence of global loops might necessitate some extra projectors and scalings (cf. [2]). One might also resort to other integral equations, such as the Müller equation, for which it is easy to see that the properties derived in chapter 4 still hold.

Concerning the results in chapter 6, a lot of possible avenues for future research exist. It seems interesting to investigate the scalability and time complexity of the different steps of the Calderón preconditioned hybrid formulation, in view of the simulation of structures that are very large with respect to the wavelength. The numerical results of section 6.5 already indicate that the calculation of the Schur complement in the reduced formulation will be the predominant factor in the time complexity of the total solution. Instead of using a direct solver to eliminate the internal unknowns, a scalable (preconditioned) iterative solver, e.g. FETI-DP [3], might be used to lower the time complexity. Also, it is interesting to compare the performance of the proposed Calderón preconditioned hybrid formulation to other preconditioned hybrid formulations in literature, e.g. [4], [5]. Finally, several other properties of the proposed preconditioned PS operator and hybrid formulation, including low-frequency stability, might be investigated.

References

[1] K. Cools, F. Andriulli, and E. Michielssen, "A Calderón multiplicative preconditioner for the PMCHWT integral equation", *Antennas and Propagation, IEEE Transactions on*, vol. 59, no. 12, pp. 4579–4587, 2011.

[2] F. Andriulli, K. Cools, I. Bogaert, and E. Michielssen, "On a Well-Conditioned Electric Field Integral Operator for Multiply Connected Geometries", *IEEE Transactions on Antennas and Propagation*, vol. 61, no. 4, pp. 2077–2087, 2013.

[3] Y.-J. Li and J.-M. Jin, "A new dual-primal domain decomposition approach for finite element simulation of 3-D large-scale electromagnetic problems", *Antennas and Propagation, IEEE Transactions on*, vol. 55, no. 10, pp. 2803–2810, 2007.

[4] J. Liu and J.-M. Jin, "A highly effective preconditioner for solving the finite element-boundary integral matrix equation of 3-D scattering", *Antennas and Propagation, IEEE Transactions on*, vol. 50, no. 9, pp. 1212–1221, 2002.

[5] M.-L. Yang, H.-W. Gao, and X.-Q. Sheng, "Parallel domain-decomposition-based algorithm of hybrid FE-BI-MLFMA method for 3-D scattering by large inhomogeneous objects", *Antennas and Propagation, IEEE Transactions on*, vol. 61, no. 9, pp. 4675–4684, 2013.